

January 2010

# Development of Atomistic Potentials for Silicate Materials and Coarse-Grained Simulation of Self-Assembly at Surfaces

Brian Barnes

*Washington University in St. Louis*

Follow this and additional works at: <https://openscholarship.wustl.edu/etd>

---

## Recommended Citation

Barnes, Brian, "Development of Atomistic Potentials for Silicate Materials and Coarse-Grained Simulation of Self-Assembly at Surfaces" (2010). *All Theses and Dissertations (ETDs)*. 30.  
<https://openscholarship.wustl.edu/etd/30>

This Dissertation is brought to you for free and open access by Washington University Open Scholarship. It has been accepted for inclusion in All Theses and Dissertations (ETDs) by an authorized administrator of Washington University Open Scholarship. For more information, please contact [digital@wumail.wustl.edu](mailto:digital@wumail.wustl.edu).

WASHINGTON UNIVERSITY IN ST. LOUIS

Department of Chemistry

Dissertation Examination Committee:

Lev D. Gelb, Chair

William Buhro, Co-Chair

Ken Kelton

Zohar Nussinov

Jacob Schaefer

Lee Sobotka

DEVELOPMENT OF ATOMISTIC POTENTIALS FOR SILICATE MATERIALS AND  
COARSE-GRAINED SIMULATION OF SELF-ASSEMBLY AT SURFACES

by

Brian Christopher Barnes

A dissertation presented to the  
Graduate School of Arts and Sciences  
of Washington University in  
partial fulfillment of the  
requirements for the degree  
of Doctor of Philosophy

December 2010

Saint Louis, Missouri

# Acknowledgments

I have had the good fortune to interact with many exceptional people on a regular basis. First and foremost is my advisor Lev Gelb. Lev has always been fair and academically rigorous, whether praising a success or pointing out things needing improvement. Our group meetings, however small, always had interesting scientific discussion. His innate curiosity and occasional excitement about science (or computers!) set the tone for the group. He has been a mentor and a friend.

Within the group, Dr. Niny Rao answered my novice questions about programming and molecular dynamics. Dr. Rafael Salazar Tio was an energetic and insightful lab compatriot, especially in regard to Monte Carlo and global optimization techniques. Dr. Dan Siderius was an enthusiastic labmate and excellent collaborator. He contributed to the thermodynamic analysis and programs used for the polyominoes research in this work. I enjoyed many discussions, scientific and otherwise, with Dr. Somendra Nath Chakraborty.

I learned a great deal in courses taught by the chemistry faculty on my committee, Profs. Buhro, Schaefer, and Sobotka – and our out of class conversations were also valuable. I am glad to have talked science and published work with Prof. Tom Vaid. Prof. Amy Walker consistently offered assistance, insight, and encouragement. Dr. Ed Hiss handles whatever problems or questions graduate students throw at him, and cannot be thanked enough. Profs. John C. Gilbert and John F. Stanton, from my years at UT-Austin, provided personal inspiration and guidance which gave me the determination to earn a doctoral degree.

Curtis Carey recruited me to the department, and his camaraderie will never be forgotten. John Glennon was a good study partner and friend. Charles Constantine and Matt van Duzor are also invaluable friends, confidants, and peers.

My parents deserve special mention, and will receive it on the next page.

Finally, Kate has been unwavering in her support, patience, and tolerance for intermittent grumpiness. I'm happy she was there when I went to ask where the physical chemistry books were located.

Brian Christopher Barnes

*Washington University in Saint Louis*  
*December 2010*

Dedicated to my parents, Mary Lou and Harry N. Barnes.

Their encouragement and support allowed this goal to become a reality.

# Contents

<b>Acknowledgments</b>	<b>ii</b>
<b>List of Tables</b>	<b>vii</b>
<b>List of Figures</b>	<b>ix</b>
<b>Glossary</b>	<b>xiv</b>
<b>1 Overview</b>	<b>1</b>
1.1 Development and Application of Evolutionary Strategies for Potential Parametrization	1
1.2 Thermodynamics and Self-Assembly of Polyominoes	3
<b>2 Meta-Optimization of Evolutionary Strategies for Empirical Potential Development: Application to Aqueous Silicate Systems</b>	<b>5</b>
2.1 Introduction	5
2.2 Methodology	14
2.2.1 Evolutionary Strategy Optimizations	14
2.2.2 Fitness Function	17
2.2.3 Application	18
2.2.4 Training Sets	20
2.2.5 Implementation	22
2.3 Meta-optimization of evolutionary strategies	23
2.3.1 Preliminary studies	24
2.3.2 Population	29
2.3.3 Recombination	33
2.3.4 Mutation Size Control	36
2.3.5 Selection	41
2.3.6 Simulated Annealing	43
2.4 Parametrization against CPMD reference data	44
2.5 Discussion	49
<b>3 Towards an Improved Charge-Transfer Potential for Silica</b>	<b>56</b>
3.1 Introduction	56
3.2 Potential Development	59
3.2.1 Functional Form	61

3.2.2	Training Sets and Parametrization . . . . .	64
3.3	Preliminary Simulations using the BG-AAEM-CT Model . . . . .	65
3.3.1	Lattice Constant Investigation . . . . .	65
3.3.2	Structure and Charge Distribution . . . . .	67
3.3.3	Melting . . . . .	68
3.4	Discussion . . . . .	71
<b>4</b>	<b>Structure, Thermodynamics, and Solubility in Tetromino Fluids . . . . .</b>	<b>73</b>
4.1	Introduction . . . . .	73
4.2	Methodology . . . . .	77
4.2.1	The Model . . . . .	77
4.2.2	Simulation details . . . . .	79
4.3	Results . . . . .	85
4.3.1	Single-component (pure) fluids . . . . .	85
4.3.2	Two-Component Systems . . . . .	93
4.3.3	Many-Component Systems . . . . .	103
4.3.4	Analysis of Virial Coefficients . . . . .	106
4.3.5	Solubility and solvation . . . . .	111
4.4	Discussion . . . . .	115
<b>5</b>	<b>Polyomino Fluids and Crystals . . . . .</b>	<b>123</b>
5.1	Mathematical Research on Polyominoes . . . . .	123
5.1.1	Enumeration . . . . .	124
5.1.2	Tiling . . . . .	125
5.2	Simulation details . . . . .	126
5.2.1	Change from binary to integer representation . . . . .	126
5.2.2	Expanded lattice . . . . .	127
5.2.3	Modified convergence heuristics and block averaging . . . . .	127
5.3	Vacancy Thermodynamics . . . . .	128
5.4	Pentomino results . . . . .	132
5.4.1	Overview . . . . .	132
5.4.2	Pentominoes without a phase transition . . . . .	133
5.4.3	Isotherms of pentominoes with phase transitions . . . . .	139
5.4.4	<i>Y</i> and <i>P</i> shapes: transition to a disordered phase . . . . .	140
5.4.5	<i>X</i> shape: transition to an ordered crystal . . . . .	143
5.4.6	<i>Z</i> shape: phase transitions and polymorphism . . . . .	143
5.5	Columnar behavior . . . . .	153
5.5.1	Theory . . . . .	153
5.5.2	Squares . . . . .	154
5.6	Shapes that exhibit “diagonal” columns . . . . .	156
5.7	“Square-like” shapes . . . . .	161
5.7.1	Two-component systems . . . . .	168
5.7.2	Future Work . . . . .	170

<b>References . . . . .</b>	<b>172</b>
-----------------------------	------------



# List of Tables

2.1	Feuston-Garofalini re-parametrizations by evolutionary strategies. The fittest parameter sets from Figure 9 are shown, as well as the original FG parametrization. Parameter names and units are as given in [61]. Only “fitted” parameters are given in the table; other parameters (cutoffs, reference angles, and formal charges) are kept fixed at their literature values [61]. . . . .	48
3.1	Parameter set for the BG-AAEM-CT model. This is one of many parameter sets tested. For many of the parameters not related to charge-transfer, values used are similar to those in the BKS or FG models. . . . .	66
4.1	Average size of clusters of each shape, from simulations at $\beta\mu_i = 7.0$ for all $i$ , for the mixtures shown in Figures 4.8 and 4.12. Statistical uncertainty in these data is $\pm 0.005$ at 95% confidence. . . . .	105
4.2	Matrix of second virial coefficients $B_{ij}$ . Note that these coefficients are exact. . . . .	107
4.3	Matrix of “orientation-specific second virial coefficients” $B'_{ij}$ . The orientations of each piece are numbered according to the scheme described in Figure 4.1. These coefficients are exact. . . . .	108
4.4	Solubility ( $1/\beta K_i$ ) of each shape in various solvents at $\beta p = 0.5$ . Values given are certain to within $\pm 0.002$ . The first column contains the packing fraction of the solvent, $\eta_s$ . The first seven rows of the table show the solubility of each shape in the pure fluids of each other shape. The diagonal values are missing because Henry’s law does not apply to components of the solvent. The next three rows show the solubility of various shapes in each of three binary mixtures, with both mixture components at the same chemical potential. The row labeled “Senary” shows the solubility of each shape in a 6-component mixture composed of all the other shapes, again all at the same chemical potential and $\beta p = 0.5$ ; these solvents do not all have the same packing fraction, but they vary over only a small range, given in the $\eta_s$ column. The final row gives the average of the solubility of each shape in the six other pure solvents; note that this quantity does not have a rigorous thermodynamic interpretation, and is only given for the sake of comparison. . . . .	113

5.1	Distribution of dense phase compositions for $Z$ pentominoes at $\beta\mu = 8.0$ , past the phase transition point. This data was gathered through simulations lasting over 1.1 trillion Monte Carlo moves for each system, beginning from an empty lattice in each case. . . . .	146
-----	---	-----

# List of Figures

2.1	Variation of optimization profile with number of configurations in the training set. Training set sizes used ranged from 4 to 320 configurations. The quantity plotted is the fitness of the fittest (lowest $\chi^2$ ) member of the current parent population at each generation averaged over ten independent runs. . . . .	26
2.2	Variation of optimization profile with random number sequence. 20 independent runs (starting from the same initial population) are shown, along with averages over the full set of 20, the first 10, and the last 10. Run conditions are the “default” algorithm, corresponding to the 128-configuration data shown in Figure 1. . . . .	28
2.3	Radius of gyration for 10 individual runs and their average. This calculation corresponds to the 128-configuration data shown in Figure 1. . . . .	30
2.4	. . . . .	31
2.5	Variation of optimization profile with choice of recombination operator. Operators tested include: (R-1) local discrete, (R-2) none, (R-3) local intermediate, (R-4) global discrete, (R-5) global intermediate, (R-6) local discrete for parameters and intermediate for $\sigma$ , (R-7) global discrete for parameters and intermediate for $\sigma$ , (R-8) local discrete for the first 250 generations, none for the subsequent 1750. . . . .	34
2.6	Variation of optimization profile with mutation size control algorithm. Algorithms tested include: (M-1) independent $\{\sigma_i\}$ , (M-2) constant $\sigma$ , (M-3) annealing $\sigma$ by a constant factor, (M-4) adjustment of $\sigma$ relative to early $\chi^2$ , (M-5) history-dependent, diversity-preserving algorithm, (M-6) alternative history-dependent, diversity-preserving algorithm. . . . .	39
2.7	Variation of optimization profile with choice of selection operator. Operators tested include: (S-1) non-overlapping truncation, (S-2) overlapping truncation, (S-3) non-overlapping truncation plus best parent, (S-4) non-overlapping truncation plus best-ever individual, (S-5) non-overlapping 2-way tournament, (S-6) overlapping 2-way tournament, (S-7) non-overlapping 8-way tournament, (S-8) overlapping 8-way tournament. . . . .	42
2.8	Simulated annealing optimizations. As in Figure 2, ten independent runs (starting from the same point) are shown, as well as their average. . . . .	45

2.9	Fitting the FG functional form to the CPMD training set. FD-1 is the default method in the meta-optimization tests. FD-2 uses local, intermediate recombination, and other options as in FD-1. FD-3 uses local, intermediate recombination and simple annealing mutation size control, and other options as in FD-1. FD-4 uses local, intermediate recombination and non-overlapping truncation plus best-ever individual selection, and other options as in FD-1. FD-5 uses local, intermediate recombination and non-overlapping 8-way tournament selection, and other options as in FD-1. . . .	46
3.1	The charge-transfer function ( $f(R_{ij})$ ) for the AAEM-CT model shown in graphical form. At small separation, the full amount $\delta q$ is transferred, while the amount transferred goes smoothly to zero outside a certain range.	59
3.2	AAEM-CT model energies for a $\beta$ -cristobalite cell. In this crystal, the silicon atoms occupy lattice sites of a diamond structure, with oxygen atoms bridging between them. The lattice constant on the y axis is that of the Si-O bond distance. . . . .	60
3.3	$\beta$ -cristobalite energy versus lattice constant for BG-AAEM-CT and AAEM-CT models. The dashed line indicates the experimental value, which is near the minimum for the BG-AAEM-CT curve in this Figure. . . . .	67
3.4	Oxygen-oxygen and silicon-oxygen radial distributions functions for BG-AAEM-CT and BKS models. Crystals simulated at 3000 K, 1 bar and the amorphous phase at 5000 K, 1 bar, with a duration of 1 ns. . . . .	69
3.5	Oxygen and silicon charge distributions for amorphous and crystal phases of the BG-AAEM-CT model. Systems simulated at 3000 K, 1 bar for crystals and 5000 K, 1 bar for the amorphous phase, with a duration of 1 ns. . .	70
3.6	Density versus temperature from isobaric-isothermal simulations of the BG-AAEM-CT and BKS models. The amorphous phase is more dense than $\beta$ -cristobalite, hence the BKS model density rises upon melting of the crystal. All simulations performed at 1 bar, with a duration of 1 ns. . . . .	71
4.1	The seven one-sided tetrominoes, with corresponding names and symbols, and rotation centers/anchor points marked by “+” symbols. Orientations are labelled numerically, starting at 1. Squares have one orientation, rod, S and Z shapes have two, and J, L and T shapes have four. The shapes shown above are all in orientation 1; subsequent orientations correspond to 90° or 180° clockwise rotations around the marked points. . . . .	78
4.2	(a) Packing fraction $\eta$ versus chemical potential $\beta\mu$ for one-component fluids. (b) Pressure $\beta p$ vs. packing fraction for one-component fluids. The color scheme in these plots is the same as for the shapes themselves (Figure 4.1). . . . .	87

4.3	Isothermal compressibility $\chi_T$ versus chemical potential $\beta\mu$ for one-component fluids. . . . .	88
4.4	Configurations of pure fluids of squares and rods, at low (-1.0), medium (+3.0) and high (+7.0) chemical potentials. These are $38 \times 38$ sections cut from $64 \times 64$ simulation cells; as a result, pieces may extend over the boundary of the section shown. For the rods, which have two possible orientations, each orientation is shown in a slightly different color. . . . .	89
4.5	Configurations of pure fluids at low (-1.0), medium (+3.0) and high (+7.0) chemical potentials, for each of the $S$ , $L$ and $T$ shapes. These are $38 \times 38$ sections cut from $64 \times 64$ simulation cells; as a result, pieces may extend over the boundary of the section shown. As in Figure 4.4, each orientation is shown in a slightly different color. . . . .	90
4.6	An example herringbone packing motif for an orientational interface of $S$ -shapes, commonly observed in high density snapshots. . . . .	92
4.7	Contour plots of packing fraction versus chemical potentials for (top) mixtures of squares and rods, and (bottom) mixtures of $S$ and $Z$ shapes. . . . .	95
4.8	Snapshots taken from simulations of mixtures of squares and rods at (top) $\beta\mu_O = 0.0$ , $\beta\mu_I = 6.0$ , (middle) $\beta\mu_O = \beta\mu_I = 4.0$ , (bottom) $\beta\mu_O = 6.0$ , $\beta\mu_I = 0.0$ . These are $38 \times 38$ sections cut from $64 \times 64$ simulation cells; as a result, pieces may extend over the boundary of the section shown. Rods are all shown in the same color regardless of orientation. . . . .	96
4.9	Snapshots taken from simulations of a mixture of $S$ and $Z$ shapes, at $\beta\mu_S = \beta\mu_Z = 4.0$ , (top) without orientation-specific coloration, and (bottom) with orientation-specific coloration. . . . .	97
4.10	Average sizes of clusters of squares and rods in square/rod mixtures, along the $\beta\mu_O = \beta\mu_I$ phase space diagonal. . . . .	99
4.11	Contour plots of volume of mixing versus pressure $\beta p$ and mole fraction $x$ for various binary mixtures: (a) squares and rods, (b) squares and $S$ shapes, (c) rods and $Z$ shapes, (d) rods and $T$ shapes, (e) $S$ shapes and $Z$ shapes, and (f) $Z$ shapes and $L$ shapes. In all cases the mole fraction shown is that of the first shape of the pair. All figures are plotted on the same vertical scale, in relative percentage units, $(\Delta V_{mix}/V) \times 100\%$ . . . . .	100
4.12	Representative snapshots of selected three-, four-, five-, six- and seven-component mixtures, with all species at $\beta\mu = 7.0$ . These are $38 \times 38$ sections cut from $64 \times 64$ simulation cells; as a result, pieces may extend over the boundary of the section shown. All pieces of a given shape are shown in the same color, regardless of orientation. . . . .	104
5.1	The 18 one-sided pentominoes. Some enantiomeric pairs are labeled with a single letter, “primed” and “unprimed”. Colors indicate the presence, absence, and type of phase transition. Yellow indicates no phase transition, blue indicates transition to a disordered phase, and red indicates transition to a crystalline phase or phases. . . . .	132

5.2	Isotherms of pentominoes without a phase transition. Data for each isotherm was gathered via “sequentially” seeded simulations. Each state point in an isotherm is separated by $0.05 \beta\mu$ . . . . .	134
5.3	Pentominoes that do not display phase transitions, each at $\beta\mu = 11$ . In this and other snapshots, pieces are shaded differently according to orientation. The blue and purple shades differ in rotation by 180 degrees, as do the yellow and orange shades. Each snapshot shows a section of the full simulation cell. From top left to bottom right (reading order): $T, N, W, L$ . . . . .	135
5.4	Additional pentominoes that do not display phase transitions, all at $\beta\mu = 11$ . Each snapshot shows a section of the full simulation cell. From top left to bottom right (reading order): $V, F, U$ . . . . .	136
5.5	Pentomino rods at $\beta\mu = 11$ . Orientation-specific clustering of groups of rods into larger rectangular (often square-like) shapes is the dominant form of packing. . . . .	139
5.6	Isotherms of pentominoes that display phase transitions (data averaged over 5 runs). State points in each isotherm are separated by $0.05 \beta\mu$ ; individual points are shown only for the $X$ data. Differences between enantiomers appear due to small sample size. . . . .	140
5.7	$Y$ pentomino snapshots at $\beta\mu = 9.50$ and $\beta\mu = 11.00$ (pre- and post-transition). . . . .	141
5.8	$P$ fluid, at $\beta\mu = 10.15$ and $\beta\mu = 11.00$ (pre- and post-transition). . . . .	142
5.9	$X$ pentomino snapshots: before transition at $\beta\mu = 3.650$ and after transition at $\beta\mu = 3.70$ . . . . .	142
5.10	$X$ pentomino isotherms, including both the forward and reverse branches. Significant hysteresis occurs in this system. . . . .	144
5.11	The six periodic tilings of the $Z$ pentomino. These are found through backtracking (a form of exhaustive enumeration for tilings), not simulation. These unit cell size on the underlying square lattice widely varies for these tilings. . . . .	144
5.12	Doubly-degenerate vacancies in type 3 and type 1 $Z$ polyomino crystals. These are the only $Z$ polymorphs with multiply-degenerate states created upon formation of a single vacancy. . . . .	147
5.13	Pre-transition snapshot of $Z$ fluid at $\beta\mu = 7.75$ . Note the presence of many different crystalline nuclei of varying shape, structure and orientation. . . . .	149
5.14	Post-transition snapshot of $Z$ at $\beta\mu = 8.75$ . This configuration is dominated by a large domain of type 2 crystal, and a smaller domain of type 3 crystal. . . . .	150
5.15	Post-transition snapshot of $Z$ at $\beta\mu = 9.30$ with domains of type 2 crystal and type 1 crystal. . . . .	151
5.16	A system at $\beta\mu = 8.0$ with two type 1 crystal domains of different orientation and a domain of type 3 crystal. . . . .	152

5.17	Isotherm of $3 \times 3$ squares. This data was collected using the same protocol as the isotherm data for $X$ shapes, with the reverse branch seeded from a perfect crystal. . . . .	155
5.18	Snapshot of $3 \times 3$ squares at $\beta\mu = 5.950$ . Columnar behavior is evident. . .	156
5.19	Entropy versus packing fraction for $3 \times 3$ squares. This data was gathered through thermodynamic integration, using the virial equation of state for zero-density extrapolation and then continuing the integration from low-density states to near unit packing fraction states. . . . .	157
5.20	Isotherms of $4 \times 4$ squares, with forward and reverse branches. This system displays a first-order phase transition. . . . .	158
5.21	Snapshot of $4 \times 4$ squares at $\beta\mu = 6.950$ . Columnar order dominates in this system. . . . .	158
5.22	The four fish-like shapes examined in this study. From left to right: the “short tail” gold fish, “long tail” goldfish, “enlarged” fish, and “fat” fish. . .	159
5.23	(A) Size 6 fish shape isotherm. No phase transition is observed. (B) Snapshot of this system at $\beta\mu = 15$ . . . . .	160
5.24	Isotherms for the size 11 “long tail” fish, which may undergo a phase transition to one of two crystal phases. . . . .	161
5.25	The liquid phase of size 11 fish at $\beta\mu = 8.2$ , shortly below a phase transition, and in two crystal polymorphs post-transition. . . . .	162
5.26	Isotherms for the “enlarged long tail” size 15 fish. This system undergoes a phase transition to a single crystal without translational freedom. . . . .	163
5.27	Solid phase of “enlarged long tail” size 15 fish, with stripes of opposite directions. . . . .	163
5.28	The “fat fish” isotherm, displaying a columnar transition. This diagonal columnar transition was “by design”. . . . .	164
5.29	The “fat fish” just below (left) and above (right) the chemical potential for the phase transition. . . . .	164
5.30	The size 12 “big cross” (or, $X$ ) and size 13 “diamond” shapes. . . . .	165
5.31	(A) Isotherms for a size 12 “ $X$ ” polyomino. Hysteresis is observed with the phase transition. (B) Snapshot of the size 12 “ $X$ ” polyomino crystal at $\beta\mu = 5.0$ . The “interlocking” columns remove translational freedom for single vacancies. . . . .	166
5.32	(A) Isotherms for the size 13 “diamond” polyomino. Hysteresis is observed in this system as well. (B) Snapshot of the size 13 “diamond” polyomino at $\beta\mu = 5.5$ . . . . .	167
5.33	A 2D isotherm of the size 12 “big cross” (label j) and size 13 “diamond” (label i) shapes from $\beta\mu = 2$ to 10 on each axis. The isotherm uses a “color temperature” scale to indicate density, with blue locations indicating low density and red locations indicating high density. . . . .	169

# Glossary

**6-31G\*** A Pople-style basis set with Gaussian-type orbitals of polarized double- $\zeta$  quality, for use in quantum mechanics calculations.

$\beta\mu$  Referred to as a “chemical potential”, temperature ( $T$ ) and chemical potential ( $\mu$ ) variables cannot be separated in our athermal grand canonical ensemble. Hence, they appear together in  $\beta\mu$ .

**AAEM-CT** Alavi, Alvarez, Elliot and McDonald Charge-Transfer model. This empirical model uses the local environment of atoms to determine charges and charge-transfer forces at each timestep. Calculation of its charges, energies, and forces for use in molecular dynamics or Monte Carlo simulations is relatively inexpensive.

**AM1** Austin Model 1. A semi-empirical electronic structure method which uses the modified neglect of differential diatomic overlap approximation.

**AMBER** Assisted Model Building with Energy Refinement. An empirical, non-reactive force field and software package which is commonly used in biochemical simulations. This model contains point charges, dispersion, bond, angular, and torsional terms.



**BG-AAEM-CT** Barnes-Gelb modification of the AAEM-CT Model. In this work we introduce new potential terms which are active between atoms that are transferring charge. These modifications to the AAEM-CT model are useful in isobaric-isothermal ensemble simulations. The AAEM-CT model is also reparametrized, its empirical two-body form changed, and a three-body term introduced.

**BKS** van Beest, Kramer and van Santen model. A popular empirical potential for silica simulations, with fixed, fractional point charges. It does not rely upon harmonic bond expressions and may simulate phase transitions.

**cc-pVTZ** A Dunning-style basis set with Gaussian-type orbitals of polarized triple- $\zeta$  quality, for use in quantum mechanics calculations.

**CPMD** Car-Parrinello Molecular Dynamics. This acronym may refer to the simulation technique which allows for relatively inexpensive “*ab initio*” molecular dynamics using DFT energies, or the software package which implements the CPMD technique and several other DFT methods.

**CPU** Central Processing Unit. The part of a computer which executes instructions of a program. Modern CPUs typically have multiple cores, each capable of carrying out instructions independently. Sometimes, casual usage of “CPU” may actually refer to a specific core executing instructions.

**DFT** Density Functional Theory. A high level quantum mechanical electronic structure theory which is often used to calculate the energies of many-body systems, such as molecules in the gas phase or condensed matter systems. While modern DFT calculations are not technically *ab initio* (relying on parametrized exchange-correlation functionals), it is often referred to as an *ab initio* technique. DFT formalism has  $O(N^3)$  scaling, making it quite popular.

- EA** Evolutionary Algorithm. A class of iterative global optimization techniques which typically use ideas drawn from biological evolution and natural selection. Evolutionary Strategies and Genetic Algorithms are both types of Evolutionary Algorithm.
- ES** Evolutionary Strategy. An Evolutionary Algorithm which operates on phenotypic representations of its trial solutions, which in our case are sets of real numbers (as opposed to bitwise representations). Its iterative steps include recombination, mutation, evaluation, and selection.
- FG** Feuston-Garofalini model. A reactive empirical potential for vitreous silica and aqueous silicate systems with formal point charges on atoms and both two-body and three-body terms. Our group has used this model for simulation of silica sol-gel reactions.
- GA** Genetic Algorithm. An Evolutionary Algorithm which operates on genotypic (bitwise) representations of its trial solutions. GAs are quite similar in spirit to Evolutionary Strategies, but the technical details of the recombination and mutation steps are not at all similar to an ES, which leads to different behavior during global optimizations.
- GCC/gfortran** GNU Compiler Collection, gfortran compiler. This is one of the most commonly used compilers for the Fortran 77 and Fortran 90/95 languages, and is freely available with any Linux distribution.
- L2 cache** Level 2 cache for a CPU. This storage unit provides access to a program's data and instructions at speeds significantly faster than a computer's main memory. This is a matter of hardware: static RAM for L2 cache versus dynamic RAM for main memory. It is quite advantageous to be able to fit time-sensitive parts of a program in L2 cache.

**MC** Monte Carlo. The statistical mechanical technique – this often refers to Metropolis Monte Carlo simulations.

**MM3** Molecular Mechanics 3 force field. A non-reactive empirical model with point charges, dispersion, bond, angular and torsion terms. MM3 was designed for simulations of hydrocarbons and biochemical systems.

**MPI** Message Passing Interface. This is an Application Programming Interface (API) specification for communication between computers. It is language-independent, but most frequently used with C, C++, Fortran, and Python languages. MPI is commonly used in High Performance Computing (HPC) due to the need for parallel programs to communicate between nodes on computer clusters.

**PBE** Perdew, Burke, Ernzerhof exchange-correlation functional. Also referred to as PBE96. This functional operates on the electronic density and density gradient of a system in order to calculate the many-particle contribution to a DFT energy calculation.

**Polyomino** Connected shape on a two-dimensional square lattice. A tetromino is a polyomino which occupies four lattice sites, and a pentomino is a polyomino which occupies five lattice sites.

**PM3** Parameterized Model number 3. A semi-empirical electronic structure method which uses the neglect of differential diatomic overlap approximation, similar to AM1.

**QEq** Charge Equilibration technique. A method for calculating the distribution of charges within a molecule, where charges are allowed to change over time depending upon the local environment. Developed by the Goddard group, this method significantly differs from the AAEM-CT approach.

**QM** Quantum Mechanical or Quantum Mechanics.

**ReaxFF** The “ReaxFF” force field. A reactive empirical potential which has been parametrized for both hydrocarbons and some silicate species. This method has point charges, dispersion, bond order (instead of harmonic bonds), angular, and torsional terms. Charges on atoms are determined by a QEq technique.

**RDF** Radial Distribution Function [ $g(r)$ ]. A description of variation in atomic density as a function of distance for a particular pair of atom types. For an atom at the origin  $O$  and an average number density  $n = N/V$ , the local density at a distance  $r$  from  $O$  is  $n \cdot g(r)$ . A commonly referenced function in statistical mechanics.

**RSL** Rahman, Stillinger, Lemberg model, or potential terms. Stillinger and co-workers originally developed an atom-based, dissociable model for liquid water using only two-body terms in the 1970s. RSL may refer to the model studied by them, or to the two-body terms which were used to control hydrogen bond distances in liquid water. These RSL terms are a part of the FG model, which was used in our meta-optimization work.

**SA** Simulated Annealing. A stochastic global optimization technique inspired by annealing in metallurgy. The method is based upon the Metropolis Monte Carlo algorithm, and features a fictitious “temperature” which is gradually lowered and acts as a control on the optimization’s search.

# Chapter 1

## Overview

This thesis is composed of two parts. The first is a study of evolutionary strategies for parametrization of empirical potentials, and their application in development of a charge-transfer potential for silica. The second is a study of thermodynamics and self-assembly in a particular class of athermal two-dimensional lattice models. In both parts, computational efficiency and performance were important goals, and this was reflected in method and program development.

### **1.1 Development and Application of Evolutionary Strategies for Potential Parametrization**

Empirical potentials are commonly used in molecular dynamics and Monte Carlo simulations, especially in studies of systems containing large numbers of particles. Our group had previously used the Feuston-Garofalini (FG) model [1] for aqueous silicate systems in large-scale simulations of silica sol-gel formation [2]. It was our intent to perform simulations with more accurate electrostatics and possibly additional elements, not present in the

FG model. This would first require improvement and reparametrization of the model, itself not a trivial task.

Therefore, we first investigated available methods for efficient reparametrization of empirical potentials. In particular, we focused on two global optimization techniques: evolutionary strategies (ES) [3–5] and simulated annealing [6]. Evolutionary strategies are potentially well-suited for parametrization of empirical potentials, as they are easily parallelizable across hundreds of processor cores. However, the performance of evolutionary strategies depends on the values of parameters and details used. There are many such items to specify, and they have domain specific effects. In Chapter 2, we address this through the “meta-optimization” of an evolutionary strategy for empirical potential fitting. This was the first comprehensive investigation of the performance of evolutionary strategies for empirical potential fitting, and several interesting results were found that may be useful to future researchers. This chapter includes figures and portions of text which the author has previously published: reprinted (adapted or in part) with permission [7]. Copyright 2007 American Chemical Society.

Chapter 3 describes our subsequent attempts to improve upon existing potentials for silicate systems. Elements in the FG model have fixed formal charges. During simulations of chemical reactions this leads to inaccuracy in the local electrostatic environments. We identified a promising and inexpensive charge-transfer model by Alavi and coworkers (AAEM-CT model) which we believed could be easily adapted for our needs, as it had previously been used on an amorphous silica system [8]. Combining the charge-transfer terms from the AAEM-CT model with empirical two-body and three-body forms from other popular potentials, we believed we could develop a new model for silica and aqueous silicate species. Initial attempts at parametrization of such a potential using evolutionary strategies, however, led to systems with physically unrealistic properties. Closer investigation

of the AAEM-CT model led to discovery of a fundamental flaw not noticed in prior work. We partially corrected this flaw, leading to a model with a much improved description of crystalline and amorphous phases of silica. We decided not to pursue this charge-transfer form for studies involving additional elements. In particular, despite many attempts, we were unable to find a parameter set (by ES or otherwise) that displayed an accurate melting point for  $\beta$ -cristobalite silica, which we took to be a reasonable test criterion.

## 1.2 Thermodynamics and Self-Assembly of Polyominoes

In a separate project, we conducted extensive studies of a simple lattice model in order to better understand the self-assembly of small molecules and nanoparticles adsorbed at interfaces. Specifically, we studied hard polyominoes on a square lattice [9–11]. Polyominoes are two-dimensional objects of varying size and shape; the polyominoes in our simulations only interact through a non-overlap condition. As a result, all of the behavior observed is entropically driven.

We first considered the tetrominoes, which are discussed in Chapter 4. These are all the same size, covering four lattice sites. A highly efficient Monte Carlo code was developed for these simulations, which were conducted in the grand ensemble. We determined the equations of state for the pure fluids and all binary mixtures, and also studied many other multicomponent systems. The one-component fluids all displayed self-ordering at higher densities. This clustering is discussed, and in the case of multicomponent systems, quantified. Analysis of second virial coefficients was useful in explaining the frequent species-specific clustering and orientations seen within clusters and mixtures. Using multicomponent simulations, we were able to calculate Henry’s law solubility constants for species within a solvent of a different species. We were also able to calculate the volumes

of mixing for binary mixtures, many of which displayed unexpected and complex non-ideal behavior. This chapter includes figures and portions of text which the author has previously published: reprinted (adapted or in part) with permission [12]. Copyright 2009 American Chemical Society.

We then went on to study larger polyominoes, which are discussed in Chapter 5. None of the tetrominoes underwent any kind of phase transition, but we did observe first-order phase transitions in species as small as the pentominoes. The family of pentominoes contained shapes with no transitions, transitions to a disordered phase, and with transitions to a crystalline phase. Some polyominoes exhibited polymorphism, undergoing phase transitions to many possible crystal domains. The frequency and properties of these different crystals are examined. Columnar phases (ordered phases that have translational freedom in one direction) were observed in many systems. We were also able to design a polyomino with a diagonally oriented columnar phase. Finally, preliminary studies of a binary mixture were also performed, including simulation and analysis of a large two-dimensional equation of state.



## **Chapter 2**

# **Meta-Optimization of Evolutionary Strategies for Empirical Potential Development: Application to Aqueous Silicate Systems**

### **2.1 Introduction**

Empirical potentials (force fields) are widely used in molecular modeling and simulation, and usually consist of analytic functions which have been parametrized to reproduce selected reference data. The functional forms are chosen to model specific intermolecular and intramolecular interactions thought to be important for a given application. For instance, in the potentials commonly used for studying the phase behavior of fluids one generally includes terms describing atomic-core repulsions, dispersion forces, bond angles, and torsions; if dipolar or charged species are present, these may be described using point

dipoles or distributions of point charges. By inclusion of higher multipoles and/or polarizabilities, such potentials can become quite complex. The design of effective potentials has been discussed extensively in the simulation literature and the functional forms used vary considerably from problem to problem [13–17].

Over the course of a molecular dynamics or Monte Carlo simulation, millions of sequential energy and calculations may have to be performed. In the case of a molecular dynamics simulation, forces will also have to be calculated for each of those configurations. It is almost always impractical to do these calculations using quantum mechanical calculations, as any given energy calculation may take up to several hours, or longer, depending upon size of the system and accuracy of the methods used. Prior to roughly 25 years ago, *ab initio* molecular dynamics calculations were not possible for any system size or method due to their computational expense. Empirical “force fields” or “potentials” are the solution to this problem. Accuracy is sacrificed for speed, although a carefully parametrized force field may often be capable of quite accurately reproducing several experimental quantities. Empirical force field equations generally involve classical mechanics instead of quantum mechanics. Further, they usually simplify the electrostatics of a system, using point charges and possibly dipoles instead of multipole expansions to describe charge distributions. Molecular orbitals from quantum mechanics which provide the framework for a molecule’s bonds are replaced, most commonly, by harmonic bond oscillators or rigid rods between atoms. The energy levels of these harmonic bonds or rigid rod rotations are not quantized. Many-body interactions are uncommon. A typical biochemical force field describing an amino acid will have two-body bond terms, three-body angle terms, and four-body dihedral terms. Further, since those two-body bonds are usually harmonic bonds, they are non-dissociating and therefore non-reactive bonds. All of this framework results

in greatly increased computational speed compared to atomic orbital, quantum mechanical based methods. The largest part of the computational expense is usually calculation of Coulomb interactions for the system, as those are long ranged and cannot be truncated at a cut-off distance where they become negligible. The formal scaling of the Coulomb interaction is  $O(N^2)$ , although advanced algorithms such as the Ewald summation may reduce this cost to  $O(N^{\frac{3}{2}})$ , or  $O(N \ln N)$  for the case of particle mesh Ewald or fast multipole methods. These empirical potentials attempt to reproduce the full N-dimensional potential energy surface of a system, hence their common name of “potentials”.

Parameters may be fit to a wide range of data, including both experimental results and quantities calculated using first-principles or semi-empirical electronic-structure methods. Experimental data often used for this purpose include, among others, crystal structures, thermophysical properties such as melting points and critical parameters, partial radial distribution functions, angular distributions, and diffusion constants. Parametrization against thermophysical quantities requires the use of simulations to determine the corresponding properties of trial parameter sets, which can be computationally expensive.

With first-principles methods one may calculate the energies and associated gradients for selected molecular configurations, as well as charge distributions, multipole moments, and structural quantities. Such data may be obtained either for isolated molecules or in the condensed phase. The parametrization of empirical potentials against first-principles reference data is now a popular and widely-used approach [18–28], building on both the broad availability of software for high-quality electronic structure calculations and general interest in multi-scale simulation methods.

In all cases, systematic parametrization of the chosen functional form presents a challenging numerical problem. This may be cast as the optimization of an objective function that

measures the ability of the empirical potential to reproduce selected reference data, and therefore as a minimization in some high-dimensional space where the dimensionality is equal to the number of parameters to be assigned. The values being optimized when fitting potentials are usually point charges, Lennard-Jones or exponential interactions, bond angles, and similar quantities. This is a non-linear optimization: the quantities being optimized are often not linear coefficients of equation terms, and this places restrictions on the mathematical methods which may be used to find solutions. For example, it cannot be treated as an eigenvalue problem and solved with matrix inversion.

In general, the properties of the objective function will depend on the physical system under consideration, reference data, potential form, and metric used to compare model results with reference data. For a given parametrization problem there may well exist a multiplicity of possible solutions, as pointed out in the early literature in development of the central force model for liquid water [29–31]. This model relied upon physical reasoning for selection of a set of two-body forms to describe hydrogen and oxygen atoms, for which parameters were determined to select forms for their two body potential, and then parameters were calculated which gave proper values for the dipole moment and harmonic force constants of an isolated water molecule. The authors chose a set of two-body functions, and then calculated parameters for those forms which would reproduce the dipole and force constants. They noted that their final set of functions was “one of an infinity of such sets which satisfy the criteria outlined above”.

Many strategies for parametrization of empirical potentials are available, varying in both computational complexity and “philosophy” [13–17]. One significant classification of these strategies is whether all parameters are considered simultaneously or if a sequential, one-parameter-at-a-time (or one-term-at-a-time) approach is used; the latter cases may also be iterated.

Iterated parameter-by-parameter optimizations correspond roughly to direction-set optimization methods [32], and therefore deterministically produce local minima of the objective function. Term-by-term optimizations (which may consider a few parameters at a time) are popular because they reflect the additivity of different interactions explicitly built into many potentials. For instance, one may parametrize a torsional motion independently of the associated angular terms by using an electronic structure program to scan over the torsional degree of freedom, and then fit that data with some appropriately chosen function. The disadvantage of this approach is that the resulting torsion is then fit at particular values of the associated angles, and any dependence of the torsion on the associated angles will not be described well. To capture such interactions one must have both reference data that explores appropriate deformations of the molecule and additional terms in the potential that depend on both torsions and angles. In such a case, one may choose either to individually fit the torsion-only and angle-only terms and then fit the “cross” term, or to fit all three parts simultaneously. The term-by-term approach allows for a better description of the isolated motions with inaccuracies concentrated in the cross-term, whereas the simultaneous fitting will spread inaccuracies more evenly among the three terms. Such issues become particularly important when extending previously developed potentials to include new atomic or molecular species. If the existing potential is not re-parametrized to some degree, then the inaccuracies associated with the (necessarily imperfect) description of interaction with the new species will be concentrated in the added terms. Conversely, when all parameters are fit simultaneously this will not be the case, but parts of the potential may not be as accurate as the functional form allows. The global optimization may use the large parameter search space to compensate for some deficiency elsewhere in the functional form. For example, a term describing van der Waals attractions may be optimized to an unphysically strong value in order to compensate for unrealistic point charge Coulombic interactions.

The ReaxFF family of reactive potentials [18–23], for instance, is parametrized against small molecule calculations for bond distances and angles and experimental data for heats of formation. A local optimization technique of successive one-parameter optimization (line search) was used [33]. In an alternative approach, Voth *et al.* have used first-principles simulations of condensed phases to create potentials for water and hydrogen fluoride [24, 25]. Their “force matching” technique uses a short-ranged cubic spline and a long-ranged Coulomb form to model site-site interactions. Splines are mathematically convenient as they are polynomials with well-behaved derivatives and which may be summed using linear coefficients to describe arbitrary curves. The linearly independence of splines enable the use of singular value decomposition to exactly find parameters for a given configuration, and a final set of parameters is then determined by averaging over the results of many configurations.

For potentials describing a small number of degrees of freedom (and therefore either very small systems or species of low structural complexity) electronic structure calculations can be used to “scan” over the complete potential energy surface. These results can then be numerically interpolated, fit to analytical functions, or some combination of both, in order to obtain highly accurate potentials. Recent examples of such parametrizations include the water potential of Bukowski *et al.* [26] and the nine-dimensional potential for collisions of hydrogen gas and water monomers developed by Faure *et al.* [27]; there is a considerable literature on the development of such surfaces for use in reaction dynamics calculations [34–37].

In the 1960s and 1970s, three groups developed independently numerical optimization methods which mimicked the process of evolution [4, 38]. Rechenberg and Schwefel created a family of “evolutionary strategies” to solve real-valued problems [39–43]. Fogel

researched artificial intelligence problems through an “evolutionary programming” technique [44]. Lastly, Holland developed “genetic algorithms” as a general optimization method [45]. Interestingly, the development of these similar but distinct types of algorithms seems to have been furthered by the geographical separation of the groups performing the work; there were essentially no instances of authors publishing with both the American and German groups. De Jong discusses all these methods under a unified framework of “evolutionary computation”, and generalizes them as “evolutionary algorithms” [46].

A brief outline of an evolutionary strategy is as follows. First, a population of trial solutions, called parents, is created. Second, a *recombination* process creates a group of children by averaging or otherwise combining parts of the parents. Third, the children undergo *mutation*, consisting of small random changes. Fourth, those children are *evaluated*. Fifth, a *selection* process is used to select a new group of parent from the current population. The cycle is then repeated, starting with the recombination step.

One important difference between evolutionary strategies and genetic algorithms is in the representation of trial solutions: evolutionary strategies are phenotypic, and genetic algorithms are genotypic [47]. That is, in an evolutionary strategy the individuals are manipulated “as-is”, whereas genetic algorithms operate on bitwise representations. This difference in representation requires different operators for recombination and mutation steps. In genetic algorithms, recombination operators exchange strings of bits between two parents in order to generate children, and the basic mutation operator is a random bit flip. For a continuous-valued problem represented phenotypically, the recombination step would involve choosing or averaging values from the parents to create a child, and the simplest mutation would be the random displacement of selected child parameters. In general, this is a difference in “data structures” for the trial solutions and it has a significant effect on

how an program is written. Converting a program from operating as an evolutionary strategy to operating as a genetic algorithm or vice-versa is possible but may take significant effort to properly and efficiently implement.

Genetic algorithms (GAs) have been used in potential development in a number of studies, mostly to extend semi-empirical methods or to refine popular force fields. Cundari, Deng and Fu used a GA to parametrize technetium interactions in the semi-empirical PM3 method. Semi-empirical QM methods use pre-parametrized overlap integral calculations to speed up the evaluation of molecular energies. Therefore, reparametrization of the integrals for specific problems may lead to increased accuracy. Their results were fit against crystal structure geometries, and they found that their GA provided significantly better parameters than those obtained by interpolating parameters of the metals to the left and right of technetium in the periodic table [48]. Rossi and Truhlar used a GA to re-parametrize the AM1 semi-empirical method against quantum mechanical data in order to perform semi-quantitative direct dynamics on the Cl + CH<sub>4</sub> potential energy surface [49]. Parameters for organic systems containing sodium and transition metals in the AM1 and PM3 methods have also been refit using GAs [50,51]. These targeted re-parametrizations can allow semi-empirical methods give substantially improved structures for biochemically relevant systems. Ge and Head used dual genetic algorithms in a study of Si<sub>x</sub>H<sub>y</sub> clusters, with one GA tasked to iteratively re-parametrize the AM1 method, and the other GA to search cluster geometries for a global minimum [52]. GAs have also been used in computer-aided molecular design [53]. As reviewed by Lameijer *et al.* [54], in the area of drug design evolutionary algorithms have been applied to the design of molecule libraries, conformational analysis, molecule superposition and pharmacophore detection, quantitative structure–activity relationships (QSAR), ligand docking, *de novo* design, and “drug-likeness” evaluation. In



particular, Thomsen investigated the effects of variation operators and local-search hybrid methods on EA/GA performance for ligand docking [55].

Strassner *et al.* performed one of the few studies of the influence of GA parameters in the context of developing empirical potentials. They examined the interaction of crossover rates, mutation rates, and selection methods on the overall GA performance for refitting of the MM3 force field for a rhenium complex [28, 56]. In this study, different GA parameter sets were compared via the root-mean-squared deviation (rmsd) between experimental (or high-level theoretical) crystal structures and those obtained using the GA-parametrized force field; GAs which produced MM3 parameters with smaller rmsd's were judged to be more effective. Results were averaged over only three different independent optimizations for each set of GA parameters, and definite trends in GA performance with different parameters were observed. The most efficient algorithm tested was a simple GA with a tournament selector, 90% crossover rate and 20% mutation rate. Wolohan *et al.* re-parametrized the MM3 force field for copper complexes [57] using the GA parameters recommended by Strassner *et al.* [28, 56]. Other efforts at re-parametrizing force fields using GAs include partial re-parametrization of the AMBER force field [58], refitting of the BKS and TTAM potential forms [59], and refitting of the Stillinger-Weber potential for silicon [60].

With the exception of the work of Strassner *et al.* [28, 56], the actual performance of the GAs used in potential parametrization work has rarely been considered in any depth. Many previous studies of the efficiency of evolutionary strategies have considered only the optimization of relatively simple and low-dimensional mathematical functions [4, 38]. The behavior of an ES for much more complex problems may be distinctly different.

In this chapter we evaluate the performance of a reasonable selection of evolutionary strategy algorithms applied to the problem of optimizing an empirical potential for molecular

simulation applications. The process of finding the best algorithm for an optimization is termed a “meta-optimization”. The empirical potential we consider is the all-atom, reactive potential for aqueous solutions of silicate oligomers developed by Feuston and Garofalini (FG) [1, 61]. Reparametrization of the FG potential is a useful test application because the short-ranged nature of the potential makes it inexpensive to evaluate and optimization of the large number of parameters used poses a difficult numerical problem. The purposes of this chapter are to provide effective guidelines for future applications of evolutionary strategies in similar parametrization studies, and to provide benchmarks for the behavior that can be expected of these algorithms.

## 2.2 Methodology

### 2.2.1 Evolutionary Strategy Optimizations

A complete evolutionary strategy implementation requires specification of initialization, recombination, mutation, evaluation, selection, and termination algorithms. In this chapter we evaluate the performance and behavior of a variety of recombination, mutation, and selection methods in the parametrization of an empirical potential against various reference data.

Individuals (parents and children) will be represented as vectors of real numbers  $\mathbf{x} = \{x_i, \sigma_i\}, i = 1, \dots, N$ , where  $N$  is the number of parameters. The  $\{x_i\}$  are the quantities to be optimized (in this case, parameters of an empirical potential), and the  $\{\sigma_i\}$  are associated quantities that control the size of mutations applied to each parameter. The  $\{\sigma_i\}$  may themselves be subject to evolution. While they do not affect the evaluation of the potential,

they affect the optimization process and its ability to both escape and pinpoint local minima in parameter space. The parts of the evolutionary strategy are presented below.

1. *Initialization.* In this step an initial population of  $m$  parents is created. Each parameter  $x_i$  of each parent is selected from a continuous uniform distribution within a constrained range,  $x_i^{min}$  to  $x_i^{max}$ , which are part of the initial input. Selecting random seeds is not a necessity – values may be picked by hand – but a random approach was used so the process was unbiased. The initial values of the  $\{\sigma_i\}$  are defined through scaling of an input parameter  $\sigma_0$ :  $\sigma_i = \sigma_0 \cdot (x_i^{max} - x_i^{min})$ . This reflects the fact that the absolute values of the  $x_i$  can vary by many orders of magnitude, depending on the units and functional forms used.

2. *Recombination.* Recombination is the process of combining parents to produce children. Following Schwefel, recombination operators are classified as *local* or *global*, and also as *discrete* or *intermediate* [3]. Local operators generate a child entirely from two randomly selected parents. Global operators randomly select a new pair of parents *for each parameter* of every child. Discrete operators assign each  $(x_i, \sigma_i)$  pair for the child by setting them equal to the value of the corresponding  $(x_i, \sigma_i)$  pair in one of the randomly chosen parents. Intermediate operators instead assign the average value of the corresponding parent parameters to the child. Selections are made “without replacement”, so that it is not possible to create a child from two “copies” of a single parent.

3. *Mutation.* Each parameter  $x_i$  in each child  $\mathbf{x}$  is displaced with probability  $p$  by a random number chosen from a normal distribution of zero mean and standard deviation  $\sigma_i$ ,  $G(0, \sigma_i)$ . This change is represented as:

$$x_i = x_i + G(0, \sigma_i) \tag{2.1}$$

The  $\sigma_i$  control the size of mutations. As discussed in greater detail below, different mutation algorithms may independently evolve the  $\{\sigma_i\}$  over the course of the optimization. Alternatively, the  $\{\sigma_i\}$  may be controlled through a common reference  $\sigma$ , with  $\sigma_i = \sigma \cdot (x_i^{max} - x_i^{min})$ ; various algorithms for evolving  $\sigma$  may then be applied.

4. *Evaluation.* The fitness of each new child is evaluated, as described in the next section.

5. *Selection.* In the selection step, the parents of the next generation are selected from the current population. Selection methods may be categorized according to (a) whether or not they allow overlapping generations and (b) their degree of *elitism*.

Evolutionary strategies are commonly labeled either  $(m, n)$ -ES or  $(m + n)$ -ES, where  $m$  is the number of parents and  $n$  is the number of children per generation [62]. An  $(m, n)$ -ES is non-overlapping: the  $m$  parents of the next generation are chosen only from among the  $n$  children of the current generation. An  $(m + n)$ -ES is overlapping: the  $m$  parents of the next generation are chosen from the entire current population of  $n + m$  individuals. This allows for the survival of individuals for more than one generation, and potentially indefinitely [3].

Elitism describes the importance placed on fitness when selecting the next generation's parents. *Truncation* methods are the most elitist, and simply choose the best  $m$  individuals from the available population ( $n$  or  $m + n$ ). A less elitist method is *binary tournament* selection, in which  $m$  random pairs are chosen from the available population, and the “winner” of each pair is made one of the parents for the next generation [63]. With tournament methods, it is possible that the individual with the highest fitness is not selected. The tournament method may be extended to have competitions between an arbitrary number of children when creating a child, e.g. a three-way tournament instead of a binary (two-way) tournament. The truncation selection method is deterministic, while the tournament method is stochastic. We use the term *semi-overlapping* to refer to selection methods which, when

choosing new parents (from either the children or from the full population), always include either the best current parent or the best current individual.

After selection, one generation is complete. The  $m$  selected individuals now become the parents, and the algorithm returns to the recombination step.

6. *Termination.* Common termination options include exiting after a certain fitness has been achieved, exiting when the fitness of the fittest individual becomes constant to within a specified tolerance, or exiting after a fixed number of generations. In the studies below, which compare various algorithms, termination criteria are chosen to ensure that the computational costs of the different methods are comparable. For algorithms with the same  $m$  and  $n$ , this corresponds to termination after a fixed number of generations, but for comparisons of algorithms with different  $m$  and  $n$ , optimizations are terminated after a fixed number of child evaluations, or “births.”

### 2.2.2 Fitness Function

Our goal in potential parametrization is to have the empirical potential accurately reproduce some reference data, which we will call the *training set*. It is called this because the empirical potential is being “trained” to reproduce the data in the training set. Here the training set will consist of the total energies of a series of  $N_{config}$  atomic configurations. The *fitness function* is defined as

$$\chi^2(\mathbf{x}) = \frac{1}{N_{config}} \sum_i^{N_{config}} [\{E_{emp}(\mathbf{R}_i, \mathbf{x}) - E_{emp}(\mathbf{R}_{ref}, \mathbf{x})\} - \{E_{TS}(\mathbf{R}_i) - E_{TS}(\mathbf{R}_{ref})\}]^2 \quad (2.2)$$

where  $E_{emp}(\mathbf{R}_i, \mathbf{x})$  is the energy of configuration  $\mathbf{R}_i$  determined using the empirical potential with parameters  $\mathbf{x}$ .  $E_{TS}(\mathbf{R}_i)$  is the energy of configuration  $\mathbf{R}_i$  determined using some

high quality method, for instance Density Functional Theory (DFT).  $\chi^2(\mathbf{x})$  is a measure of the mean-squared difference between the potential energy surfaces sampled by the training set and defined by the chosen empirical functional form and parametrization  $\mathbf{x}$ .

$\mathbf{R}_{ref}$  denotes a reference configuration, which is included in the definition of  $\chi^2$  because the empirical potential and reference method may differ in ways which make absolute comparisons of their energies impossible. For instance, the energies obtained from typical all-atom empirical potentials cannot be directly compared with the “raw” output of electronic structure calculations. This is because in electronic structure methods even isolated atoms have non-zero total energy due to their internal structure, which is generally not the case for empirical potentials. One possible solution to this problem is to use the energy at the dissociation limit (all atomic separations increased to infinity) to define the energy “zero” in each case, which corresponds to a particular choice of  $\mathbf{R}_{ref}$ . However, for many empirical potentials, including non-dissociable molecular potentials and potentials that include non-integral charges, this is an awkward choice. In this study, we chose the lowest-energy configuration in the training set as the reference state  $\mathbf{R}_{ref}$ . This choice is applicable regardless of the form of empirical potential used, and requires no additional “reference” calculations. Furthermore, it has the appeal of directly including the differences in energy between “relevant” configurations of the reference system, which appear in the Boltzmann factors determining the thermodynamic properties of the system.

### 2.2.3 Application

Our test problem for meta-optimization of evolutionary strategies is a re-parametrization of the Feuston and Garofalini (FG) potential for aqueous solutions of silicate oligomers [1,61]. The FG potential includes a modified Born-Mayer-Huggins [64, 65] functional form and

Rahman-Stillinger-Lemberg [30] (RSL) terms for two-body interactions, and three-body terms as introduced by Stillinger and Weber [66]:

$$V_2(\mathbf{r}_i, \mathbf{r}_j) = A_{ij} \exp\left(\frac{-r_{ij}}{\rho_{ij}}\right) + \frac{Z_i Z_j}{r_{ij}} \operatorname{erfc}\left(\frac{r_{ij}}{\beta_{ij}}\right) + \sum_{m=1}^{D_{ij}} \frac{a_{ij,m}}{1 + \exp(b_{ij,m}(r_{ij} - c_{ij,m}))} \quad (2.3)$$

$$V_3(\mathbf{r}_{ij}, \mathbf{r}_{jk}, \theta_{jik}) = \lambda_{jik} \exp\left[\frac{\gamma_{ij}}{r_{ij} - r_{ij}^o} + \frac{\gamma_{ik}}{r_{ik} - r_{ik}^o}\right] \times (\cos \theta_{jik} - \cos \theta_{jik}^o)^2 \quad (2.4)$$

The two-body part has a damped Coulomb potential (in fact, this is the real space part of the Ewald summation for calculating Coulomb interactions), an exponential repulsion, and a soft (and short-ranged) attraction. Note that a different number  $D_{ij}$  of RSL terms are used for each type of two-body interaction involving hydrogen (Si-H, O-H, and H-H). The three-body term penalizes deviation from a specified angle  $\theta_{jik}^o$ , controlled by parameters for cutoff distance, magnitude, and rate of decay. This is an all-atom, dissociable potential and can be used to study chemical reactions in solution, including the hydrolysis and condensation of siloxane bonds and the early stages of sol-gel processing [1, 2, 61].

The FG potential was fit to thermophysical quantities including the radial distribution functions and angular distribution functions of melt-quenched silica. The short-ranged repulsive term was parametrized using a formula based upon ionic radii and charges. The other parameters were chosen based on hydrogen-bond energies, cluster geometries and liquid state properties extracted from molecular dynamics simulations, although how trial parameter sets were chosen for these simulations was not described.

The FG potential has two-body parameters for all combinations of the elements Si, O, and H, and parameters describing four different three-body combinations (Si-O-Si, H-O-H, O-Si-O, and Si-O-H), for a total of 55 adjustable parameters. In this investigation, 45 were optimized, and 10 were kept at fixed values because of physical arguments. The fixed parameters include the charges on each atom type, five three-body cutoff distances  $r_{ij}^o$ , and the four preferred angles  $\theta_{jik}^o$ . The atomic charges were kept at their formal values (+1 for hydrogen, +4 for silicon, -2 for oxygen) so that dissociation produced ions with the correct integer charges. The three-body cutoff distances and angles ensure that all silicon and oxygen atoms prefer tetrahedral geometries, except for those oxygens in a water-like environment, which prefer the experimental angle of  $104.5^\circ$  found in liquid water.

#### 2.2.4 Training Sets

Two types of training set were used in this study, both consisting of configurations sampled from molecular dynamics simulations of an aqueous solution of three silicate species. Each configuration in both sets contained one of each of silicic acid, disilicic acid, and cyclotrisilicic acid molecules and 64 water molecules, in a cubic box of 1.4014 nm edge length for a total density of 1.0 g/cc. These species were chosen because they are the initial components of silica oligomerization and gel formation in aqueous systems, a topic of interest to our group.

The first type of reference data, used below in the meta-optimization of the evolutionary strategy, consisted of configurations sampled according to the FG potential and the associated FG energies. These data were generated using a molecular dynamics trajectory thermostatted (via the Gaussian isokinetic method [14]) at 300 K, with configurations sampled



at intervals of 2 ps. As in previous studies using this potential, interactions were truncated at 7 Å.

The second training set was generated using Car-Parrinello Molecular Dynamics (CPMD) simulations [67], also in the canonical ensemble. In these calculations the Perdew-Burke-Ernzerhof (PBE) functional [68] was used with a plane-wave basis with 30 Rydberg cutoff for the wavefunction and 150 Rydberg cutoff for the density. Vanderbilt ultrasoft pseudopotentials were used for all atoms [69]. The silicon pseudopotential featured a non-linear core correction. This level of theory was checked by comparing optimized bond distances, bond angles, and hydrogen bond strengths with similar data obtained with the same PBE functional, and the 6-31G\* and cc-pVTZ basis sets in Gaussian03 [70]. The plane-wave results were closer to the 6-31G\* basis results, giving bond lengths within 0.005 Å and similar hydrogen bond strengths.

Four visibly and temporally distinct configurations were selected from the first training set. These were used as the starting points for the CPMD simulations. For each configuration, the following procedure was followed. First, each configuration was optimized to a root-mean-square force of 0.005 a.u. Next, the configuration was relaxed through a series of eleven 200-step CPMD simulations using a 3.0 a.u. timestep and a 400.0 a.u. fictitious mass for the electrons. A velocity rescaling thermostat was used, with a target temperature of 300 K and rescaling whenever the temperature of the ions was more than 37.5 K away from the target value. After the first six 200-step simulations, the convergence criterion for the gradient of the wavefunction was tightened from  $10^{-5}$  to  $10^{-6}$  a.u. Between each 200-step simulation the electrons were quenched back to the Born-Oppenheimer surface. This ensures the nuclear and electronic wavefunctions are simultaneously minimized. After the relaxation procedure was finished, the production CPMD run was started. The production run used a Nosé-Hoover thermostat for each degree of freedom [71]. The temperature was

300 K with a thermostat frequency of  $2500.0 \text{ cm}^{-1}$  for the ions and  $10000.0 \text{ cm}^{-1}$  for the electrons. These simulations ran for 10000 steps, giving a total of 242 fs of data in each of the four CPMD simulations, or nearly 1 ps total data. From these trajectories, 370 evenly-spaced configurations were selected. Single point energies were then calculated for each configuration; these differ slightly from the CPMD energies because during the dynamics run the electrons are not quenched to the Born-Oppenheimer surface at each timestep. These configurations and single-point energies make up the second training set. The program “CPMD version 3.9.2”, was used for these calculations [72].

### 2.2.5 Implementation

We have developed a computer code to optimize empirical potentials against training sets of the type described above. Our program implements several optimization techniques, including evolutionary strategies, a simple direct search minimizer, an unconstrained Powell line search algorithm, simplex simulated annealing [73] and Metropolis simulated annealing [6]. The direct search minimizer and Powell algorithm are deterministic, local optimization methods. The simplex and Metropolis simulated annealing methods are global search techniques similar in strategy, of which the Metropolis simulated annealing will be described in detail later. Several potentials are implemented, including the the Lennard-Jones model, central force water model, FG model, and a charge-transfer model [8]. Additional potentials may be easily added.

The program is parallelized using the Message Passing Interface (MPI) library for Fortran in two ways. In evolutionary strategy optimizations, evaluation of the fitness of the  $n$  children in each generation is divided over many processors by assigning some number of children to each processor. In other optimization techniques, which do not involve the

simultaneous evaluation of many trial solutions, the evaluation of a single  $\chi^2$  may be parallelized by the distribution of training-set configurations among multiple processors and the simultaneous evaluation of many of the  $E_{emp}(\mathbf{R}_i)$  terms. Evolutionary strategy speedups were found to be nearly ideal using up to 16 processors, while the training-set decomposition approach is slightly less efficient due to the increased quantity of communication required. The parallel scalability is also different for the two approaches. For algorithms that only evaluate one trial solution at a time, the theoretical maximum number of processors that can be used is equal to the number of configurations in the training set. Evolutionary strategies, on the other hand, evaluate many individuals in parallel, with each processor handling an equal number of individuals. Therefore, if a very large number of processors is available (as is increasingly the case with modern multi-core processors), cases where  $n > N_{cpu} > N_{config}$  allow evolutionary strategies to scale higher than other methods. Finally, evolutionary strategies can be further parallelized by distributing the evaluation of each  $\chi^2$  among several processors (as in the single-evaluation methods), which could then be used even for  $N_{cpu} > n$ , and for all methods, even the evaluation of the energy of a single configuration could be spread across several processors using either domain-decomposition or replicated-data strategies.

## 2.3 Meta-optimization of evolutionary strategies

The evolutionary strategy may itself be optimized for a particular class of problems by selection of appropriate population sizes, recombination methods, mutation size control schemes, and selection methods. In this study this will be accomplished by optimizing the FG functional form against reference data (training sets) generated using the FG potential itself. Since the functional form is unchanged, it is in principle possible for an optimization

algorithm to reduce  $\chi^2$  to zero (within some numerical tolerance), which would occur at the exact FG parameters;  $\chi^2(\mathbf{x}_{\text{FG}}) = 0$ . Different ES algorithms will approach this limit more or less quickly, and with different “profiles” of  $\chi^2$  vs. generation.

Testing different evolutionary strategies is accomplished here by first selecting a “default” combination of population size, recombination method, selection method, etc., and then considering and comparing several alternatives for each of these components. Note that this approach does not consider all possible combinations of methods, but does allow for controlled comparisons of different variants of the same operator (for instance, mutation size control schemes).

The default options were selected based on a large number of preliminary trials and recommendations from the literature discussed above. They consist of populations of  $m = 8$  and  $n = 96$ , local discrete recombination, mutation size control using evolving independent  $\sigma_i$  and an initial  $\sigma_0 = 0.03$ , and non-overlapping truncation selection.

Unless otherwise stated, all individual optimizations were truncated after 192000 function evaluations, which took roughly 27 wall-clock hours running on two Opteron 250 (2.4 GHz) CPUs. Near-linear scaling of parallel performance was observed in additional tests on up to 16 CPUs; all calculations were performed on a cluster of dual-processor nodes each with 2-4 GB of RAM, networked using Infiniband interconnects.

### 2.3.1 Preliminary studies

In equation (2), each configuration provides only one energy datum. Therefore, the number of configurations in the training set must exceed the number of parameters to be optimized. Training set size may affect the reliability, speed and smoothness of optimizations. These

effects are shown in Figure 2.1, which compares training sets of varying sizes. Each optimization profile in Figure 2.1 consists of the lowest parent  $\chi^2$  at each generation, averaged over ten independent optimizations (see below). Two of the profiles, using 4 and 16 configurations, are for optimizations against too few independent data to be meaningful. These optimizations have considerably different profiles than the others, rapidly finding parameter sets with very low  $\chi^2$ , which is perhaps not surprising given that in these cases this can be satisfied in a large fraction of parameter space.

All the other traces are quite similar, both in the shape of the profile and the lowest  $\chi^2$  reached after the allotted simulation time. In Figure 2.1 all optimizations were run to between 1500 and 2000 generations. Based on the similarity of these data, a training set size of 128 configurations was chosen for use in all the calculations that follow. This is significantly greater than the number of free variables (45), and requires less CPU time than the larger sets of 192, 256 or 320 configurations while clearly retaining the same general properties.

Data are plotted in log-log form in this and subsequent figures. It is therefore important to note that the absolute decrease in  $\chi^2$  is much larger in the early generations than in later ones. The units of  $\chi^2$  are  $[(\text{kJ/mol}) \text{ per configuration}]^2$ . The initial values of  $\chi^2 > 10^5 (\text{kJ/mol})^2$  correspond to the randomly generated parent populations described above, which are clearly of poor quality. The final values of  $\chi^2$  (for meaningfully large training sets) do not converge to zero in the allotted number of generations, but instead tend to reach values near  $100 (\text{kJ/mol})^2$ . The meaning of this value can be assessed by performing simple perturbations of various parameters from their original FG values, and measuring the resulting change in  $\chi^2$ . This measure can then be averaged over perturbations of all the parameters. Single-parameter perturbations of  $\pm 0.1\%$  increase  $\chi^2$  to  $0.392 (\text{kJ/mol})^2$ , on average. Deviations of  $\pm 1\%$  increase  $\chi^2$  to  $39.17 (\text{kJ/mol})^2$ , on average, and deviations of

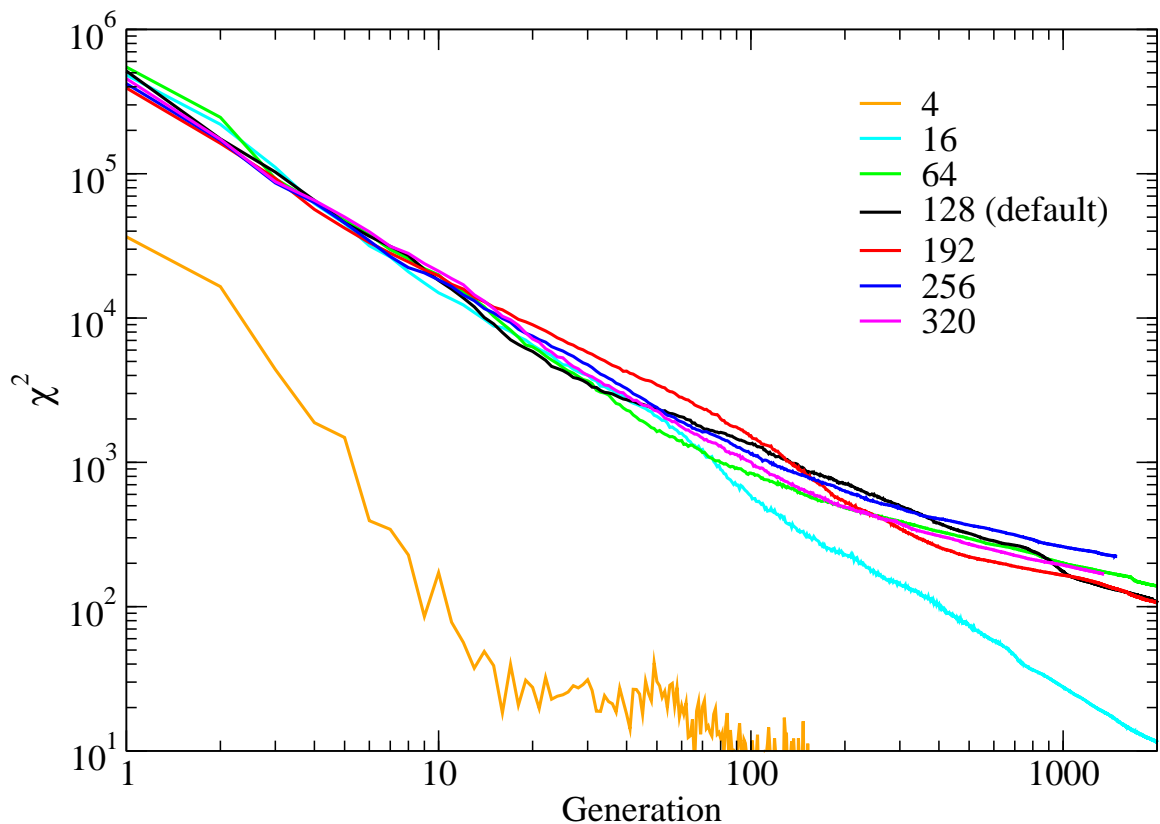


Figure 2.1: Variation of optimization profile with number of configurations in the training set. Training set sizes used ranged from 4 to 320 configurations. The quantity plotted is the fitness of the fittest (lowest  $\chi^2$ ) member of the current parent population at each generation averaged over ten independent runs.

$\pm 10\%$  increase it to  $3812.5 \text{ (kJ/mol)}^2$ , on average. Thus, final values near  $100 \text{ (kJ/mol)}^2$  correspond roughly to parameters that have converged to within 1% of their optimal values. However, the sensitivity of  $\chi^2$  to such deviations varies considerably from parameter to parameter. Sensitive parameters include the  $\rho_{ij}$  parameters for the Buckingham exponential repulsions between oxygen and hydrogen atoms and between oxygen and silicon atoms, and the position  $c_{ij}$  of the second RSL oxygen-hydrogen term (which is important for modeling hydrogen bonding).

In any single optimization run,  $\chi^2$  fluctuated strongly because the recombination and mutation steps are stochastic. In order to make meaningful comparisons of different ES algorithms, we therefore present  $\chi^2$  profiles averaged over over multiple independent runs. “Independent” in this case means differently re-seeding the random number generator for each run after generation of the initial population. The different runs therefore have the same “starting point”. We determined that ten independent runs were sufficient to reliably profile different evolutionary strategy variants. This was done by performing twenty runs and then comparing the averaged profiles of two different sets of ten runs with the average profile of all twenty runs. As shown in Figure 2.2, the average of either set of ten runs is quite similar to the average of all twenty runs. Note that this is not the case for averages over only three independent runs, as used by Strassner *et al.* [28, 56]. Each of the twenty individual runs is also plotted in order to illustrate the magnitude of variation between runs. It is clear that the shape of the optimization profile can vary considerably from run to run, and also that the final fitness values can vary by approximately one order of magnitude between runs started from the same initial population. As in Figure 2.1, all subsequent figures will show the  $\chi^2$  for the best parent in each generation averaged over 10 runs, unless noted otherwise. Further analysis of the variations between individual runs will be presented in section 2.5.

Genetic diversity is a measure of the difference between members of a population. If members of the population differ only slightly, then a population has low genetic diversity. We measure this through a radius of gyration  $R_g$ , defined as:

$$x_i^{ave} = \frac{1}{m} \sum_{j=1}^m x_{i,j} \quad (2.5)$$

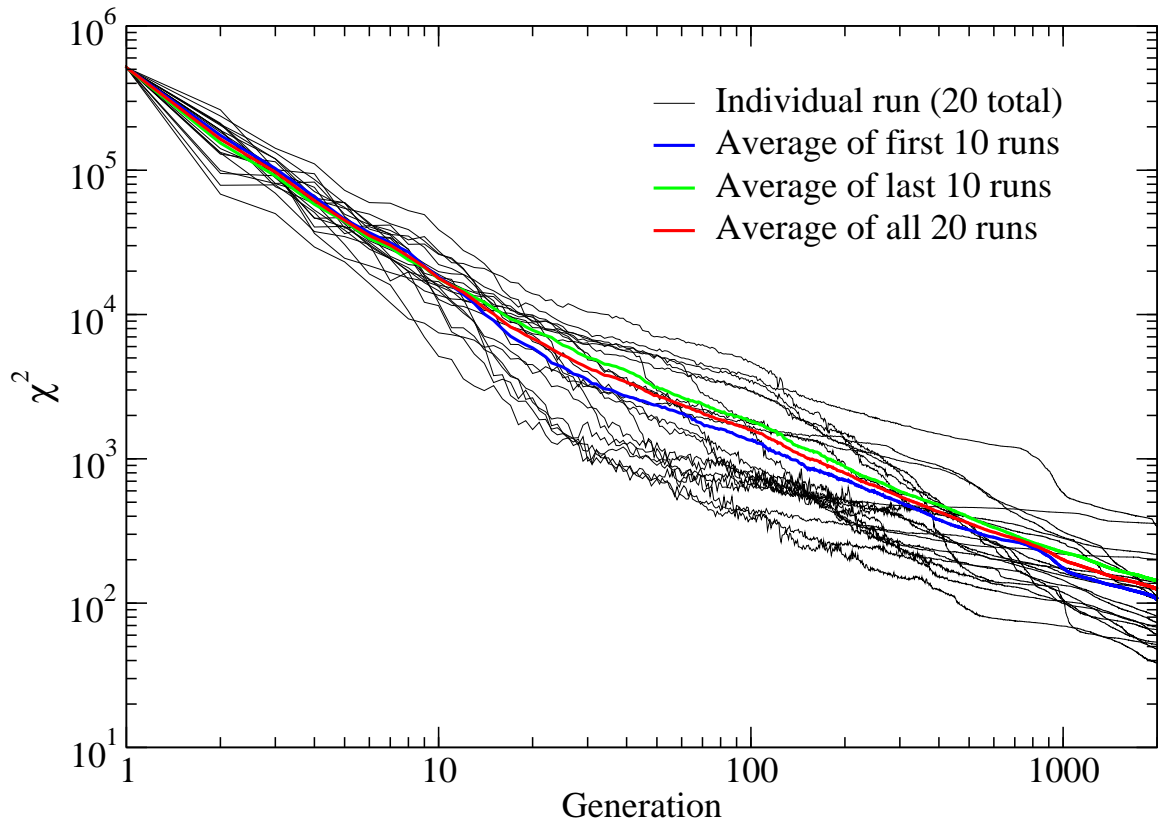


Figure 2.2: Variation of optimization profile with random number sequence. 20 independent runs (starting from the same initial population) are shown, along with averages over the full set of 20, the first 10, and the last 10. Run conditions are the “default” algorithm, corresponding to the 128-configuration data shown in Figure 1.



$$R_g^2 = \frac{1}{m} \sum_{j=1}^m \sum_{i=1}^N \left( \frac{x_{i,j}}{x_i^{ave}} - 1 \right)^2 \quad (2.6)$$

where  $x_{i,j}$  is the value of parameter  $i$  in parent  $j$ . Genetic diversity is an important quantity in ES optimizations. If there is too little genetic diversity then the entire population will become trapped in a single minimum. While this is generally the end result of an evolutionary optimization, it is important that it not happen too early in the calculation, before a large part of parameter space has been explored.  $R_g$  data for the default ES strategy are shown in Figure 2.3. This is a strongly fluctuating quantity, but shows clear structure. The initial  $R_g$  is large. After approximately 10 generations (corresponding to a reduction of  $\chi^2$  from approximately  $5 \times 10^5$  to around  $10^4$ , see Figure 2.2)  $R_g$  drops to a plateau near 0.3, where it remains for approximately 250 generations. Over this period  $\chi^2$  decreases by another two orders of magnitude. After this,  $R_g$  begins to diminish quickly, becoming very small by the late generations.

### 2.3.2 Population

For an  $(m,n)$ -ES, a parent:child ( $m:n$ ) ratio of 1:4 has been recommended [38], although many studies use larger ratios [74]. Having a very high ratio of children to parents is considered inefficient, since the vast majority of computational time is spent evaluating individuals which do not survive to the next generation. However, in preliminary work we found that a  $m:n$  ratio of 1:12 seemed more effective. The effects of changing the numbers of children and parents, and the ratio  $m:n$ , are therefore of interest in further optimizing the ES approach.

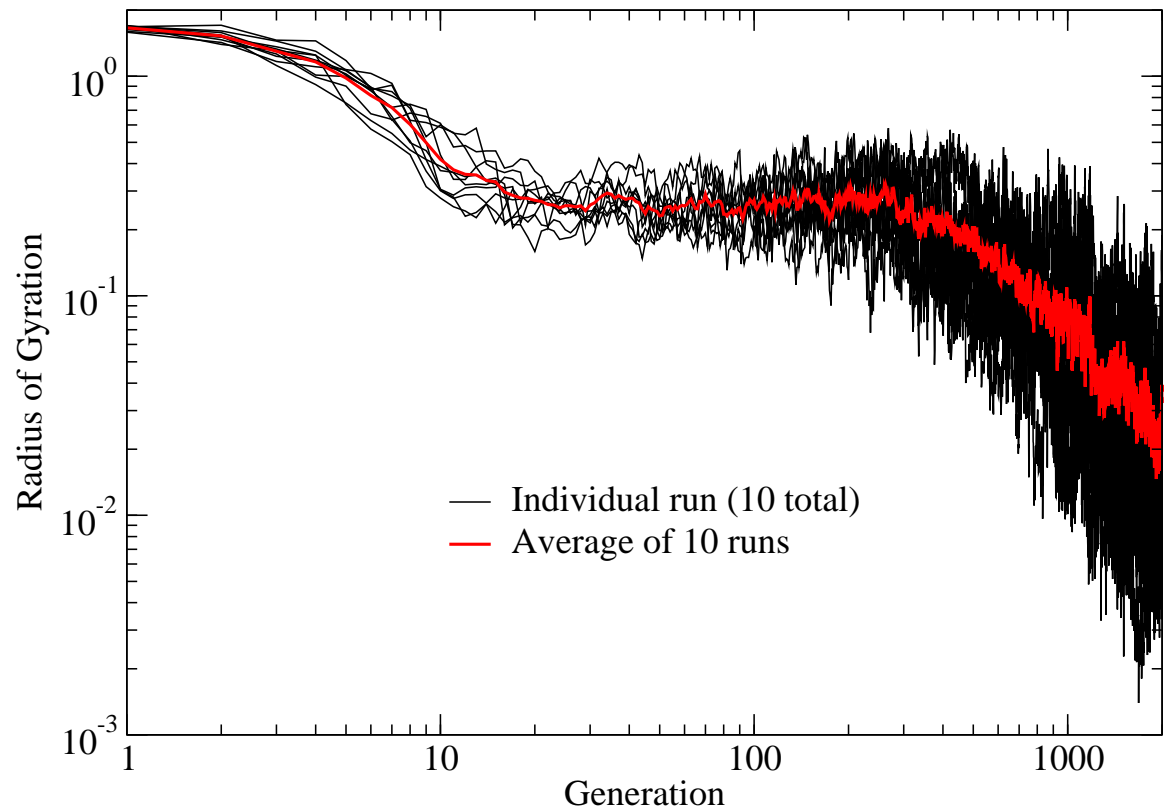


Figure 2.3: Radius of gyration for 10 individual runs and their average. This calculation corresponds to the 128-configuration data shown in Figure 1.

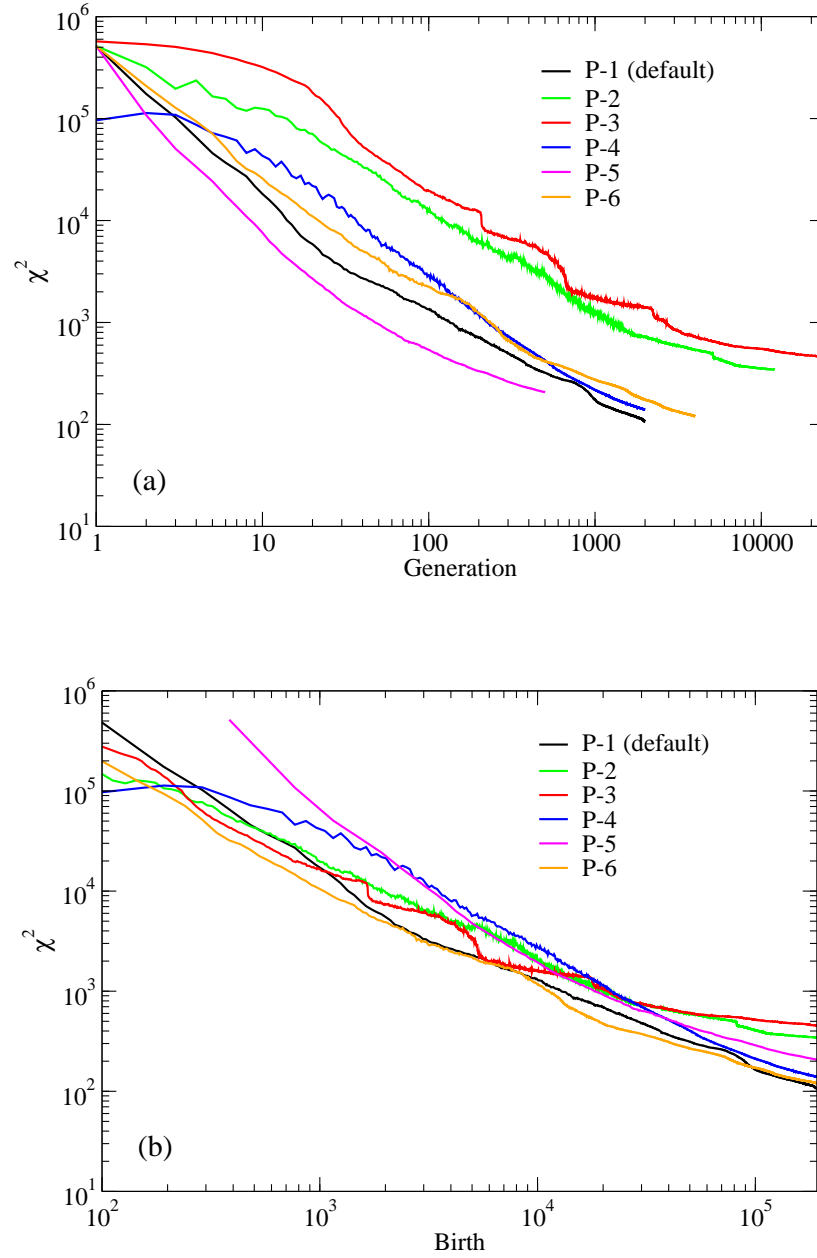


Figure 2.4: Variation of optimization profile with numbers of parents and children. Tested are: (P-1) 8 parents and 96 children, (P-2) 8 parents and 16 children, (P-3) 1 parent and 8 children, (P-4) 48 parents and 96 children, (P-5) 8 parents and 384 children, (P-6) 8 parents and 48 children. Top: optimization profiles vs. number of generations. Bottom: optimization profiles vs. number of births.

In Figure 2.4,  $(m,n)$ -ES choices of (8,96), (8,16), (1,8), (48,96), (8,384), and (8,48) are compared, labeled P-1 through P-6, respectively. As explained above, each variant was terminated after a total of 192000 fitness function evaluations, corresponding here to different numbers of generations. The best initial fitness value among the parents for any  $(m,n)$ -ES with same number of parents is the same. The profile of P-3 (1,8) has a slightly worse initial best fitness than any  $m = 8$  ES, while P-4 (48,96) has an initial best fitness over five times smaller than any  $m = 8$  ES. This is not surprising: a initial population with  $m = 48$  instead of  $m = 8$  has a much larger probability of containing a parent with low  $\chi^2$ .

Comparing the P-1 (8,96) and P-4 (48,96) data shows the benefit of having a smaller parent:child ratio. In P-4,  $\chi^2$  actually increases over the first few generations. This can occur when the fittest parents are either not chosen in the recombination step or chosen so infrequently that a child more fit than those parents is not produced. As the selection method in the default strategy does not allow parents to survive to the next generation, the fitness of the best individual may increase from generation to generation.

P-3 is less effective than the other strategies throughout, but especially at early times. With only one parent, there cannot be recombination. Therefore, fitness can only be improved by random mutation of the single initial parent. Distinct jumps can be seen near generations 200, 600 and 1100, when especially productive mutations occurred. These data are again averaged over ten independent runs, and each of these jumps actually corresponds to a very large drop in  $\chi^2$  in an individual run.

Comparing strategies with  $m = 8$  shows that an increase in the number of children leads to larger decreases in  $\chi^2$  per generation during the early stages of the optimization. P-5 (8,384) has the largest initial decreases in  $\chi^2$  per generation, followed by P-1 (8,96), P-6 (8,48) and P-2 (8,16), in that order. However, the use of large numbers of children is

generally avoided because it is both computationally more expensive (per generation) and it tends to more quickly reduce genetic diversity. This can be understood as follows. In the (8,384) optimization, there are only 36 unique pairs of parents, each of which will produce, on average, 10.67 children per generation. If the children of a single pair of parents are particularly fit and truncation selection is used (as is the default here), then the *entire* next generation of parents may consist of the offspring of that pair of parents, and will have very low genetic diversity. As the ratio of  $m$  to  $n$  is increased, more of the current group of parents will likely contribute to the next generation, and genetic diversity will be preserved. Of the populations tested in Figure 2.4, P-1 (8,96) achieves the lowest  $\chi^2$  after the allotted time and appears to make the most effective compromise between genetic diversity and  $\chi^2$  reduction per generation. This finding has implications for the use of evolutionary methods on massively parallel computers. Increasing the number of children,  $n$ , may appear to be an efficient way to utilize many processors in an optimization, but then  $m$  must likewise be increased to prevent loss of diversity. Furthermore, increasing both  $m$  and  $n$  does not necessarily improve the rate of convergence of the algorithm in a cost-effective way; this is easily seen in Figure 4b, wherein the performance of method P-6 measured against the number of births is clearly superior to the other algorithms at nearly all times, with only P-1 pulling very slightly ahead after  $10^5$  births.

### 2.3.3 Recombination

Our default algorithm was local, discrete recombination. This is the most commonly used recombination operator and is procedurally similar to the method used in genetic algorithms. Various recombination operators are compared in Figure 2.5. The two intermediate operators (local, R-3, and global, R-5) are seen to provide the most efficient recombination.

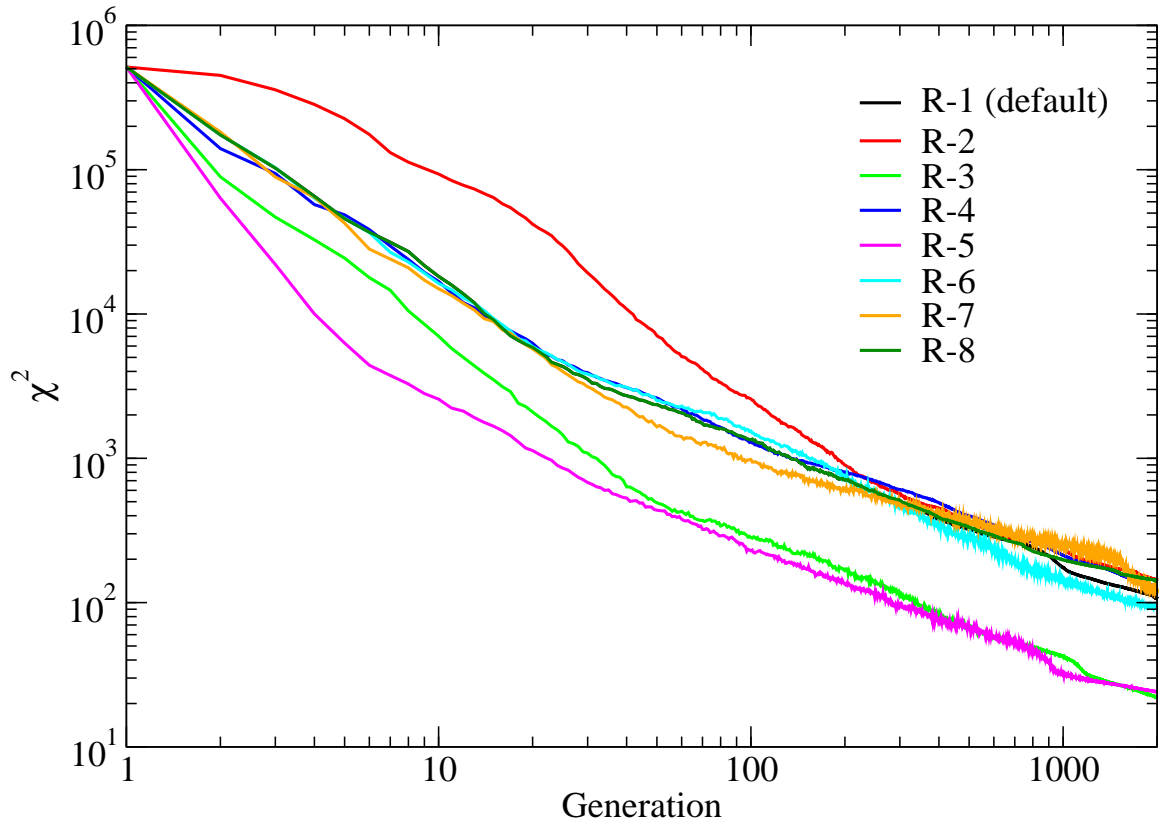


Figure 2.5: Variation of optimization profile with choice of recombination operator. Operators tested include: (R-1) local discrete, (R-2) none, (R-3) local intermediate, (R-4) global discrete, (R-5) global intermediate, (R-6) local discrete for parameters and intermediate for  $\sigma$ , (R-7) global discrete for parameters and intermediate for  $\sigma$ , (R-8) local discrete for the first 250 generations, none for the subsequent 1750.

After approximately 250 generations, using no recombination at all (R-2) gave results equivalent to local discrete recombination (R-1). This was an unexpected result, and suggests that recombination is most effective in the early generations of an optimization. After the first 250 generations, all the optimization profiles have similar slopes, suggesting that after this time the optimization is controlled by mutation instead of recombination. If recombination was still important in the later generations, we would expect the profiles in Figure 2.5 to differ significantly at late times. Intermediate operators (R-3 and R-5) produce better results overall due to their clear superiority during the early generations; these recombination operators eventually located parameter sets with  $\chi^2$  (again, averaged over ten independent runs) only 1/5 that of the typical result of the other operators.

These findings are consistent with the genetic diversity data of Figure 2.3, where a substantial drop-off in genetic diversity is observed after approximately 250 generations. Once a population is sufficiently inbred, it is unlikely that recombination can lead to substantial improvements in fitness, since the parents are already all very similar. This is investigated by performing an optimization using the default ES parameters (as in R-1), but then disabling all recombination after 250 generations. These results (R-8) overlap with those obtained with the default (R-1) until roughly 1000 generations, after which the default improves very slightly over the modified version, as shown in Figure 2.5. This behavior is consistent with the hypothesis that recombination is not a substantial contributor to further improvement in fitness after the drop-off in genetic diversity.

It has been suggested that using a discrete operator for the parameters  $x_i$  and an intermediate operator for the  $\sigma_i$  is more effective than using either fully discrete or fully intermediate operators [3]. Our results show that this is not the case in this application, and that the use of an intermediate operator for the parameters  $x_i$  is the key factor. Fully intermediate operators R-3 and R-5 are clearly much more efficient than operators R-6 and R-7, which apply

discrete recombination to the  $x_i$  and intermediate recombination to the  $\sigma_i$ . The similarity between R-3 and R-5 after the first 50 generations suggests that there is no substantial difference between local and global recombination operators in this application.

### 2.3.4 Mutation Size Control

Mutation operators must be included in ES optimizations because recombination operators alone cannot fully search the available parameter space. For instance, when using intermediate operators, the averaging of parameters would mean that children with  $x_i$  values outside of the largest and smallest  $x_i$  in the current group of parents would never be generated. Likewise, when using discrete recombination operators, the only children that could be created would be combinations of parameters already in the population.

While all mutations involve Gaussian perturbations, the size of these perturbations may be controlled in various ways. It is considered advantageous to have large mutations at the beginning of the optimization, which helps to search quickly across the range of allowed values. However, at later times smaller mutations may be desirable as they can allow near-optimal parents to produce children that are “refinements” of themselves; this is analogous to the very small steps taken by conventional optimization techniques as they approach an extrema. Therefore, the absolute size of mutations should be gradually reduced [38]. The method used for this may also attempt to promote genetic diversity.

The default method used here, labeled M-1, has an independent  $\sigma_i$  for each parameter  $x_i$ . Following Beyer and Schwefel [38], the  $\sigma_i$  are generated through a recombination process (as above), and then mutated via

$$\sigma_i^{child} := \sigma_i^{child} \cdot \mathcal{S}_g \cdot \mathcal{S}_i \quad (2.7)$$



where the two mutation operators  $\mathcal{S}_g$  and  $\mathcal{S}_i$  are:

$$\mathcal{S}_g = \exp(\tau_g \cdot G(0, 1)) \quad \tau_g = \frac{1}{\sqrt{2N}} \quad (2.8)$$

$$\mathcal{S}_i = \exp(\tau_i \cdot G(0, 1)) \quad \tau_i = \frac{1}{\sqrt{2\sqrt{N}}} \quad (2.9)$$

$\mathcal{S}_g$  is calculated independently for each child and used for all the  $\sigma_i$ ; this acts as a global scaling of mutation size, while the  $\mathcal{S}_i$  are calculated independently for each  $i$  for each child, allowing for variations in mutation size between parameters.

The simplest mutation size control operator is to fix  $\sigma$  for the entire length of the optimization. Method M-2 demonstrates such a constant global  $\sigma$ .

Method M-3 is referred to as “simple annealing.” Here, a global  $\sigma$  is reduced by a constant factor every generation:  $\sigma := \sigma \cdot c_\sigma$  where  $0 < c_\sigma < 1$ . For the profile in Figure 2.6,  $c_\sigma = 0.995$ . Note that M-2 may be considered a special case of M-3.

Method M-4 introduces history dependence. It sets  $\sigma$  by scaling  $\sigma_0$  by the square root of the current average value of the parents’ fitness divided by the average value of the parents’ fitness after an initial equilibration period. This equilibration period is determined as the end of the initial rapid decrease in  $\chi^2$ . Specifically, for generation  $g > 100$ , once  $\langle \chi^2 \rangle(g) \geq 0.9 \langle \chi^2 \rangle(g - 100)$ , we set  $\langle \chi^2 \rangle_{ref} = \langle \chi^2 \rangle(g)$  and proceed according to:

$$\sigma = \sigma_0 \times \left( \frac{\langle \chi^2 \rangle_{parents}}{\langle \chi^2 \rangle_{ref}} \right)^{\frac{1}{2}} \quad (2.10)$$

where  $\sigma_0$  is the initial value for  $\sigma$ . This directs the mutation size to decrease at a slower rate than fitness itself for the majority of the simulation, allowing search for a global minimum.

The mutation size decreases rapidly when the fitness is a small fraction of the fitness found at the end of the equilibration period, enhancing local search.

Method M-5 is also history-dependent, and attempts to promote genetic diversity while still allowing only small mutations near the end of a run. To do this, M-5 compares  $\chi_{min}^2$  (the lowest  $\chi^2$  of the current population) with the  $\chi^2$  averaged over the last 100 generations. It uses the following quantities:

$$\chi_{scale}^2 = \left(\frac{10}{g} + 1\right) \cdot \chi_{min}^2(g) \quad (2.11)$$

$$\langle\langle\chi^2\rangle\rangle_{100}(g) = \frac{1}{100} \sum_i^{i-100} \langle\chi^2\rangle(g) \quad (2.12)$$

Every tenth generation, if  $\langle\langle\chi^2\rangle\rangle_{100}(g) > \chi_{scale}^2$  then  $\sigma$  is reduced by a multiplicative factor  $c_\sigma$ , else  $\sigma$  is increased by the inverse of the factor  $c_\sigma$ . In this work  $c_\sigma = 0.95$ . Furthermore, if  $\chi_{min}^2(g) = \chi_{min}^2(g - 100)$  then we assume that the minimum has been approximately located and reduce  $\sigma$  by  $c_\sigma^2$ . Note that this condition can only be satisfied using overlapping or semi-overlapping selection methods.

Lastly, mutation size control method M-6 uses a history-dependent adjustment of  $\sigma$  which is similar in motivation to M-5, but with a different criterion for changing  $\sigma$ . M-6 tracks the average of the last 10 changes in  $\chi_{min}^2$  by defining a quantity  $\langle\Delta\chi_{min}^2\rangle_{10}(g)$ , which is the average over the 10 most recent non-zero changes in  $\chi_{min}^2$ . This measures the “step size” of progress towards an optimum solution. Then, if  $\langle\langle\chi^2\rangle\rangle_{10}(g) > 4 \cdot \langle\Delta\chi_{min}^2\rangle_{10}(g)$ ,  $\sigma$  is reduced by a multiplicative factor  $c_\sigma$ ; else  $\sigma$  is increased by the inverse of  $c_\sigma$ . As in M-5,  $c_\sigma = 0.95$ , and if  $\chi_{min}^2(g - 100) = \chi_{min}^2(g)$  then  $\sigma$  is reduced by a factor  $c_\sigma^2$ .

The performance of these different mutation operators is shown in Figure 2.6. There is no significant impact of mutation size control until roughly 250 generations. It was argued

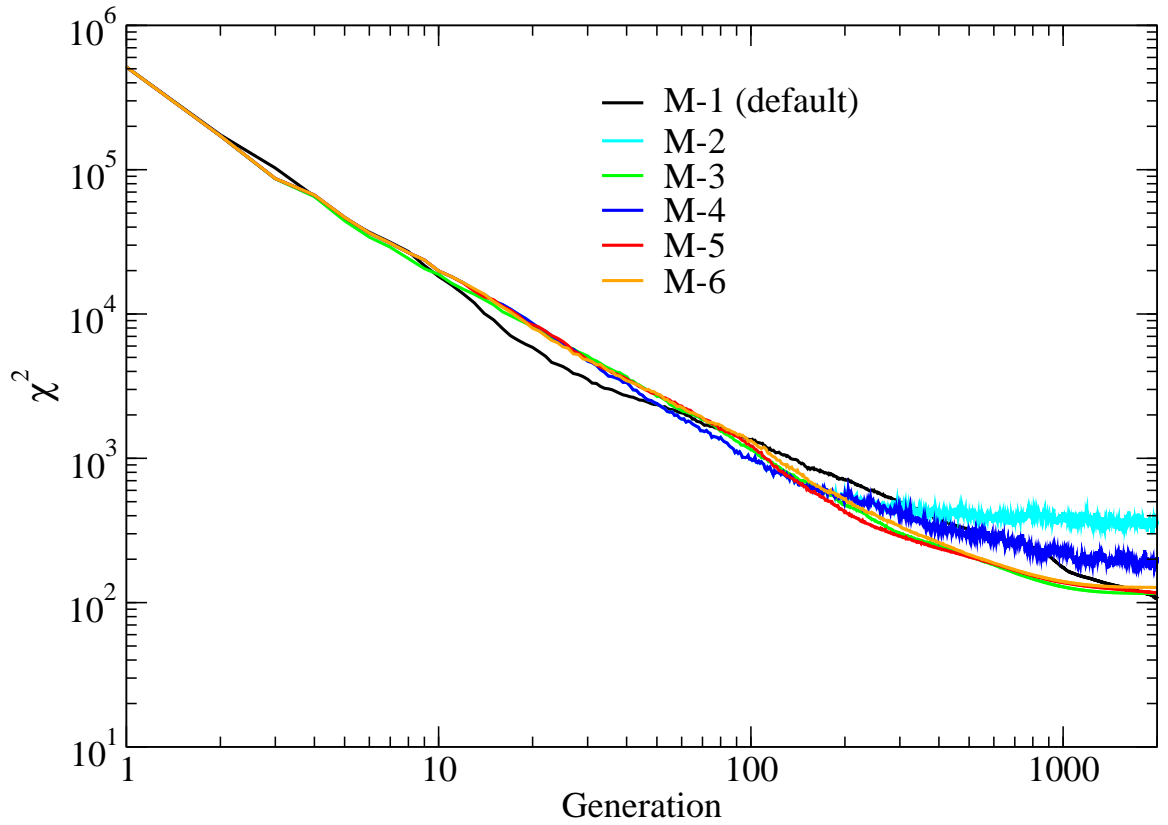


Figure 2.6: Variation of optimization profile with mutation size control algorithm. Algorithms tested include: (M-1) independent  $\{\sigma_i\}$ , (M-2) constant  $\sigma$ , (M-3) annealing  $\sigma$  by a constant factor, (M-4) adjustment of  $\sigma$  relative to early  $\chi^2$ , (M-5) history-dependent, diversity-preserving algorithm, (M-6) alternative history-dependent, diversity-preserving algorithm.

above that recombination methods only had a significant effect in the first 250 generations. It appears that after 250 generations the populations are sufficiently homogeneous that mutation becomes the dominant method of search.

Keeping a constant mutation size prevents parameters from being optimized to values any more precise than the size of Gaussian mutations being applied. This is shown by the fluctuating yet flat fitness of the constant- $\sigma$  method M-2 from generation 300 onward. The flat fitness profile occurs because the default selection method is non-overlapping and the best parent is not carried forward to the next generation. Method M-4 gives results similar to keeping  $\sigma$  constant in the later generations, which is surprising. The scaling factor in M-4 should allow for drops in  $\chi^2$  to produce relatively greater drops in  $\sigma$  when the optimization is in its later generations. However, this is not observed, and  $\sigma$  never became small enough to reach the  $\chi^2$  values achieved in other methods.

History-dependent, diversity-promoting methods M-5 and M-6 produce results similar to simple annealing, algorithm M-3. Methods M-5 and M-6 did have the desired impact on the genetic diversity of the parent population, but the effect only became noticeable after roughly 1300 generations. At that point, the population had already converged on a single minima and the diversity was quite low. The likely explanation for the observed behavior is that the diversity-enhancing mutations tended to be for parameters on which  $\chi^2$  did not depend sensitively, so that the mutations would increase the radius of gyration but not lower the fitness. These mutations, therefore, would not contribute strongly to the location of new, lower- $\chi^2$  minima. For such methods to have a significant effect on the optimization, they would have to be tuned to become active closer to the point when mutation takes over from recombination as the dominant form of search, near 250 generations. The default algorithm M-1 performed well but has a somewhat “wavier” profile than the other variants, possibly caused by sporadic large reductions in  $\chi^2$  in one of the independent runs. This algorithm

ends up very slightly outperforming the other mutation size control algorithms tested. It may be that the large amount of local search towards the end of optimizations does not provide an opportunity for more complex mutation size control mechanisms to outperform the basic M-1 algorithm.

### 2.3.5 Selection

Selection methods are compared in Figure 2.7. The default selection method used, S-1, was the  $(m, n)$  non-overlapping truncation method, S-1 is deterministic, choosing the best  $m$  out of  $n$  children to be the parents for the next generation. This is compared against overlapping (S-2) and semi-overlapping (S-3 and S-4) truncations, and all combinations of overlapping and non-overlapping two-way and eight-way tournament methods (S-5 through S-8). S-1, S-3 and S-4 clearly outperformed all other options in the selection tests. S-1 and S-2 performed similarly until roughly 350 generations into the optimization. S-1 provided a final result with a  $\chi^2$  almost 50% better than S-2. Tournament methods are less elitist than truncation methods, and also less effective. The two-way tournament methods S-5 and S-6, also called binary tournaments, do not approach the  $\chi^2$  value of other methods. Increasing the number of participants in a tournament increases the method's elitism, which makes this method more flexible than truncation methods. However, even eight-way tournament selection methods S-7 and S-8 still lag behind truncation methods.

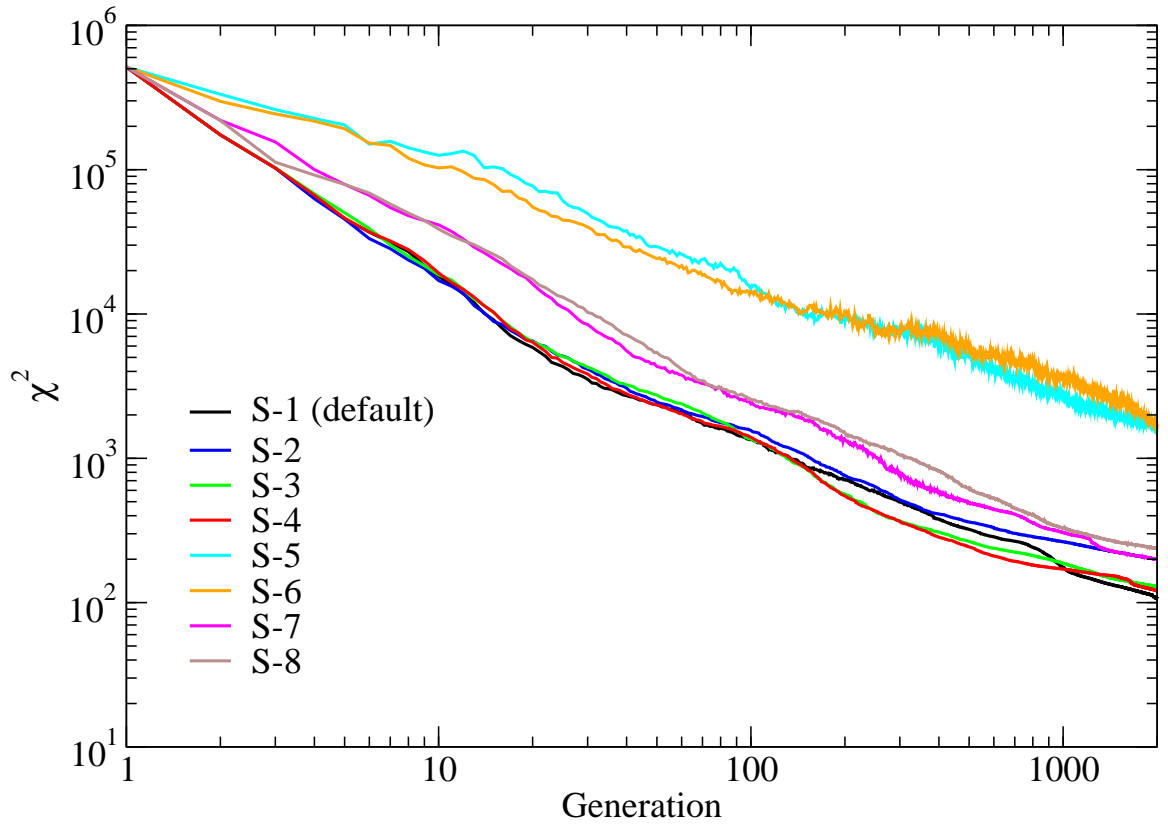


Figure 2.7: Variation of optimization profile with choice of selection operator. Operators tested include: (S-1) non-overlapping truncation, (S-2) overlapping truncation, (S-3) non-overlapping truncation plus best parent, (S-4) non-overlapping truncation plus best-ever individual, (S-5) non-overlapping 2-way tournament, (S-6) overlapping 2-way tournament, (S-7) non-overlapping 8-way tournament, (S-8) overlapping 8-way tournament.

### 2.3.6 Simulated Annealing

For comparison with the evolutionary strategies, we also considered an efficient simulated annealing (SA) algorithm [6]. Simulated annealing is similar to (1+1)-ES, though with different selection and mutation size control operators.

In our SA implementation, a new trial solution (child) is generated by applying Gaussian mutations to parameters of the parent. As this is only done for one child per cycle, we refer to births instead of generations. With probability 0.2 we mutate each parameter  $x_i$  by addition of a Gaussian random number  $G(0, \sigma_i)$ , where  $\sigma_i$  is a global  $\sigma$  scaled by the allowed range of parameter  $i$ , as in most of the ES mutation size control variants. Another change made beyond a typical simulated annealing algorithm is that acceptance and rejection of trial solutions are tracked over the past 512 births. If fewer than 20 percent of children are accepted, then  $\sigma$  is decreased by a factor of  $c_\sigma = 0.995$ . If more than 20 percent are accepted, then  $\sigma$  is increased by a factor of  $1/c_\sigma$ . This is a simple version of the “1/5 rule” sometimes used in (1,1) evolutionary strategies and Monte Carlo simulations [3]. The algorithm has a “temperature”  $T$  (with initial value 175.0585 (kJ/mol)<sup>2</sup>) which is annealed by a factor  $c_T = 0.99994$  after each birth. The child replaces the parent if  $U(0,1) \leq \exp(-(\chi_{child}^2 - \chi_{parent}^2)/T)$  where  $U(0,1)$  is a uniform random number on the interval  $[0,1]$ .

As shown in Figure 2.8 the shape of the convergence profile in simulated annealing is substantially different from that displayed by the evolutionary strategies tested. After an initial rapid improvement, a period of slow searching occurs. The rapid feedback of simulated annealing – only considering one child per generation before choosing a new parent – may explain the advantage of SA in the first thousand births or so. The advantage of SA towards the end of the simulation is probably related to the “1/5 rule” which allows mutation size

to be adjusted on-the-fly. The historical success of this heuristic is in part what inspired attempts to use mutation size control heuristics in evolutionary algorithms. Interestingly, the profile of SA optimizations at very late times is still different in shape than that of any of the ES mutation size control variants, even though they are designed to have similar effects.

As the simulated temperature is lowered, the algorithm becomes trapped in a single minimum. Different annealing runs produce fitness values varying over about one order of magnitude, much as do the independent ES optimizations of Figure 2.2. The cooling schedule used here was chosen to allow the optimization to reach low temperatures, characterized by fluctuations in  $\chi^2$  much smaller than  $\mathcal{O}(1)$ , within the same number of function evaluations that the evolutionary strategies were allowed. There may be less variation between final fitness values when using a slower cooling schedule. Nevertheless, simulated annealing is very effective in finding a good solution.

## 2.4 Parametrization against CPMD reference data

Using combinations of ES options that were found to be effective in the meta-optimization study, we then ran many optimizations of the FG potential against the second training set, composed of DFT data. These calculations fit the FG functional form against data which it cannot perfectly reproduce, and so the minimum possible  $\chi^2$  will no longer be equal to zero. These optimizations were initialized with the original FG potential parameters as one of the parents.



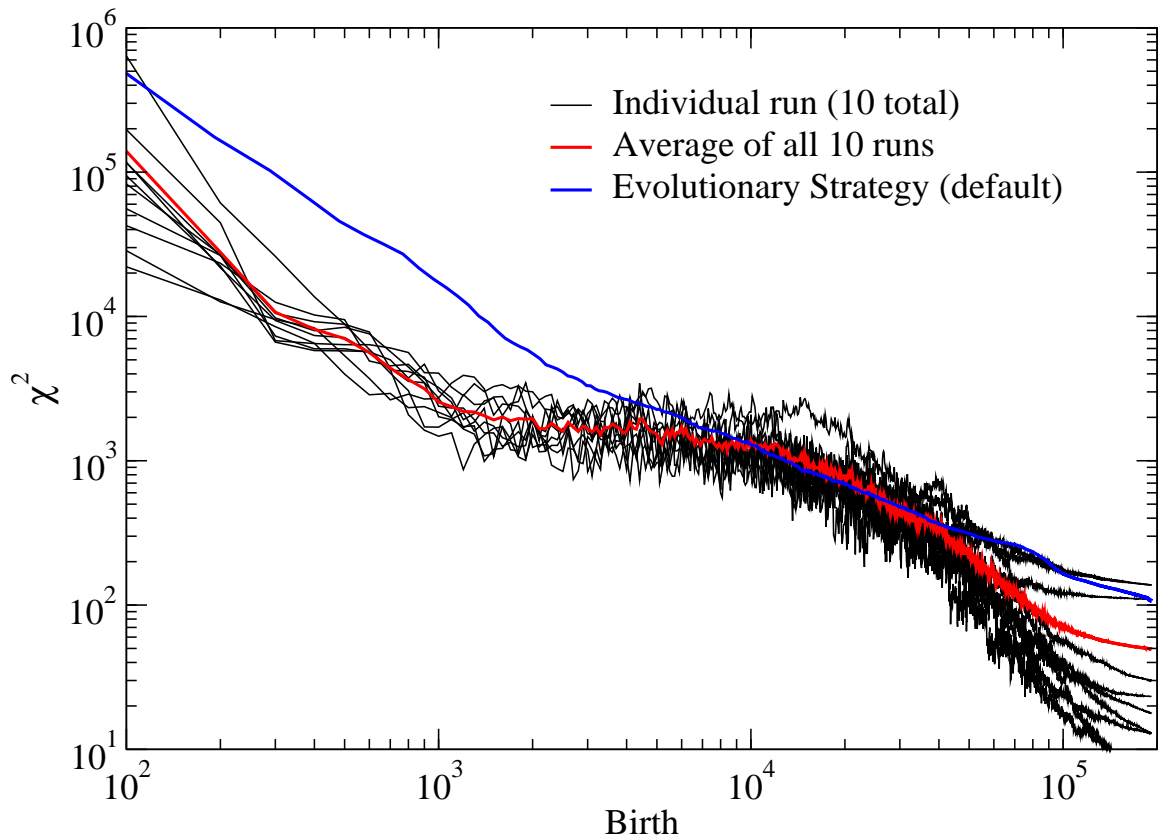


Figure 2.8: Simulated annealing optimizations. As in Figure 2, ten independent runs (starting from the same point) are shown, as well as their average.

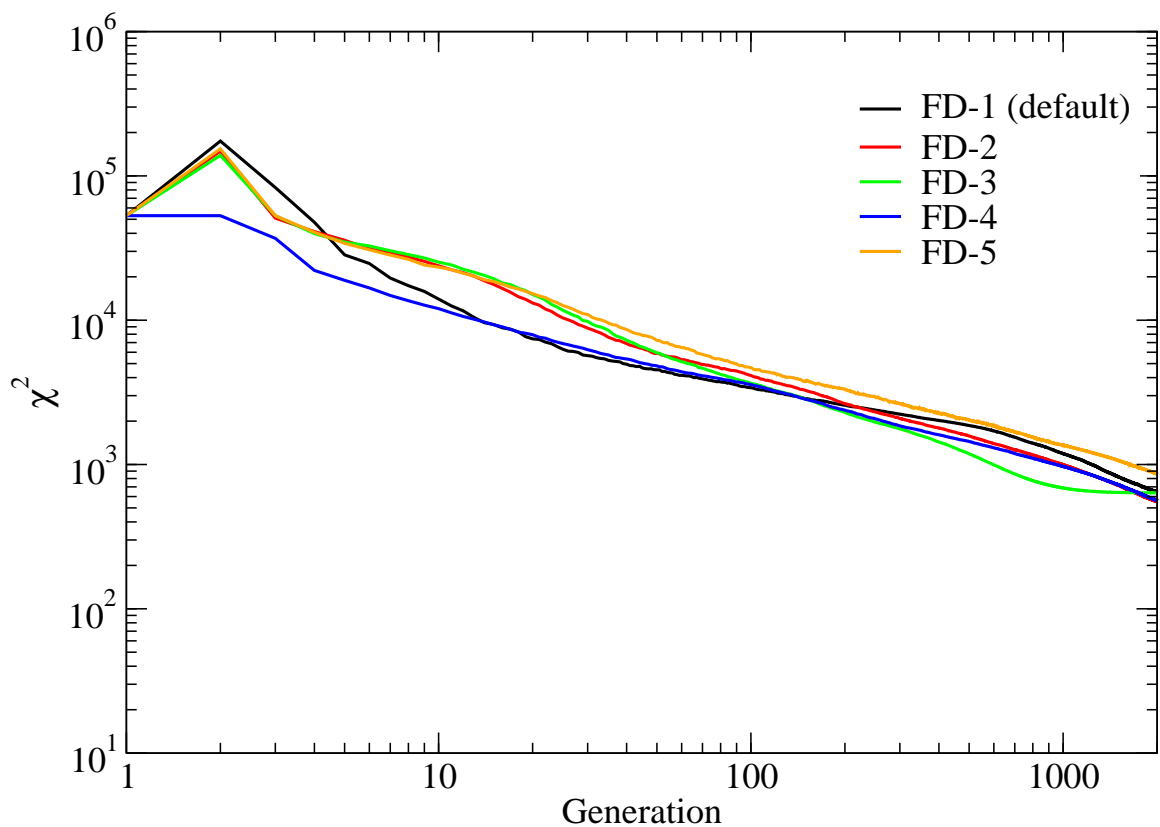


Figure 2.9: Fitting the FG functional form to the CPMD training set. FD-1 is the default method in the meta-optimization tests. FD-2 uses local, intermediate recombination, and other options as in FD-1. FD-3 uses local, intermediate recombination and simple annealing mutation size control, and other options as in FD-1. FD-4 uses local, intermediate recombination and non-overlapping truncation plus best-ever individual selection, and other options as in FD-1. FD-5 uses local, intermediate recombination and non-overlapping 8-way tournament selection, and other options as in FD-1.

These results are shown in Figure 2.9. FD-1 was the default method used in the meta-optimization study. FD-2 used local, intermediate recombination. FD-3 used local, intermediate recombination and simple annealing for mutation size control. FD-4 used local, intermediate recombination and semi-overlapping truncation selection from the population  $m + n$ . FD-5 used local, intermediate recombination and 8-way tournament selection.

The FG parameters are better than almost any random guess. The use of non-overlapping selection then creates a “spike” at the second generation in four of the five methods tested, since recombination and mutation create children with a larger  $\chi^2$  than the FG parameters while the FG potential is not carried over to the second generation.

FD-2 and FD-4 performed the best, and have extremely similar profiles for the last 1000 generations of the optimization. Against this training set, the effects of recombination are observed much further into the optimization than the 250 generations usually seen during the meta-optimization study. The effects of recombination may be observed for a longer number of generations because an exact solution is not available for this case, and because the initial guess may be much further from a good solution. FD-1 and FD-2 develop similar slopes after generation 1000. FD-3, using simple annealing, performs strongly until just after generation 1000, when  $\sigma$  became too small to make further significant improvements in fitness. Lastly, FD-5 lagged consistently behind the other options, showing that for this problem and the population size used, even large tournament sizes may not be sufficiently elitist. Excepting FD-3, all of these methods displayed optimization profiles similar to those seen in the meta-optimization study, suggesting that the approach of fitting an empirical potential to itself is a reasonable choice of test problem for investigation of ES behavior.

The parameter sets obtained from these calculations are shown in Table 1; these are the fittest individual results from the ten independent runs using each evolutionary strategy

Parameter	FD-1	FD-2	FD-3	FD-4	FD-5	FG
$A(\text{H-H}), \times 10^{-9} \text{ ergs}$	0.03103	0.02106	0.03571	0.02257	0.021513	0.0340
$\rho(\text{H-H}), \text{\AA}$	0.2827	0.1784	0.2573	0.1786	0.2206	0.35
$\beta(\text{H-H}), \text{\AA}$	1.319	1.3790	1.3526	1.3496	1.3727	2.10
$a_1(\text{H-H}), \times 10^{-12} \text{ ergs}$	-5.335	-6.3800	-5.3370	-5.7848	-5.3192	-5.2973
$b_1(\text{H-H}), \text{\AA}^{-1}$	5.117	4.7664	4.7996	5.2802	5.4553	6.0
$c_1(\text{H-H}), \text{\AA}$	1.2663	1.2006	1.2770	1.2207	1.2542	1.51
$a_2(\text{H-H}), \times 10^{-12} \text{ ergs}$	0.2009	0.2632	0.4197	0.2993	0.3546	0.3473
$b_2(\text{H-H}), \text{\AA}^{-1}$	1.8539	2.0173	1.3476	2.1513	2.2582	2.0
$c_2(\text{H-H}), \text{\AA}$	3.2085	3.1084	2.5569	3.0789	3.0109	2.42
$A(\text{O-H}), \times 10^{-9} \text{ ergs}$	0.3360	0.3838	0.4018	0.3882	0.3848	0.3984
$\rho(\text{O-H}), \text{\AA}$	0.2992	0.2773	0.2695	0.2757	0.2787	0.29
$\beta(\text{O-H}), \text{\AA}$	1.7270	1.7978	1.7405	1.9038	1.9026	2.26
$a_1(\text{O-H}), \times 10^{-12} \text{ ergs}$	-2.2366	-1.2288	-1.8019	-1.7787	-1.4016	-2.0840
$b_1(\text{O-H}), \text{\AA}^{-1}$	10.2427	21.4197	19.0815	20.9755	17.0696	15.0
$c_1(\text{O-H}), \text{\AA}$	1.1064	1.1605	1.1855	1.1760	1.1541	1.05
$a_2(\text{O-H}), \times 10^{-12} \text{ ergs}$	6.8043	7.1150	7.1936	8.4660	7.8496	7.6412
$b_2(\text{O-H}), \text{\AA}^{-1}$	2.8448	3.2279	3.2265	2.7840	3.0235	3.2
$c_2(\text{O-H}), \text{\AA}$	1.4358	1.6233	1.5092	1.5852	1.5941	1.50
$a_3(\text{O-H}), \times 10^{-12} \text{ ergs}$	-0.8008	-1.1142	-0.8619	-0.8341	-1.0400	-0.8336
$b_3(\text{O-H}), \text{\AA}^{-1}$	3.8372	5.3733	4.9270	5.1868	5.1650	5.0
$c_3(\text{O-H}), \text{\AA}$	1.7244	1.9072	1.8161	1.9928	1.8755	2.00
$A(\text{O-O}), \times 10^{-9} \text{ ergs}$	0.6204	0.9318	0.7086	1.0126	0.6314	0.7250
$\rho(\text{O-O}), \text{\AA}$	0.1536	0.2258	0.2316	0.1685	0.1815	0.29
$\beta(\text{O-O}), \text{\AA}$	1.6597	1.7056	1.7057	1.7451	1.7893	2.34
$A(\text{Si-H}), \times 10^{-9} \text{ ergs}$	0.03488	0.04092	0.05571	0.05767	0.05520	0.0690
$\rho(\text{Si-H}), \text{\AA}$	0.3333	0.1732	0.2241	0.1868	0.2076	0.29
$\beta(\text{Si-H}), \text{\AA}$	1.7574	1.8393	1.8692	1.8520	1.9144	2.31
$a_1(\text{Si-H}), \times 10^{-12} \text{ ergs}$	-5.9716	-5.9754	-6.2415	-6.0339	-6.3399	-4.6542
$b_1(\text{Si-H}), \text{\AA}^{-1}$	3.6173	3.7601	3.7488	3.7710	3.7888	6.0
$c_1(\text{Si-H}), \text{\AA}$	2.1270	2.1799	2.2019	2.1767	2.1761	2.20
$A(\text{Si-O}), \times 10^{-9} \text{ ergs}$	4.3049	2.0904	2.3021	2.1387	2.3477	2.9620
$\rho(\text{Si-O}), \text{\AA}$	0.2320	0.3052	0.3041	0.3058	0.3070	0.29
$\beta(\text{Si-O}), \text{\AA}$	1.2277	1.5972	1.6715	1.6305	1.7657	2.34
$A(\text{Si-Si}), \times 10^{-9} \text{ ergs}$	2.0641	2.0021	2.2312	1.7762	2.1179	1.8770
$\rho(\text{Si-Si}), \text{\AA}$	0.3035	0.1890	0.2862	0.2197	0.1855	0.29
$\beta(\text{Si-Si}), \text{\AA}$	1.1892	1.4321	1.4610	1.4137	1.5670	2.29
$\lambda(\text{O-Si-O}), \times 10^{-11} \text{ ergs}$	11.3068	10.1754	19.44	9.6978	19.1985	19.0
$\gamma(\text{O-Si-O}), \text{\AA}$	4.1957	3.8445	3.1944	4.1697	3.9531	2.8
$\lambda(\text{Si-O-Si}), \times 10^{-11} \text{ ergs}$	0.4496	0.4483	0.3136	0.4447	0.4439	0.3
$\gamma(\text{Si-O-Si}), \text{\AA}$	1.0005	1.0052	2.0065	1.0021	1.0067	2.0
$\lambda(\text{Si-O-H}), \times 10^{-11} \text{ ergs}$	4.8690	3.1015	5.1819	2.7365	3.9802	5.0
$\gamma(\text{Si-O-H: Si-O}), \text{\AA}$	1.6022	1.0161	1.9427	1.0495	1.7518	2.0
$\gamma(\text{Si-O-H: O-H}), \text{\AA}$	1.5203	1.7038	1.3923	1.7058	1.5326	1.2
$\lambda(\text{H-O-H}), \times 10^{-11} \text{ ergs}$	31.9566	25.3210	32.1643	38.3666	32.3834	35.0
$\gamma(\text{H-O-H}), \text{\AA}$	1.4741	1.3718	1.4345	1.4649	1.4264	1.3
$\chi^2, (\text{kJ/mol})^2$	352.4	430.7	501.3	459.8	560.7	52963.0

Table 2.1: Feuston-Garofalini re-parametrizations by evolutionary strategies. The fittest parameter sets from Figure 9 are shown, as well as the original FG parametrization. Parameter names and units are as given in [61]. Only “fitted” parameters are given in the table; other parameters (cutoffs, reference angles, and formal charges) are kept fixed at their literature values [61].

variant. All five parametrizations are dramatically fitter (closer to the CPMD reference data) than the original FG parameters, though we should note that this does not *a priori* indicate that they will be more suitable for modeling a particular system or property. The obtained  $\chi^2$  values of  $\sim 500 \text{ (kJ/mol)}^2$  correspond to an rms deviation of 0.1 kJ/mol per atom in the energy of any given configuration relative to the reference configuration. The average hydrogen bond strength in liquid water is about 20 kJ/mol. Since hydrogen bonding is expected to dominate the energy differences between configurations, we expect that these important interactions should be described well by these parameter sets, at least to within the accuracy of the density functional theory used. The different sets vary considerably in the actual values of particular parameters, with some, such as the  $\lambda$ s, varying over a fairly large range, while others, such as  $\beta(\text{O-O})$ , are very similar from one set to the next. In a few cases ( $\gamma(\text{Si-O-Si})$ , for example) parameters have converged to one side of their “allowed range,” which suggests that better fits could be obtained by expanding these ranges. Additionally, training set coverage could be extended to include more configurations which contain geometries at extreme bond angles or distances. As the training set was generated using a CPMD simulation, physically infrequent configurations were not necessarily sampled.

## 2.5 Discussion

All of the optimization profiles shown above are averaged over ten independent runs. In a typical run, for instance as shown in Figure 2.3, the radius of gyration  $R_g$  of the population at the endpoint had a value near to 0.03, indicating that the members of the population were all very similar to each other and that the algorithm had converged into a single minimum of the fitness function. However, the  $R_g$  value measured for the ten best solutions

obtained from the ten independent runs is 1.49, approximately two orders of magnitude larger. Comparing the two values suggests that independent optimization runs are finding different minima of the fitness function; inspection of the actual parameter sets given in Table 1 (which is a different calculation, but with similar convergence properties) supports this. While evolutionary methods are often touted as globally convergent, it appears that for “reasonable” run conditions, performing multiple independent runs is probably a good strategy. In practice, for a sufficiently complex problem any method which is globally convergent in infinite time will only be locally optimal in finite time. The stochastic nature of the method leads to different locally optimal solutions being found through independently seeded runs. However, global methods are still quite valuable as their solutions will usually be better than those found by purely local optimizations.

The number of minima, and the “shape” of the fitness function  $\chi^2$ , are of interest in this regard. Given the high dimensionality of the parameter space, one might suppose that the many different solutions found in these optimizations arise from the relatively small number (128) of configurations used in the training set: the fewer conditions there are to satisfy, the more ways there should be to do so. However, this appears to not be the case. The  $R_g$  values for the ten independent optimal solutions for each of the different training set sizes of Figure 1 are all between 1.33 and 1.68, with no correlation with training set size. That is, adding additional data beyond 128 configuration energies does not bring the many locally-optimal parameter sets any closer to each other. Likewise, the corresponding  $R_g$  values for the runs of Figure 4, which vary in  $m$  and  $n$ , are all between 1.49 and 1.73, and likewise do not exhibit any trend with population parameters. It therefore appears that the many local minima in this objective function result from the potential itself and the particular definition of  $\chi^2$  used, rather than the size of the training set or other, more arbitrary parameters.

A significant feature observed in many of the optimization profiles in this study was an apparent crossover, at about 250 generations, from behavior dominated by recombination to behavior dominated by mutation. This crossover was remarkably robust to changes in the various operators involved and therefore its appearance may be anticipated in related problems. Manipulating the number of generations in which recombination is the dominant mode of search may be an important tactic for future evolutionary algorithm work, as it is believed that recombination is almost entirely global, not local, search.

Since most of the computational effort is expended after the crossover, in order to more quickly locate optimized parameter sets one should make the mutation operator as efficient as possible. However, of the considerable number of mutation operators tested in this work there were no clearly superior ones, and significant further improvements may be difficult. One possible alternative could be a composite (or “memetic” [75]) optimization strategy, in which, once the ES algorithm “slows down”, one switches over to a different, locally-convergent, method which is good at “refining” an approximately-located solution. The radius of gyration  $R_g$  introduced above is an effective signature for the ES crossover and could be monitored to trigger the change to another method. We note, in this regard, that rapidly-converging methods such as conjugate-gradient optimization or Newton-Raphson root-finding are not very well suited to parameter optimization problems, since it is preferable to not have to implement derivatives of the energy with respect to the potential parameters. However, such derivatives could be efficiently estimated by using parallelized one-way finite or centered difference methods, which could provide a cost-effective route to the precise location of  $\chi^2$  minima; the effectiveness of this approach would depend on the roughness of the  $\chi^2$  function and the stability of the optimizer with respect to numerical precision. It should be noted that when applied to ligand docking, a prior study did not find local optimization to be beneficial [55].

Based on the results of the meta-optimization study, we recommend the use of intermediate recombination operators for both the parameters  $\{x_i\}$  and mutation size control variables  $\{\sigma_i\}$ . No substantial difference is observed between global intermediate and local intermediate recombination at long times, though at short times the global variant appears preferable. Of the mutation operators considered, the self-adaptive, independent- $\sigma$  method M-1 is at least as effective as any of the others considered and lacks any “adjustable” parameters. We note that “simple annealing” is nearly as effective with one adjustable parameter (here chosen arbitrarily) and considerably simpler to implement. Finally, non-overlapping or semi-overlapping truncation methods are clearly preferred for selection, as the tournament methods appeared to not have enough selection pressure, and overlapping methods exhibited slowdowns in the later stages of optimization.

Simultaneous parametrization of all parts of a potential has the advantage of providing more uniform “quality” between different terms, but greatly increases the complexity of the numerical problem to be solved. Even in fully automated parametrizations one must still provide initial estimates of the magnitude (and, likely, the allowed range) of each parameter, which requires at least some physical insight into the problem. In applications where an existing potential is to be extended, such estimates are straightforward, but for the parametrization of a new functional form or previously unstudied chemical species they may be more difficult to obtain. For very large problems, preliminary parametrization of groups of related parameters against subsets of the available reference data may also be a viable strategy.

ES methods are inherently parallelizable. While evolution of the objective (fitness) function used here can also be parallelized over a reasonable number of processors, the ES approach has a considerable advantage in this regard, and therefore should be of particular interest when wall-clock time is a limiting factor. This suggests that ES is particularly suitable for



work involving a large number of parametrizations, for instance comparisons of different functional forms, comparisons of potentials based on different reference data, or even the (common) extension of an existing potential to treat some new chemical species.

This type of design is implemented in a “data parallel” program. Each CPU is performing the same type of work, but on different data sets. The advantage of ES methods over simulated annealing methods is the multiple level structure of its data parallelism, which is useful on cluster computers with many independent nodes. Rapid communication is needed when calculating the fitness of a specific individual parameter set, which is confined to a single node. The evaluation of the entire set of individuals may be distributed over many nodes, and communication between nodes will be less frequent than communication between CPUs on the same node. This is important because the latency on inter-node communication is orders of magnitude higher than intra-node communication. In other fields, parallel programs are often “task parallel” in which one CPU will perform work of one type (such as graphical rendering) and another CPU perform an entirely different task (such as sound processing). This type of parallelism is rare for optimization applications. When increasing the size of the training set or the number of individuals being evaluated as part of an ES, this optimization method provides a good example of Gustafon’s law for parallel computing, where the possible speedup from additional processors is essentially unbounded.

$$S = f(n) + p \times (1 - f(n)) \quad (2.13)$$

In this equation, the speedup is  $S$ ,  $f(n)$  is the fraction (ranging from zero to one) of work that must be done sequentially, and  $p$  is the number of processors. As the parallelizable part of the work increases (training set size and number of individuals, represented as “ $n$ ”),  $f(n)$  decreases, and therefore speedup increases as more processors are used. For a fixed

problem size, Amdahl’s law applies, with high scaling.

$$S = 1(1 - F) + Fp \quad (2.14)$$

In this case,  $S$  is the speedup,  $F$  is the fraction of work that is parallelizable (and is a fixed value), and  $p$  is once again the number of processors that may be used.

As shown in Figure 2.8, the efficient simulated annealing method used in this study generally outperformed the evolutionary strategies when fitting the FG potential to the FG training set. Simulated annealing can be parallelized either through distribution of configurations in the training set or by performing multiple independent runs. As discussed earlier, evolutionary strategies may spread the evaluation of groups of children across available processors. This is a significant advantage: the number of CPU cores available in modern supercomputers or clusters is increasing at a greater rate than the performance per core. We also note that the adaptive mutation algorithm in the simulated annealing optimizations may have been superior to the mutation algorithms used in the evolutionary strategy, as no equivalent to the “1/5 rule” was available for ES runs.

Finally, we note that the type of reference data used (configurational energies) and definition of the fitness function as a least-squares–like criterion are themselves arbitrary choices and there are certainly other possibilities. Force (gradient) data could also be used in the fitness function (as in the “force-matching” studies described above [24, 25]), for instance, and a “minimax” criteria could be used to define the fitness function, so that the final optimized value would limit the maximum deviation in selected quantities between the model system and the reference data.

In this chapter, we have presented guidelines for the selection of ES operators and training set sizes suitable for the parametrization of empirical potentials against reference data generated using electronic-structure methods. Such parametrizations are considerably higher in dimension and complexity than the typical problems used in development of evolutionary strategies, and algorithms optimized for these different problem classes differ in non-obvious ways. The ES approach is highly parallelizable and may therefore be suited to “large” optimization problems. However, ES exhibits relatively slow convergence at later generations that may warrant changeover at late times to an alternate method which converges rapidly once a solution has been approximately located.

## Chapter 3

# Towards an Improved Charge-Transfer Potential for Silica

### 3.1 Introduction

Our research group has a long-standing interest in simulating properties and formation of silica sol-gels [76–78]. This has included development of coarse-grained models of gel networks and atomistic simulation using existing models and extremely large simulation cells to directly simulate the early stages of gelation [2, 79]. As part of this effort, we sought to create a better atom-based potential for silica.

Incorporating changes in charge distribution among atoms in molecules during chemical reactions is a challenge for empirical potentials [33]. As discussed in the previous chapter, most commonly used potentials use fixed partial charges on atomic sites, possibly augmented with dipoles or higher multipoles centered near atomic sites or geometric centers of small molecules. These empirical potentials are often unable to undergo bond-breaking and bond-forming reactions. The Feuston and Garofalini (FG) potential does undergo bond-breaking and bond-forming reactions, but its electrostatics are relatively primitive,

consisting only of hard-core electronic repulsion and a damped Coulomb interaction [1]. Further, full formal charges are used (+1 for hydrogen,  $-2$  for oxygen, +4 for silicon), which may be appropriate for ionized, isolated atoms but which do not accurately describe the electrostatic field around a molecule.

There has been significant work on empirical models which allow atom charges to change over the course of a simulation. One widely cited model incorporates a charge equilibration technique (the “ReaxFF” model, which uses the “QEq” technique developed by the same group) [18, 19]. This approach has been successful in modeling some molecular reactions. However, we judged that it is too costly to use for systems consisting of millions of atoms, due to the complex algorithms used to calculate new charges at each timestep. In particular, the QEq algorithm formally has  $O(N^2)$  scaling ( $N$  is the number of atoms in the system), which would be prohibitively expensive at large system sizes. The Kieffer group has also created a charge-transfer model for silica species which is under active development [80, 81], but will not be considered in detail here.

Alavi, Alvarez, Elliot and McDonald developed a charge-transfer model (henceforth, the “AAEM-CT” model) which is inexpensive, using only the local environment of atoms to determine charges and charge-transfer forces at each timestep [8]. As this model had already been applied to liquid silica, we decided to combine the charge-transfer features of the AAEM-CT model and some of the empirical features of the FG model to create a new charge-transfer model of silica which could eventually be extended to aqueous silicate species. The AAEM-CT energies and charge-transfer forces are given in Equations 3.1 through 3.5. They include a Coulombic interaction ( $E_C$ ) and empirical covalent terms ( $E_{emp}$ ) of a generalized Morse (also known as a Hulbert-Hirschfelder) form, plus a steric repulsion between oxygen atoms. Note that only atoms of opposite sign and within a cutoff

distance ( $R_{ij} < R_{CT}$ ) are allowed to transfer charge (for all other atoms normal Coulomb interactions still apply).

$$E_C = \sum_i \sum_{j>i} \frac{q_i q_j}{4\pi\epsilon_0 R_{ij}} \quad (3.1)$$

$$q_i^A = q^A - \Delta q \sum_j f(\mathbf{r}_i^A, \mathbf{r}_j^B) \quad (3.2)$$

$$q_j^B = q^B + \Delta q \sum_i f(\mathbf{r}_i^A, \mathbf{r}_j^B) \quad (3.3)$$

$$f(R_{ij}) = \frac{1}{2} \{1 - \tanh[(R_{ij} - R_{AB})/\zeta]\} \quad (3.4)$$

$$\begin{aligned} E_{emp} = & \epsilon[(1 - \exp(-x))^2 + cx^3(1 + bx)\exp(-2x) - 1] \\ & + \frac{e^2}{36\pi\epsilon_0\sigma} \left(\frac{\sigma}{R_{ij}}\right)^9 \end{aligned} \quad (3.5)$$

In these equations,  $q_i^A$  is the charge on an individual cation ( $A$ ), and  $q_i^B$  would be the charge on an anion ( $B$ ), and  $x = (R_{ij} - R_e)/a$  in Equation 3.5. The amount of charge which may be transferred between them is determined by the parameter  $\Delta q$  which is specific to a given  $A - B$  pair, and the charge transfer functional  $f$  which depends on the distance between atoms  $i$  and  $j$  and their specific types (its shape is shown in Figure 3.1).

We planned to parametrize our new model, the Barnes-Gelb modification of the AAEM-CT model (the “BG-AAEM-CT” model) using an evolutionary strategy (ES), with ES techniques optimized in the previous chapter. The model would be fit against *ab initio* training sets. Simulations of different phases of silica would be used to validate the empirical potential form and parameters. In this chapter we describe those efforts, problems encountered

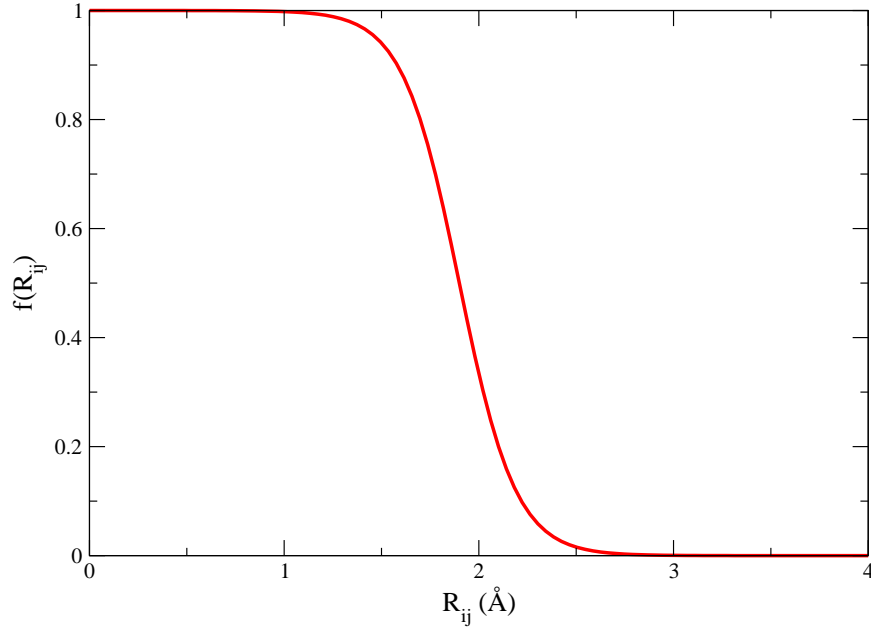


Figure 3.1: The charge-transfer function ( $f(R_{ij})$ ) for the AAEM-CT model shown in graphical form. At small separation, the full amount  $\delta q$  is transferred, while the amount transferred goes smoothly to zero outside a certain range.

and overcome, and some simulation results obtained using a preliminary version of the new model.

## 3.2 Potential Development

While working with the AAEM-CT model, we noticed problems with simulations at constant pressure. Specifically, the simulation cells would tend to expand rapidly and soon after that the numerical integrator would become unstable. At first, this was quite puzzling. No mention of such problems had been mentioned in the literature; prior work was mostly performed in the canonical and microcanonical ensembles. First, we verified our program's implementation of the analytical equations for force and pressure calculations. This was

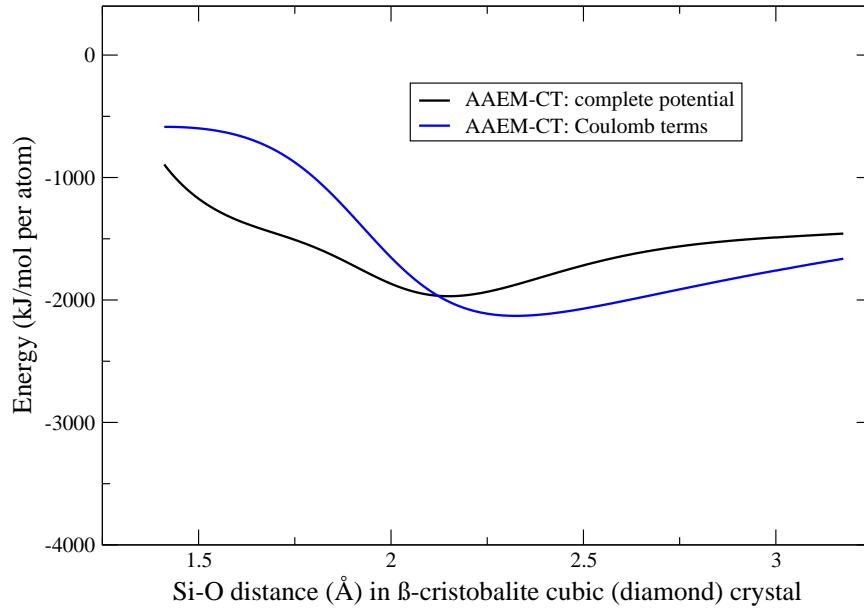


Figure 3.2: AAEM-CT model energies for a  $\beta$ -cristobalite cell. In this crystal, the silicon atoms occupy lattice sites of a diamond structure, with oxygen atoms bridging between them. The lattice constant on the y axis is that of the Si-O bond distance.

done through comparison with numerical differentiation of the energy with respect to particle displacement (for forces) and simulation cell size changes (for pressure). We eventually discovered the root cause of the problem by examining the  $\beta$ -cristobalite crystal phase of AAEM-CT silica.

In Figure 3.2 we show the AAEM-CT potential energy versus silicon-oxygen distance for a uniformly expanded  $\beta$ -cristobalite crystal. The minimum energy lattice constant is near 2.35 Å instead of the experimental 1.61 Å. This occurs because the total energy of the system is minimized at silicon-oxygen distances *outside* charge-transfer range, due to the increased magnitude of attractive Coulomb interactions. That is, the charge-transfer between neighboring atoms lowers the magnitude of (opposite) neighboring charges, and therefore the total cohesive energy of the crystal. As a result, atoms prefer not to be bonded when the system is allowed to expand freely. At 4000 K and 1 bar, the equilibrium density of



AAEM-CT silica is only 0.24 g/cc, roughly 1/10 of experimental density. A correction for this rather fundamental problem had to be part of our improvement plan.

### 3.2.1 Functional Form

Our proposed functional form is most easily understood by examining the Coulombic and non-Coulombic parts separately. We will discuss the Coulombic part of the potential first, as it is the most complicated. We include a short-ranged, many-body modification to the AAEM-CT form when atoms are transferring charge. As with the AAEM-CT model, for two atoms  $i$  and  $j$  to transfer charge, they must be within range ( $R_{ij} < R_{CT}$ ) and of types  $A$  and  $B$  which form bonds with each other. The following equations then apply:

$$q_i^A = q^A - \Delta q \sum_j f(\mathbf{r}_i^A, \mathbf{r}_j^B) \quad (3.6)$$

$$q_j^B = q^B + \Delta q \sum_i f(\mathbf{r}_i^A, \mathbf{r}_j^B) \quad (3.7)$$

$$f(R_{ij}) = \frac{1}{2} \{1 - \tanh[(R_{ij} - R_{AB})/\zeta]\} \quad (3.8)$$

$$E_{CT}(\mathbf{r}_i^A, \mathbf{r}_j^B) = \frac{1}{R_{ij}} [q_i^A + \Delta q \cdot f(R_{ij})][q_j^B - \Delta q \cdot f(R_{ij})] \quad (3.9)$$

$$E_C(\mathbf{r}_i^A, \mathbf{r}_j^B) = \left( P_I + (1 - P_I) \frac{R_{ij}}{R_{CT}} \right) E_{CT}(i, j) + (1 - P_I) \left( 1 - \frac{R_{ij}}{R_{CT}} \right) \frac{q^A q^B}{R_{ij}} \quad (3.10)$$

During the normal evaluation of the Coulomb sum for the system, Equation 3.10 is used to evaluate the pair energy for two atoms transferring charge. This would be identical to the handling of the Coulomb sum in the AAEM-CT model except for the terms in green and red. The changes in Equation 3.9 modify the short-range energy terms so that some energy from charge transferred between a pair of atoms is “given back” in the energy evaluation

of that pair. The motivation behind this change was to mimic the conversion of energy from an ionic interaction into a covalent bond. The changes in Equation 3.10 include an interpolation parameter ( $P_I$ , with a range of 0 to 1) between charge-transfer Coulomb and formal-charge Coulomb energies, which restores additional short-ranged bonding energy. The second term (the “bare” Coulomb interaction) is larger in magnitude at short distances than the first term, which uses  $E_{CT}$  (the charge-transfer Coulombic energy). A value of  $P_I = 1$  indicates that the interpolation is turned off (“pure  $E_{CT}$ ”), and  $P_I = 0$  indicates the interpolation is fully active. This interpolation may sometimes be useful for adjusting bond lengths during parametrization, as its value may complement the shape and magnitude of the hard repulsive wall in a potential. The constant  $R_{CT}$  is the cutoff distance for charge-transfer and used in the interpolation scheme. Importantly, long-range Coulomb interactions are unaffected by our changes. This allows the evaluation of short-range many-body charge transfer and the resulting forces to remain inexpensive.

The forces that result from charge transfer are complicated. First, it is important to note that the change in charge on an atom with respect to the change in coordinates of a nearby atom is a derivative through the charge transfer function  $f(R_{ij})$ , which is given in Equation 3.11. This expression is used in the Coulombic force on atom  $k$ ,  $F_k$ , which is given in both an expanded and a simplified form (Equations 3.12 and 3.13). The factor  $s_{ij}$  is a “sign” factor and always equal to plus or minus one. It is positive if the atom of type  $i$  is a cation, and negative if the atom of type  $i$  is an anion. The usage of this sign factor allows for a more compact expression of the forces and computationally less expensive implementation in a simulation program as some of the work is moved outside the inner loop.

$$\frac{\partial q_i^{CT}}{\partial r_k} = \frac{\Delta q}{2\zeta} \text{sech}^2[R_{ik} - R_{AB}] / \zeta \cdot \mathbf{r}_{ik} \quad (3.11)$$

$$\begin{aligned}
F_k &= \frac{-\partial E_{CT}}{\partial \mathbf{r}_k} \\
&= \left[ \frac{1}{2} \sum_i \sum_{j \neq i} \frac{\Delta q}{R_{CT}} f(R_{ij}) \cdot \frac{\partial q_i^{CT}}{\partial r_k} - \frac{\Delta q}{R_{CT}} f(R_{ij}) \cdot \frac{\partial q_j^{CT}}{\partial r_k} \right]
\end{aligned} \tag{3.12}$$

$$F_k = \frac{\Delta q}{R_{CT}} \left[ \sum_i \frac{\partial q_i^{CT}}{\partial r_k} \left( \sum_{j \neq i} s_{ij} f(R_{ij}) \right) \right] \tag{3.13}$$

The augmented functional form also has non-Coulombic terms which may be divided into two-body and three-body interactions:

$$E_{2b}(\mathbf{r}_{ij}) = A_{ij} \exp(-\rho_{ij} R_{ij}) - \frac{\beta_{ij}}{R_{ij}^6} \left( \frac{1}{2} + \frac{1}{2} \tanh((R_{ij} - d_{1(ij)})/d_{2(ij)}) \right) \tag{3.14}$$

$$E_{3b}(\mathbf{r}_{ij}, \mathbf{r}_{jk}, \theta_{jik}) = \lambda_{jik} \exp \left[ \frac{\gamma_{ij}}{R_{ij} - R_{ij}^o} + \frac{\gamma_{ik}}{R_{ik} - R_{ik}^o} \right] \times (\cos \theta_{jik} - \cos \theta_{jik}^o)^2 \tag{3.15}$$

The two-body form includes an exponential repulsion and an attractive dispersion interaction, which is damped to zero at short distances to preserve a hard repulsive core. The three-body term is of the Stillinger-Weber form (as previously used in the FG model), which acts as a penalty function for deviation from a preferred angle for specified types of triplets. All of the constants represented by symbols in Equations 3.14 and 3.15 are “fittable” parameters (only  $R_{ij}$ ,  $R_{ik}$  and  $\cos \theta_{jik}$  are variables).

### 3.2.2 Training Sets and Parametrization

Our approach to parametrization was based upon that described in Chapter 2: least-squares optimization against *ab initio* “training set” data. Two systems were used to create the training set. The first was a box of fluid  $\text{SiO}_2$  containing 192 atoms at a density of 2.20 g/cc. The second was an  $\alpha$ -quartz box containing 576 atoms at a density of 2.64 g/cc. The procedure used to create the configurations and evaluate their energies was as follows. First, molecular dynamics simulation using the Beest-Kramer-Santen (BKS) silica potential [82] to equilibrate the system, at 600 K for the  $\alpha$ -quartz and at 4000 K for the fluid phase. This was done using a Gaussian isokinetic thermostat. One hundred configurations from the equilibration runs (widely separated in simulation time) were then selected. Each of those configurations was then used as the input geometry for a separate plane-wave DFT single-point energy calculation using the CPMD package [72]. These DFT calculations used a 30 Rydberg cutoff, a Vanderbilt ultrasoft pseudopotential [69] for oxygen, a Troullier-Martins pseudopotential [83] for silicon, and the Perdew-Burke-Ernzerhof (PBE96) exchange-correlation functional [68]. Therefore, the training set contained one hundred configurations, representative of systems with different phases, temperatures, and densities. We believed that the range of energies and atomic distances represented would provide enough data to parametrize a transferable empirical potential effectively.

Initial attempts to optimize the BG-AAEM-CT parameter set using evolutionary strategies were almost totally unrestricted, allowing all parameters to vary within physically possible plausible ranges (for example, repulsive wall pre-factors were constrained only to be non-negative). When tested in short simulations of amorphous silica, for models obtained this way often resulted in physically unrealistic behavior, often forming small, dense clusters with hexa-coordinated silicon atoms. To address this, some parameters were often held fixed during optimization. These include the amount of charge transferred (to replicate

BKS charges, which are known to be effective in atomistic models), the interpolation parameter, and three-body terms. Other terms, such as the charge-transfer curvature  $\zeta$ , were set to values near best-fit ES optimization results. A wide variety of parameter sets were tested in preliminary simulations; one such table of values is given in Table 3.1. In this parameter set, isolated atoms have fully ionic charges, like the FG model, but can transfer charge so that at full coordination they would have the same partial charges as the BKS model. The two-body parameters are similar to those of the BKS model, but with repulsive walls which are larger in magnitude. The three-body parameters have the same value as those in the FG model.

### 3.3 Preliminary Simulations using the BG-AAEM-CT Model

In this section, we describe results obtained using the BG-AAEM-CT model with the parameters in Table 3.1. This includes both analytical calculations of lattice energies and molecular dynamics simulations. Our isobaric-isothermal ensemble simulations were performed at temperatures from 3000 to 10000 K and a pressure of 1 bar, for both  $\beta$ -cristobalite and amorphous phases.

#### 3.3.1 Lattice Constant Investigation

BG-AAEM-CT silica has more realistic constant pressure properties than the original AAEM-CT model. The minimum-energy lattice constant is near the experimental 1.61 Å. This is shown in Figure 3.3, which displays energy versus  $\beta$ -cristobalite lattice constant for both the BG-AAEM-CT model and the previously examined AAEM-CT model. In our model, the energy change with respect to system size is much smoother, and the minimum is at the

$q^A$ (proportion of formal charge)	1.0
$q^B$	1.0
$\Delta q(\text{Si-O})$	0.4
$R_{AB}(\text{Si-O}), \text{\AA}$	1.75
$\zeta, \text{\AA}^{-1}$	0.2
$A(\text{Si-O}), \times 10^{-9} \text{ ergs}$	21604.50864
$\rho(\text{Si-O}), \text{\AA}$	4.87318
$\beta(\text{Si-O}), \text{\AA}$	133.5381
$d_1(\text{Si-O}), \text{\AA}$	1.25
$d_2(\text{Si-O}), \text{\AA}^{-1}$	0.2
$A(\text{O-O}), \times 10^{-9} \text{ ergs}$	1666.5276
$\rho(\text{O-O}), \text{\AA}$	2.76
$\beta(\text{O-O}), \text{\AA}$	175.0
$d_1(\text{O-O}), \text{\AA}$	1.25
$d_2(\text{O-O}), \text{\AA}^{-1}$	0.2
$A(\text{Si-Si}), \times 10^{-9} \text{ ergs}$	36000.0
$\rho(\text{Si-Si}), \text{\AA}$	3.0
$\beta(\text{Si-Si}), \text{\AA}$	200.0
$d_1(\text{Si-Si}), \text{\AA}$	2.0
$d_2(\text{Si-Si}), \text{\AA}^{-1}$	0.2
$\lambda(\text{O-Si-O}), \times 10^{-11} \text{ ergs}$	19.0
$\gamma(\text{O-Si-O}), \text{\AA}$	2.8
$R^o(\text{O-Si-O})$	3.0
$\theta(\text{O-Si-O}), \text{degrees}$	109.471
$\lambda(\text{Si-O-Si}), \times 10^{-11} \text{ ergs}$	0.3
$\gamma(\text{Si-O-Si}), \text{\AA}$	2.0
$R^o(\text{Si-O-Si})$	2.6
$\theta(\text{Si-O-Si}), \text{degrees}$	109.471
$P_I$	0.0

Table 3.1: Parameter set for the BG-AAEM-CT model. This is one of many parameter sets tested. For many of the parameters not related to charge-transfer, values used are similar to those in the BKS or FG models.

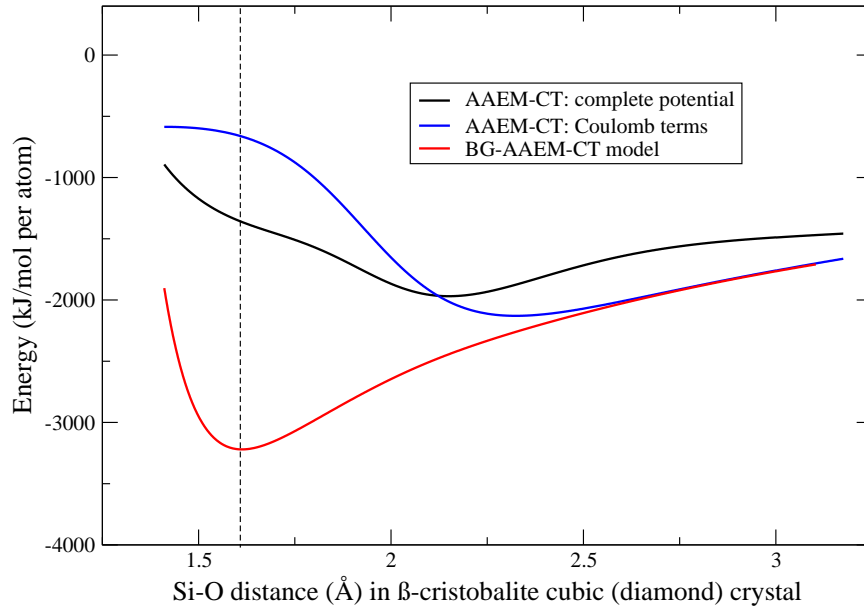


Figure 3.3:  $\beta$ -cristobalite energy versus lattice constant for BG-AAEM-CT and AAEM-CT models. The dashed line indicates the experimental value, which is near the minimum for the BG-AAEM-CT curve in this Figure.

right position. The BG-AAEM-CT repulsive wall also has a steeper slope, and resembles that of more well-behaved potentials such as the BKS model.

### 3.3.2 Structure and Charge Distribution

Oxygen-oxygen and silicon-oxygen radial distribution functions (RDF) for these models are given in Figure 3.4. The  $\beta$ -cristobalite simulation was performed at 3000 K and 1 bar. The amorphous phase results are from a simulation started with an amorphous initial configuration and run at 5000 K and 1 bar. They show that the  $\beta$ -cristobalite crystal remains intact, with the crystalline structure signified by sharp peaks. The silicon-oxygen and oxygen-oxygen RDFs for the amorphous phase of the BG-AAEM-CT model are quite

similar to that of the BKS model simulated under the same conditions, with the nearest-neighbor and next-nearest-neighbor peaks occurring at roughly the same distances.

The structural differences between the crystalline and amorphous phase are also reflected in charge distributions from simulations using the BG-AAEM-CT model, which are given in Figure 3.5. In each figure, the broader distribution of charges in the higher temperature amorphous phase reflects the wider distribution of interatomic distances. In the amorphous phase atoms are sometimes not fully coordinated, as they occasionally experience rearrangements in their local environment.

### 3.3.3 Melting

A short investigation into the melting point of this model was also conducted. The original problem with the AAEM-CT model was that the crystal was unstable, but the BG-AAEM-CT model as parametrized here appears to overcorrect for this problem and tended not to melt at any physically realistic temperatures in our simulations.

For example, Figure 3.6 contains density results from a series of isobaric-isothermal simulations for the BG-AAEM-CT and BKS models. Each simulation was performed independently, in parallel: the beginning of one simulation was not dependent on the result of the prior state point in the series. For the BKS amorphous phase data, the simulations were seeded using an amorphous system previously equilibrated at 4000 K. The initial configuration for the crystal simulations was a perfect crystal. The data shown are density versus temperature; when a phase transition occurs, the density of the cell undergoes a significant change. At 4000 K and above, the BKS crystal melts, and simulations seeded from the crystal phase have the same density as those seeded from the amorphous phase. For BG-AAEM-CT  $\beta$ -cristobalite silica, the equilibrium density at 4000 K and 1 bar is near



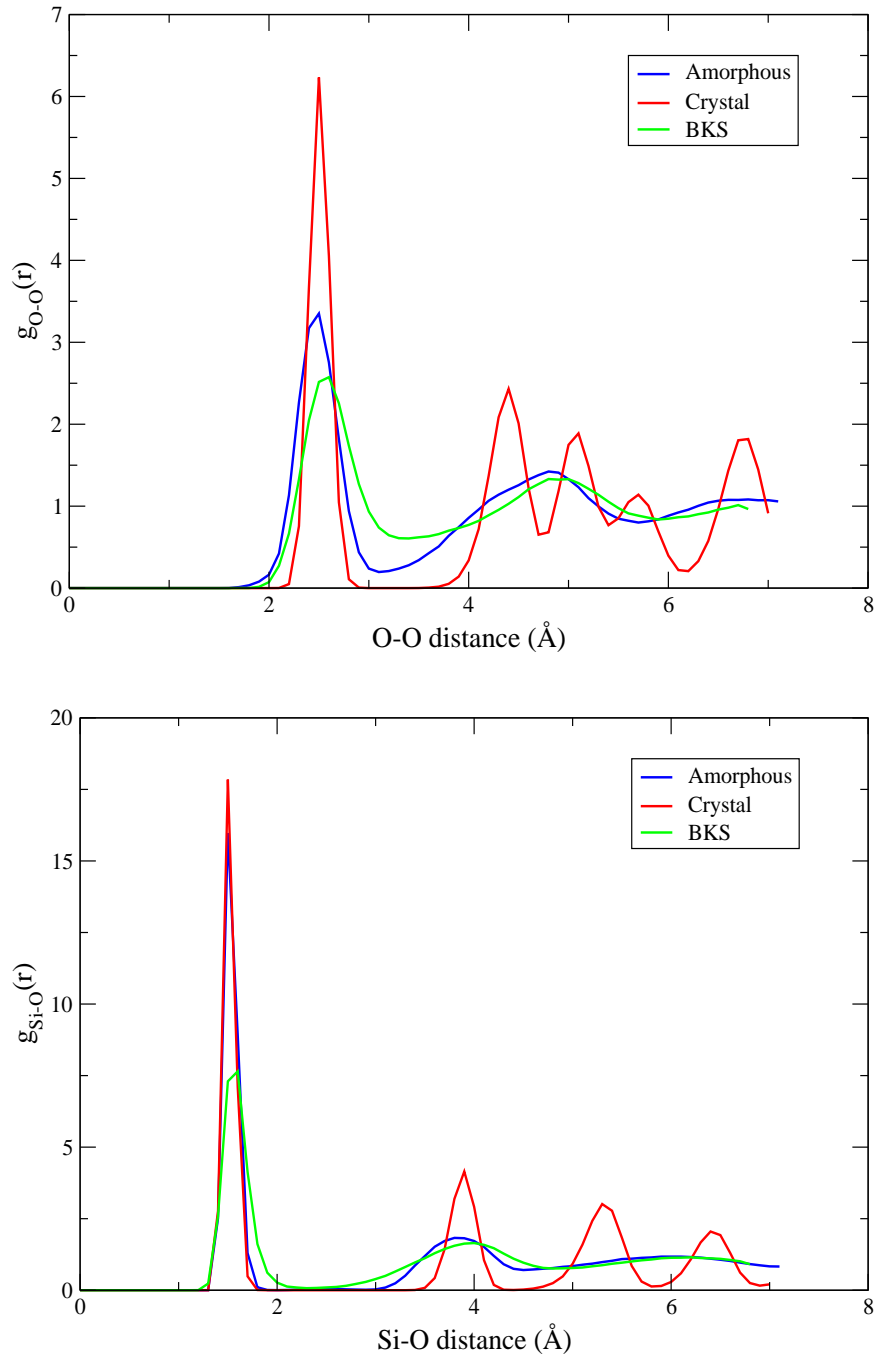


Figure 3.4: Oxygen-oxygen and silicon-oxygen radial distributions functions for BG-AAEM-CT and BKS models. Crystals simulated at 3000 K, 1 bar and the amorphous phase at 5000 K, 1 bar, with a duration of 1 ns.

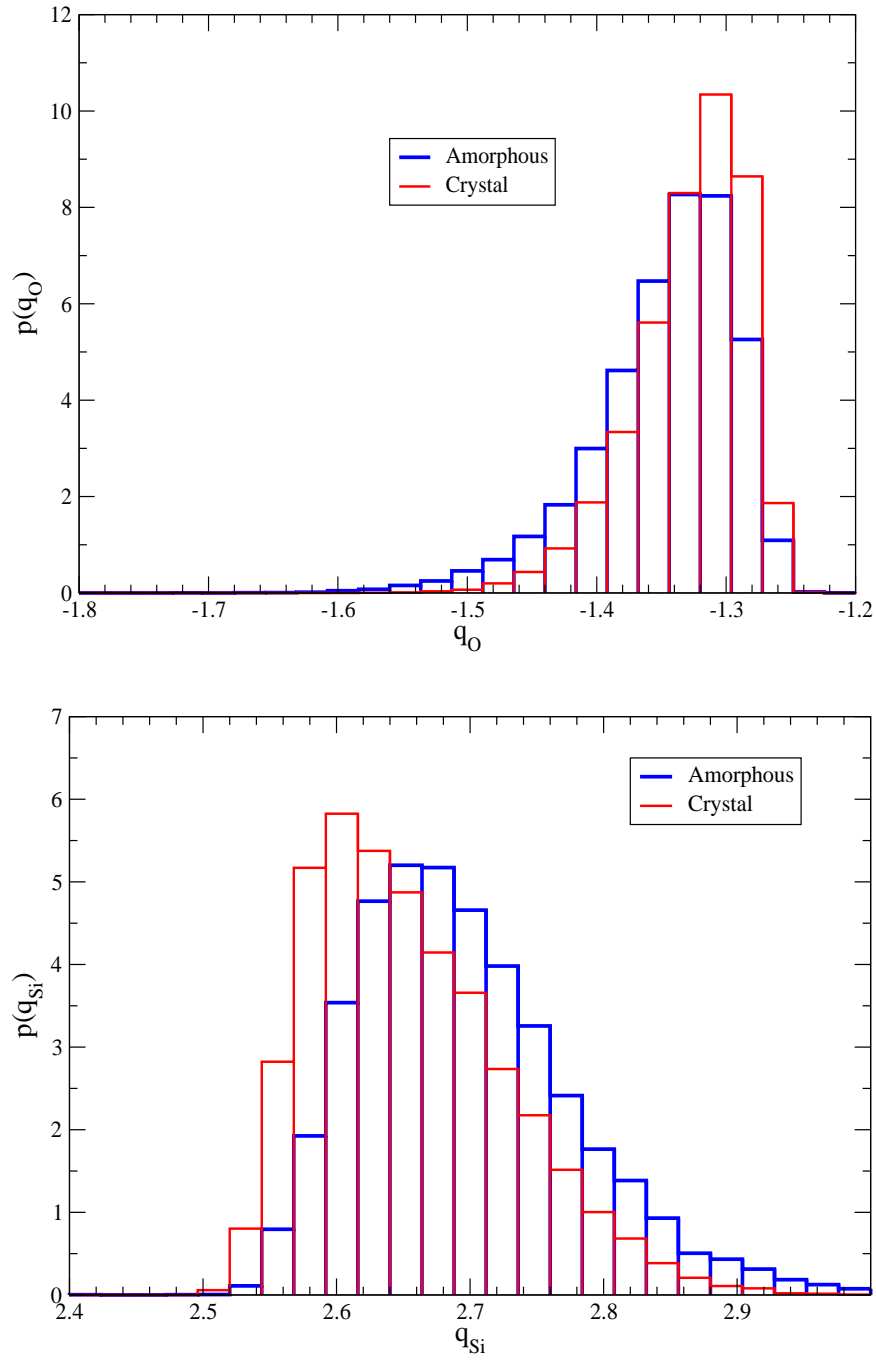


Figure 3.5: Oxygen and silicon charge distributions for amorphous and crystal phases of the BG-AAEM-CT model. Systems simulated at 3000 K, 1 bar for crystals and 5000 K, 1 bar for the amorphous phase, with a duration of 1 ns.

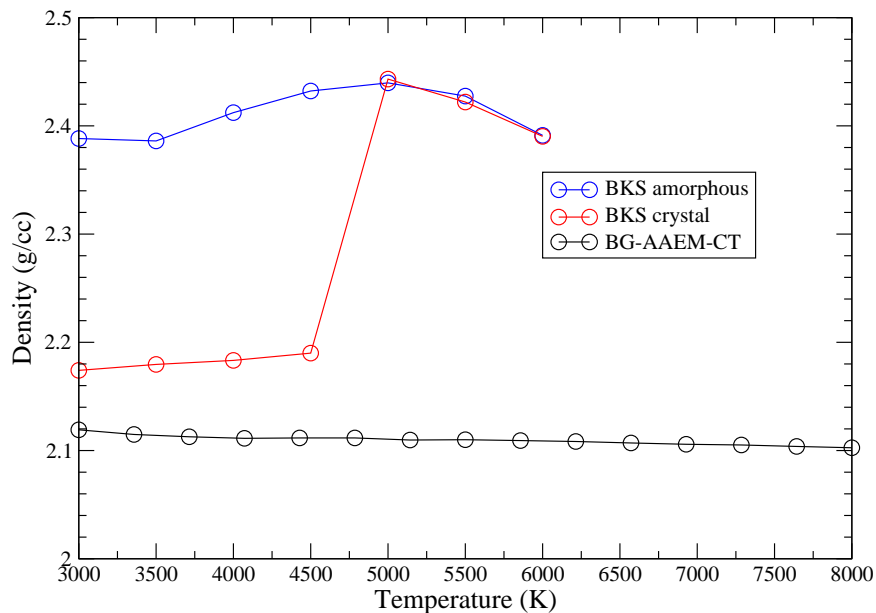


Figure 3.6: Density versus temperature from isobaric-isothermal simulations of the BG-AAEM-CT and BKS models. The amorphous phase is more dense than  $\beta$ -cristobalite, hence the BKS model density rises upon melting of the crystal. All simulations performed at 1 bar, with a duration of 1 ns.

2.12 g/cc. However, the BG-AAEM-CT model does not have a sharp density change in the range of temperatures shown, and inspection of snapshots verifies that the crystal is still intact, even at the highest temperatures.

### 3.4 Discussion

Developing a new charge-transfer model proved to be a challenging endeavor. Our original aspiration was to include terms for hydrogen-oxygen and hydrogen-silicon interactions, and we chose a functional form similar to the BKS or FG potential, which had previously been augmented with three-body potential terms. After encountering multiple difficulties in getting a good “fit” with evolutionary strategy optimizations, our close investigation

of the AAEM-CT model discovered the flaw in how its charge-transfer form behaved in constant pressure simulations. We focused first on silica and solving the problem of low density at normal pressure, but ultimately could not obtain a well-behaved charge-transfer silica model. The sources of problems in our new model could lie in many different places. The AAEM-CT charge-transfer form could be flawed beyond repair, with our attempts to “fix” it simply revealing new problems after solving an old one. Our choice of charge-transfer parameters may not have been appropriate for both amorphous and crystalline phases. Ultimately, while some progress was made in improving the AAEM-CT form and we obtained a new model which was usable in constant pressure simulations, we decided not to extend the model further for simulation of aqueous silica systems.

## **Chapter 4**

# **Structure, Thermodynamics, and Solubility in Tetromino Fluids**

### **4.1 Introduction**

The reversible self-assembly of objects of controlled size and shape is of great interest for construction of nanoscale devices and nanostructured materials without laborious manipulation of individual particles. Self-assembly-based methods have been proposed, and in many cases demonstrated, for applications in areas from data storage [84] to medicine [85] to energy generation [86]. Self-assembly occurs both at the molecular scale, most famously in self-assembled monolayers [87,88], and in nanoparticulate systems, polymers, and combinations of the two [89,90]. Apart from its potential applications, self-assembly is also fascinating in its own right, with complex structures formed through an interplay of energetic and entropic forces. Studies of self-assembly relate naturally to work on the appearance and stabilization of structure in other systems, ranging from ordered crystals through partially-ordered liquid crystals to disordered liquids.

Much insight into the structure and behavior of self-assembled systems, liquid crystals and normal liquids has come from theoretical and simulation studies of idealized models. The simplest models are “hard”, or “athermal”, in that particles do not interact except to completely avoid overlap, behaving like idealized billiard balls. In such systems the behavior is entropically controlled: the structure adopted by a system of rigid hard objects is that which maximizes the total entropy, a sum of translational and rotational contributions. Fluids of rigid hard objects studied to date have included disks [91], spheres [92,93], confined spheres [94], hard dumbbells in two [95] and three [96] dimensions, squares [97] rectangles [98–101], pentagons [102], rods, spherocylinders and ellipsoids [103–105], cubes [106], and others.

Lattice models, in which objects are positioned only at discrete sites, are appealing because of their simplicity, analytical tractability, and low computational cost. Hard sphere lattice systems have been studied with both analytical and numerical methods for more than 40 years [107, 108]. Hard hexagons on a lattice were solved analytically by Baxter [109]. Freed and co-workers have studied the behavior of a variety of lattice objects, with and without energetic interactions, in the context of their Lattice Cluster Theory (LCT) [110–112]. Columnar phase transitions were also investigated as part of their LCT, which we will revisit in studies on larger polyominoes. Panagiotopoulos *et al.* have obtained the phase behavior of a variety of on-lattice shapes in three dimensions, both with nearest-neighbor attractive interactions and in the athermal limit. First-order crystallization transitions were recovered for on-lattice spheres and capped cylinders, while other rigid hard objects were found to display continuous order-disorder transitions [113].

Dill *et al.* have used both analytical methods [114] and simulation [115] to study solvation in fluids of hard lattice objects. Exact expressions for the partition functions of very small numbers of objects in a bounded domain were obtained using recursive methods. From

these were obtained the equations of state (density versus chemical potential) of objects of several shapes, which were then analyzed in terms of Flory-Huggins theory and virial-like expansions [114]. In the subsequent study [115], attractive interactions were added to the model and large-scale Monte Carlo simulations in the canonical ensemble used to extract relations between the chemical potential of the fluid and its contact free energy per unit area, the latter being unambiguously definable in a lattice model. Analysis of fluid structure or the phase diagram of the model was not attempted.

Connected shapes on a two-dimensional lattice, as simulated above, are referred to in the mathematical literature as “polyominoes”, and have been of interest for a considerable time [11]. They have received attention in the popular press, as the foundation for series of puzzles in *Scientific American* [9]. Shapes which occupy one square are monominoes, those which occupy two are dominoes, etc. The mathematics of polyominoes has focused on two questions, the first being enumeration of the possible polyominoes occupying a given number of squares, and the second being the number of ways of arranging polyominoes in a bounded region, generalizing the question originally proposed as the number of possible placements of dominoes on a chessboard, also known as the “dimer model” [116, 117]. Other properties of lattice animals which are commonly investigated include more complex tiling theorems, percolation thresholds and perimeter distributions [118].

Here we consider self-assembly, liquid structure, and solvation in the multicomponent “tetromino” fluid using Monte Carlo simulations. There are seven different one-sided tetrominoes, corresponding to the shapes from the well-known computer game Tetris<sup>TM</sup> [119]. While some of the tetrominoes (and various other polyominoes) have been simulated in the studies mentioned above [98, 114, 115], no comprehensive survey of the statistical mechanics or self-assembly of these objects seems to have been made to date. We note that related models have also been used in studies of compaction in granular matter [120, 121], and

that the problem of arranging “falling polyominoes,” familiar from the computer game, is of practical interest as it is related to algorithms for the optimal packing of crates in trucks [122]. Another packing problem more specific to tetrominoes that has been studied recently was the critical behavior of rigid rods on two-dimensional lattices, in which cumulants were used to quantify nematic transitions [123]. Finally, Cicoira and Rosei have drawn an analogy between the arrangement of pieces in Tetris and the self-assembly of molecules on surfaces [124], and a version of tetrominoes augmented with energetic interactions has been studied in the context of self-organization by Troisi *et al.* [125].

We performed these simulations in the grand canonical ensemble, corresponding to an open system. Since the model is two-dimensional, this is similar in spirit to experimental work on adsorption [124] and self-assembled monolayers [87, 88]. In such studies a surface is placed in contact with a solution or gas, from which particles (the solute, in the former case, and molecules of the gas, in the latter) reversibly adsorb to the surface. The surface layer is therefore in mass equilibrium with a reservoir of additional material; the concentration of the solution (or pressure, in the case of a gas) determines the coverage or density at the surface. Adsorption of molecules on surfaces also offers interesting possibilities for introducing and controlling chirality not present in three-dimensional systems [126, 127].

The details of the model and simulations are discussed in section 4.2, followed by discussion of the structure of pure fluids (section 4.3.1), binary mixtures (section 4.3.2) and multicomponent mixtures (section 4.3.3). The interactions between different shapes are analyzed in terms of virial coefficients in section 4.3.4, followed by further analysis of solubility thermodynamics in both pure and multicomponent fluids in section 4.3.5, and a general discussion of these findings in section 4.4.



The one-component fluids all exhibit marked self-ordering tendencies at higher densities, with quite complex structures formed in some cases. Significant clustering of objects with the same rotational state (orientation) is also observed in some of the pure fluids. In all the binary mixtures, the two species are fully miscible at large scales, but exhibit strong species-specific clustering (segregation) at small scales. This behavior persists in multicomponent mixtures; even in seven-component mixtures of all the shapes there is significant association between objects of the same shape. In order to better understand these phenomena, we calculate the second virial coefficients of the tetrominoes and related quantities, extract thermodynamic volume of mixing data from the simulations of binary mixtures, and determine Henry’s Law solubilities for each shape in a variety of fluids. The overall picture obtained is one in which complementarity of both the shapes of individual objects and of the characteristic structures of different fluids are important in determining the overall behavior of a fluid of given composition, with sometimes counter-intuitive results. Finally, we note that no sharp phase transitions are observed, but that this appears to be due to the small size of the objects considered. It is likely that complex phase behavior may be found in systems of larger polyominoes.

## 4.2 Methodology

### 4.2.1 The Model

The objects (“pieces”) simulated are the seven possible “tetrominoes,” orthogonally connected objects which occupy four lattice sites. These shapes and their common names are given in Figure 4.1. The pieces only interact through avoidance of overlap; there is no attractive potential. There are two enantiomeric pairs: the *S* and *Z* shapes, and the *J* and

*L* shapes. These shapes are not chiral in three dimensions, but restriction to two dimensions eliminates some symmetry operations such that they are no longer superimposable. This is the complete set of “one-sided” tetrominoes, as opposed to the complete set of five “free” tetrominoes which would exclude one of the enantiomers from each pair [11]. One could also consider simulations of larger polyomino sets, such as the eighteen one-sided pentominoes or sixty one-sided hexominoes.

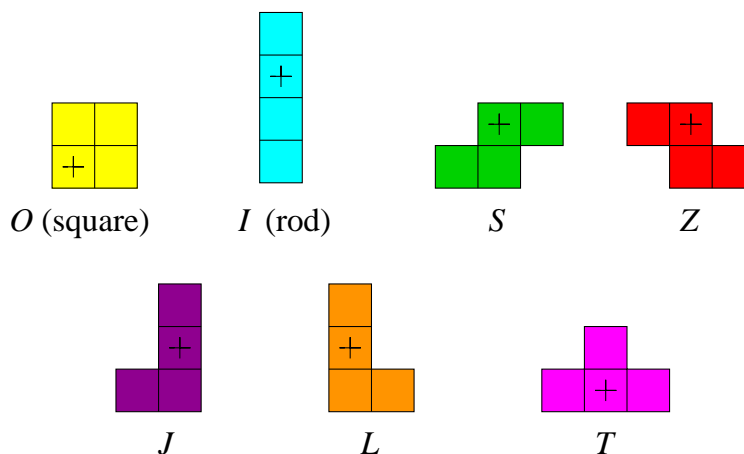


Figure 4.1: The seven one-sided tetrominoes, with corresponding names and symbols, and rotation centers/anchor points marked by “+” symbols. Orientations are labelled numerically, starting at 1. Squares have one orientation, rod, *S* and *Z* shapes have two, and *J*, *L* and *T* shapes have four. The shapes shown above are all in orientation 1; subsequent orientations correspond to 90° or 180° clockwise rotations around the marked points.

Further specifications are required for purposes of statistical mechanics. Only distinguishable rotations will be considered as available “states” for each piece, by analogy with the symmetry of molecules. Therefore, a square (*O*) has one rotational state, the rod (*I*), *S* and *Z* pieces two states, and the *J*, *L* and *T* pieces four states. As shown in Figure 4.1, each

shape is given an “anchor point”, which will be used in the Monte Carlo simulations to define rotational and piece-insertion moves.

### 4.2.2 Simulation details

In the grand canonical ensemble, the number of pieces of a given shape is not fixed but is controlled by an applied chemical potential. Simulations may include any number or combination of the seven shapes. Typically, grand canonical simulations of an  $N$ -component system sample an ensemble at constant temperature, volume and the  $N$  chemical potentials  $\{\mu_i\}$ , or equivalently,  $\beta$ ,  $V$  and the  $N$   $\{\beta\mu_i\}$ , with  $\beta = 1/kT$ . Since this is an athermal model the temperature is an arbitrary parameter with no effect on the distribution of states, and so the thermodynamic variables are reduced to the volume and the  $N$   $\{\beta\mu_i\}$ ; we shall refer to these latter quantities as chemical potentials. At  $\beta\mu = 0$  for a system of ideal gas particles, the equilibrium state would have unit density. This may be considered a reference state, and observed deviations at  $\beta\mu = 0$  are the direct result of the size, shape, and non-overlap requirement of the pieces in a simulation.

The classical grand partition function for a one-component system with discrete states is:

$$\Xi(V, T, \mu) = \sum_i^{states} e^{-\beta\epsilon_i} e^{\beta\mu N_i} \quad (4.1)$$

$$\beta PV = \ln \Xi \quad (4.2)$$

After excluding states with infinite energy (where pieces overlap), only states with zero energy remain, and Equation 4.1 reduces to:

$$\Xi = \sum_i e^{\beta \mu N_i} \quad (4.3)$$

Which may be expressed using a sum over the number of particles in a configuration, instead of a sum over states:

$$\Xi = \sum_N W(N) e^{\beta \mu N} \quad (4.4)$$

Where the  $W(N)$  are degeneracy coefficients (microcanonical density-of-states). Derivatives of this equation may be taken in order to recover thermodynamic quantities:

$$\left( \frac{\partial \ln \Xi}{\partial \beta \mu} \right)_{V, \beta} = \sum_N W(N) N e^{\beta \mu N} / \Xi = \langle N \rangle \quad (4.5)$$

Integrating:

$$\Delta \ln \Xi \Big|_{\beta \mu_1}^{\beta \mu_2} = \int_{\beta \mu_1}^{\beta \mu_2} \langle N \rangle (\beta \mu) d\beta \mu \quad (4.6)$$

This result is related to  $\beta PV$  through Equation 4.2, and is useful for calculating thermodynamic quantities.

Our simulations include the following trial moves: insertions, deletions, translations, rotations, identity changes, and piece switches. With the exception of insertions, deletions and identity changes, all of these are normal (that is, unbiased) Monte Carlo moves, such that the Boltzmann weight-based acceptance/rejection criteria are simply that moves which introduce an overlap are always rejected, and moves which do not are always accepted. For insertion and deletion moves, we use a bias to improve sampling at high densities, similar

to cavity bias insertion [128]. In this approach, a list of empty lattice sites is stored, and insertion attempts place a trial piece’s anchor point on one of those empty sites. The bias algorithm works by selecting a lattice site known to be empty for the anchor point’s insertion attempt. This means that the acceptance criteria for insertion and deletion must be altered in order to maintain detailed balance. This bias greatly increases efficiency at high densities by avoidance of trivially-rejected insertion moves, while maintaining microscopic reversibility. The probability of accepting a piece insertion is then  $\exp(\beta\mu_i) \times P_{free}/(N_i + 1)$ , and the probability of accepting a deletion is  $N_i/(\exp(\beta\mu_i) \times (P_{free} + 4))$ , where  $N_i$  is the number of pieces of type  $i$  and  $P_{free}$  refers to the number of currently empty lattice points.

The other trial moves are straightforward. Translations consist of displacements of an entire piece by one lattice site, in one of the four Cartesian directions. Rotational moves consist of attempts to rotate a piece to a different distinguishable state, chosen randomly and uniformly from the other available states for the piece. Clearly, the location of the anchor point may affect the probability of a rotation attempt being accepted in dense configurations. The anchor points shown in Figure 4.1 were chosen near to the center of each piece in order to provide more compact rotations that will likely result in fewer overlaps. The choice of anchor point only affects the efficiency in simulating a given state point, not the equilibrium results. Identity change moves attempt to both change the shape of a piece and its orientation. A piece of shape  $i$  is chosen at random and changed to a uniformly randomly selected different shape  $j$  and rotational state. Provided that no overlaps result, the move is accepted with probability  $\exp(\beta\mu_j - \beta\mu_i) \times N_i/(N_j + 1)$ . Note that the available shapes  $j$  are determined by those present in the simulation; that is, which have defined chemical potentials. “Piece switch” moves preserve both shape and rotational state. The locations of two pieces are switched, again using the anchor points to define the location of each piece.

If there are no overlaps, the move is accepted. The identity change and piece switch moves are potentially useful in multi-component simulations where demixing may occur.

In any multi-component simulation, we attempt moves with relative frequencies of 3:3:9:2:2:1 (insertion:deletion:translation:rotation:identity change:piece switch). These weights were chosen as a compromise between efficiency at low and high densities. In simulations of one-component fluids identity-change and piece-switch moves were not used, and the relative frequencies of the remaining moves were unchanged. For simulations with at least one species at high chemical potential, insertion and deletion events tend to be infrequently accepted, and identity changes or piece switches become more important.

A simulation at a given state point consists of an equilibration phase followed by a data collection phase. For scans of many state points over a variety of conditions, the use of constant numbers of trial moves in the equilibration and data collection phases proved inefficient. We use automation and heuristics to determine when data collection can be begun at each state point and when sufficient statistical quality has been achieved that a simulation can be terminated. All quantities to be evaluated, such as density and mole fraction, are tracked via the block-average method described by Flyvbjerg and Petersen [129, 130]. Each block contains 3000 samples, and each sample is separated by 1000 trial moves. The block-average method is useful as it allows not only for the expectation value of interest to be calculated, but the variance of that quantity and an estimate of the error of that variance. The last part is most valuable, and with a certain minimal number of blocks (independent groups of samples), a complete set of results and estimate of their quality may be obtained.

The separation between samples was chosen to be on the order of the maximum number of pieces present in simulations at very high densities. The block length is chosen based

on preliminary runs and appears to provide reliable and uncorrelated block averages at all densities simulated. Data collection is not started until at least three blocks have been completed and the density and other quantities have converged according to an exponential criterion, viz.  $\ln(\rho_n/\rho_{n-1}) \leq 10^{-3}$ , where  $\rho_n$  represents the average density of the system sampled during block  $n$ .

Simulation of an individual state point is terminated in one of two ways. Standard termination occurs when at least 500 million trials have been performed. Early termination occurs when the relative standard error of the density is below 0.001 (0.1%), the relative standard errors in the mole fractions of all components in a mixture are less than 0.2 (20%), and at least 10 blocks (30 million trial moves) of data collection have been completed. In practice, convergence of the density is the more stringent criterion. Under nearly all conditions mole fractions have converged to well within 0.01 (1%) by the time the density has converged; the only exceptions are in high-density mixtures where one component is of exceedingly low ( $< 0.01$ ) mole fraction, for which quantity uncertainties of up to 0.15 (15%) are seen.

For these simulations, in our computer implementation the occupancies of all lattice sites are stored in a 512 byte integer vector, and bitwise operations are used to detect overlaps when evaluating trial moves. This approach provides for very high efficiency and low memory footprint. On a modern processor (Intel Q9400, at 2.66 GHz), our code performs 2.36 million Monte Carlo trials per second (estimate obtained by averaging over simulations at low, medium and high densities), and requires an average of 28 seconds to complete a simulation at a single state point to the satisfaction of our convergence criteria. It is thus possible to survey large portions of the multicomponent phase space in reasonable time. We also used Python and shell scripting tools to parallelize some phase space surveys across hundreds of processors simultaneously. This allowed rapid turnaround of results and remote creation and submission of jobs.

We have simulated systems ranging from pure species to seven-component mixtures. All single-component fluids were simulated over at least the chemical potential range  $-4.0$  to  $+8.0$  in increments of  $0.2$ , for 61 total values per fluid. All 21 two-component (binary) mixtures were also simulated, with the chemical potential of each component scanned over the same range for a total of 3721 state points per two-component mixture. Mirror symmetry of enantiomers was not used to reduce the number of simulations required, partly for convenience and partly to illustrate the quality of the data obtained. All possible ternary (three-), quaternary (four-), quinary (five-), senary (six-) and septenary (seven-component) mixtures were simulated, but only along the phase space “diagonals” where all species have equal chemical potentials,  $\beta\mu_i = \beta\mu_j = \beta\mu_k = \dots$ , again scanned from  $-4.0$  to  $+8.0$ . There are 35 each of ternary and quaternary mixtures, 21 each of binary and quinary mixtures, 7 senary mixtures, and a single septenary mixture.

Simulations were performed on a  $64 \times 64$  square lattice, under toroidal boundary conditions (periodic boundaries on both the  $x$  axis and  $y$  axis). A maximum of 1024 pieces can be present in a simulation cell of this size. To be confident this lattice was large enough that finite size effects were not significant, lattice sizes of  $8 \times 8$ ,  $16 \times 16$ ,  $32 \times 32$ , and  $48 \times 48$  were also tested. Properties such as the density and mole fractions were well-converged at the  $64 \times 64$  lattice limit.



## 4.3 Results

### 4.3.1 Single-component (pure) fluids

The packing fraction as a function of chemical potential,  $\eta(\beta\mu)$ , for all seven single-component fluids is given in Figure 4.2a, and the pressure plotted as a function of packing fraction,  $\beta p(\eta)$ , is given in Figure 4.2b; calculation of the pressure is described in the Appendix. The packing fraction is the fraction of lattice sites covered; each shape occupies four lattice sites, so the actual density (pieces per unit area) is 1/4 of this quantity. These data may be considered analogous to isotherms of  $\rho(\mu)$  or  $p(\rho)$  in a real system. The first form of the equation of state corresponds to the “raw” results of simulations in the grand ensemble, while the second corresponds to the way data is usually presented in studies using isothermal-isobaric and canonical ensemble simulations [95]. Again, simulations are performed from  $\beta\mu = -4.0$  to  $\beta\mu = 8.0$ , corresponding to occupancies ranging from below 0.10 to nearly 1.0 (complete filling). The isotherms for all shapes collapse onto a single curve at low chemical potentials. This is as expected; these are essentially gaseous systems with repulsive interactions and identical particle sizes, so should have very similar (though non-ideal) gas-like behavior at low densities. This point will be revisited in section 4.3.4, below. At higher chemical potentials, the differences between the shapes become more apparent. At all chemical potentials squares (*O* shapes) exhibit higher density (or packing fraction) than all other shapes. Rods (*I* shapes) are the second-densest, and have density similar to that of the remaining shapes until  $\beta\mu \simeq -1.0$ , after which they exhibit  $\eta(\beta\mu)$  behavior rather more like that of the squares. The curves for *S* and *Z* shapes are identical because they are enantiomers, as are the curves for the *J* and *L* shapes. At the same chemical potential, *S* and *Z* fluids are slightly denser than *J* and *L* fluids, and the fluid of *T* shapes

is the least dense at every chemical potential. In all cases, packing fractions smoothly approach the complete-filling limit at high chemical potential. The critical packing fraction for randomly-placed small rectangles on a lattice is near 0.67 [98], suggesting that these fluids must exhibit significant structure in order to achieve high densities. We have also obtained the isothermal compressibilities of all the pure fluids, which are entirely smooth and do not exhibit any significant features over this range of chemical potentials.

The smoothness of the density plots belies significant complexity in the structure of the fluids. Snapshots taken from simulations of the pure fluids are shown in Figure 4.4 and 4.5. In each case three snapshots are given, at chemical potentials corresponding to low, medium and high densities. In the fluid of squares, there is little structure apparent in the snapshot at low density, other than that which might be expected from the non-overlap condition. In the medium-density snapshot, at a packing fraction of approximately 0.8, significant short-ranged structure is visible, with the pieces arranged in small, well-aligned groups. These tend to be three to six squares across at this density. The appearance and growth of these groups appears to correspond to the feature in the  $\beta p(\eta)$  curves where the squares “break off” from the rods (Figure 4.2b). In the highest-density snapshot, near 95% coverage, the squares form larger domains, some of which extend over the entire length of the simulation cell. We note that these structures break up and re-form during the simulation. At these high densities a sort of one-dimensional ordering is observed in which the great majority of the pieces in the system are anchored on a lattice site with (in this case) an even-numbered  $y$ -coordinate; in the snapshot shown, only a few odd-anchored pieces are visible in the lower left. This behavior occurs because alignment in one direction increases translational mobility in the other, providing an overall entropic stabilization. As the packing fraction increases from 95% through 99.5%, this behavior becomes more prevalent and pronounced. While this is suggestive of the appearance of a true crystal phase, high-resolution scans in

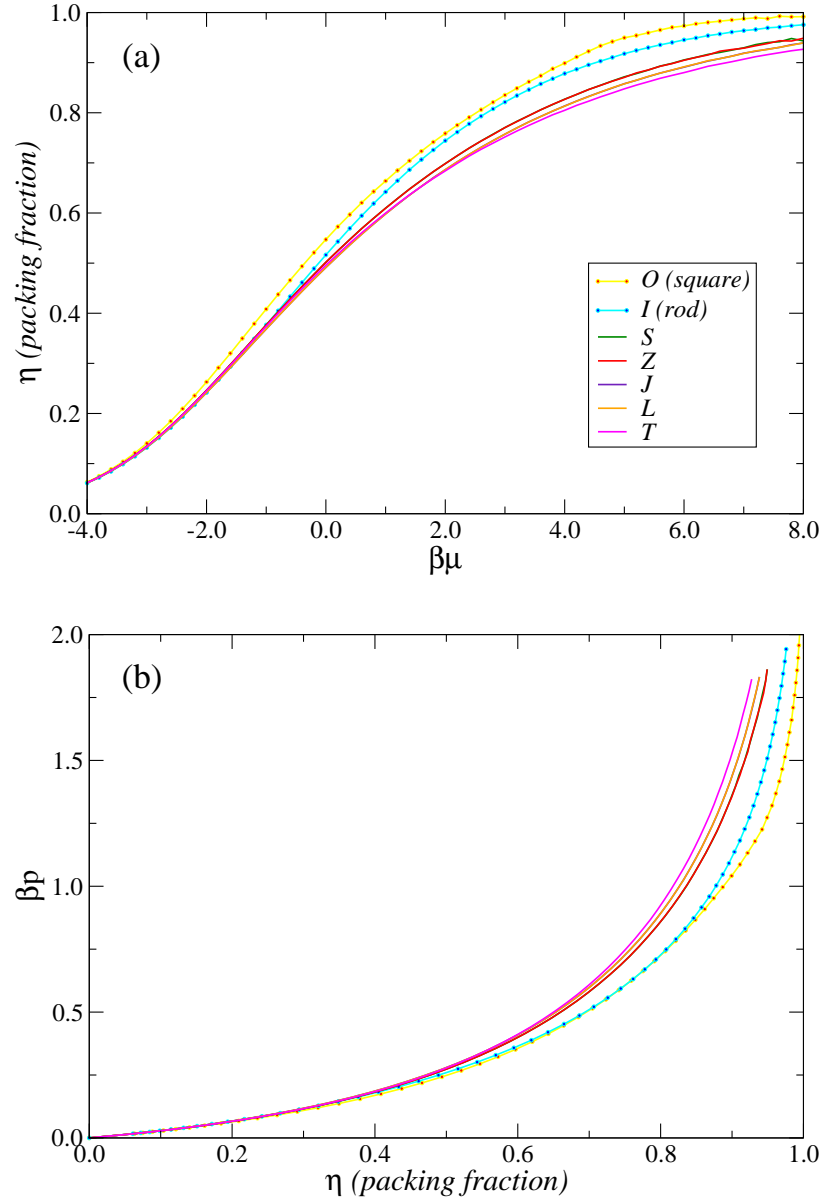


Figure 4.2: (a) Packing fraction  $\eta$  versus chemical potential  $\beta\mu$  for one-component fluids. (b) Pressure  $\beta p$  vs. packing fraction for one-component fluids. The color scheme in these plots is the same as for the shapes themselves (Figure 4.1).

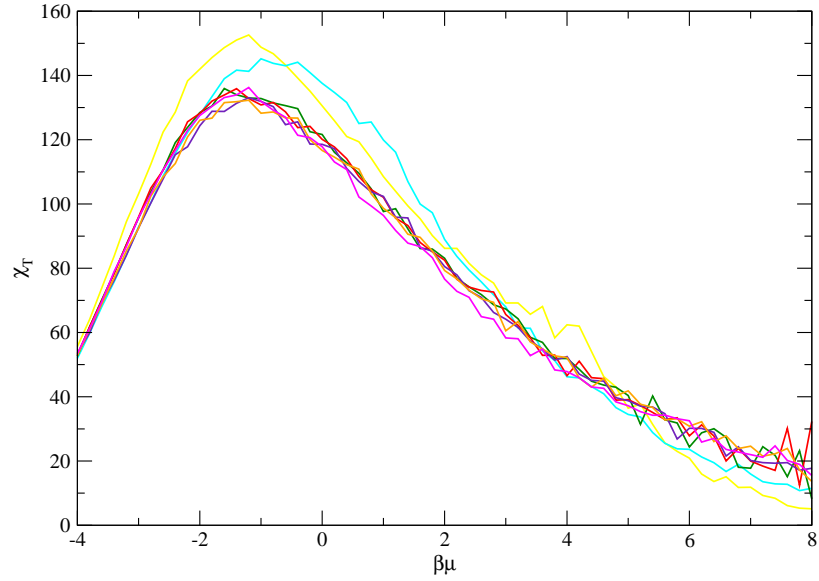


Figure 4.3: Isothermal compressibility  $\chi_T$  versus chemical potential  $\beta\mu$  for one-component fluids.

the chemical potential range 4.0 to 6.0 do not show any signature of an abrupt transition and there is the likelihood that these structures are artificially stabilized by the periodic boundary conditions used. Similar “columnar” behavior has previously been observed in constant-pressure simulations of off-lattice hard squares. These also do not exhibit a true crystallization transition, and the columnar behavior is thought to be due to the influence of the periodic boundary conditions [97]. As it turns out, this is not strictly a periodic boundary effect and is quite noticeable for larger polyominoes.

The structure of the fluid of rods (*I* shapes) is rather different. In the snapshots shown in Figure 4.4, rods of vertical orientation are shown in a lighter color than rods of horizontal orientation, to highlight the orientational structuring present in this fluid. Even at low density, significant orientational correlation is present in the rod fluid, with neighboring rods tending to orient parallel to each other. This behavior suggests a possible transition to a nematic phase at higher densities, but in fact this does not occur. As the density increases the local orientational correlation becomes stronger, but through a clustering mechanism

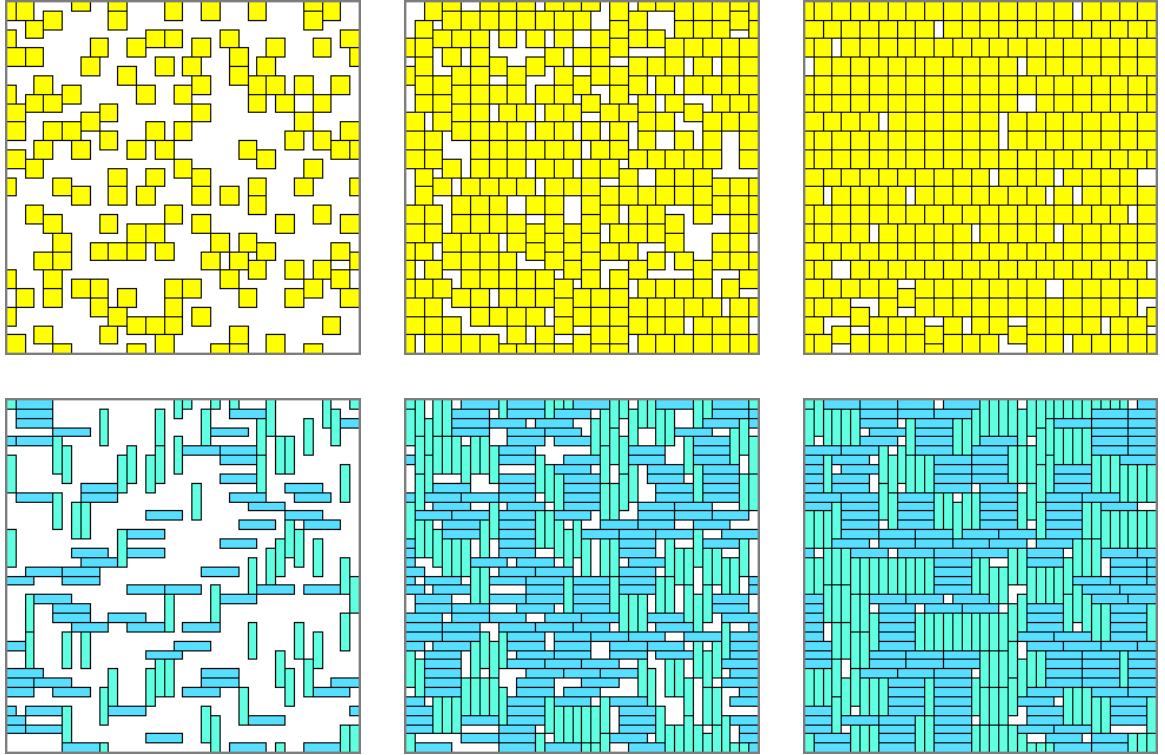


Figure 4.4: Configurations of pure fluids of squares and rods, at low (-1.0), medium (+3.0) and high (+7.0) chemical potentials. These are  $38 \times 38$  sections cut from  $64 \times 64$  simulation cells; as a result, pieces may extend over the boundary of the section shown. For the rods, which have two possible orientations, each orientation is shown in a slightly different color.

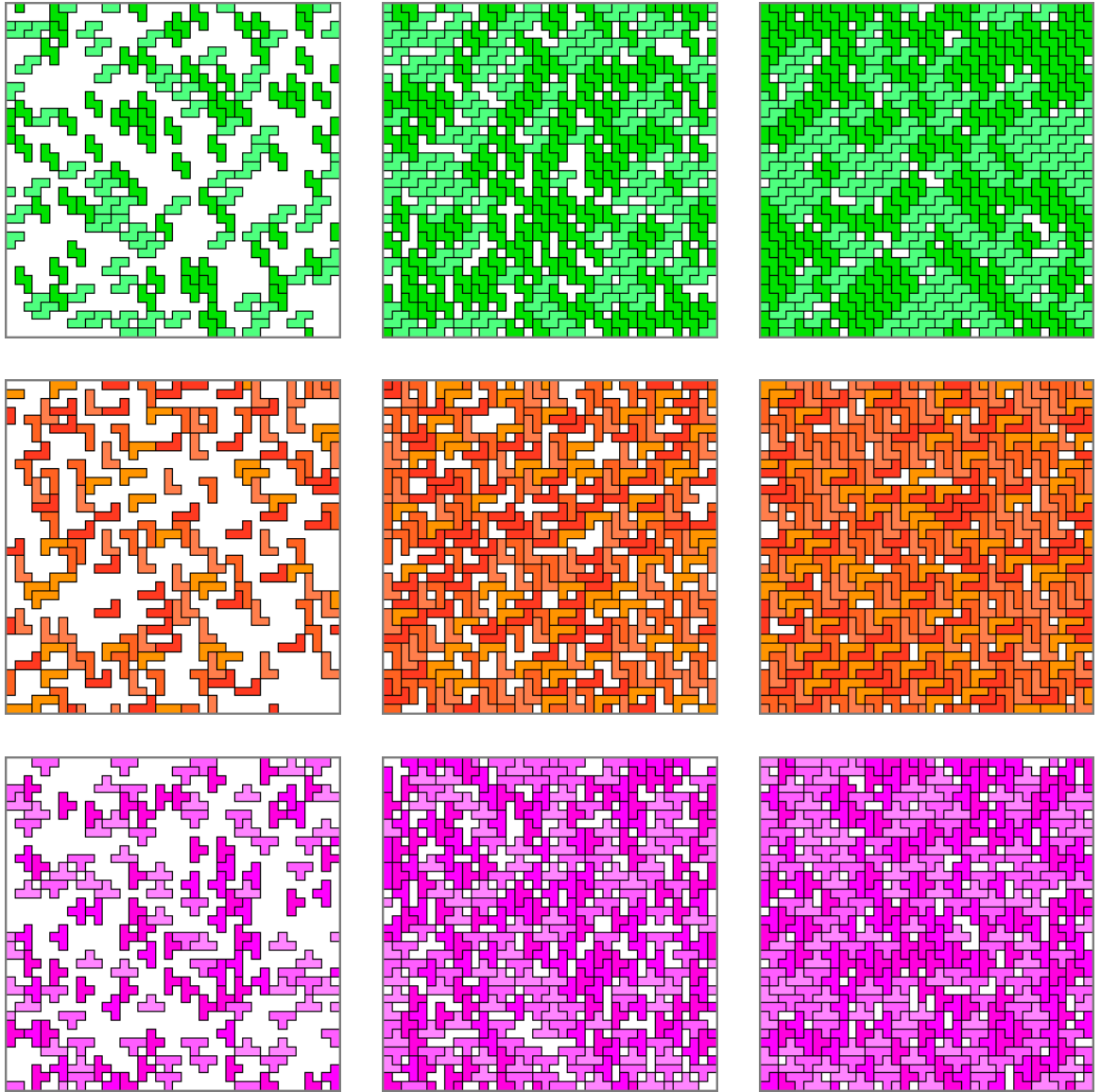


Figure 4.5: Configurations of pure fluids at low (-1.0), medium (+3.0) and high (+7.0) chemical potentials, for each of the  $S$ ,  $L$  and  $T$  shapes. These are  $38 \times 38$  sections cut from  $64 \times 64$  simulation cells; as a result, pieces may extend over the boundary of the section shown. As in Figure 4.4, each orientation is shown in a slightly different color.

that destroys any long-ranged correlation. In particular, at the middle density one observes clusters of approximately four parallel rods which are then oriented more-or-less randomly to each other. This behavior is similar to the “tetratic” ordering (which has elements of both horizontal and vertical order) observed in both off-lattice simulations of hard rectangles [99] and in experimental work on a quasi-two-dimensional system of a monolayer of disk-shaped colloidal particles standing on edge [131]. However, particles in these systems can take any orientation, while the on-lattice nature of our simulations allows for only two orientations of the rod clusters (reinforcing tetratic-like behavior), so the comparison is not wholly appropriate. At high density the clusters tend to grow somewhat larger, and a sort of layering is observed as they pack against like-oriented clusters. The apparent lack of an isotropic-to-nematic transition in this system is consistent with previous work. Ghosh and Dhar found that for packing fractions up to 0.85, only rods of length 7 or greater display an orienting transition on the square lattice [132]; we have performed additional calculations on rods of up to and greater than length 7, reaching packing fractions of 0.99, and also found no transition.

A related kind of ordering is observed in the fluids of *S* and *Z* shapes, of which the *S* fluid is shown in Figure 4.5. Again, even at low densities, there is clearly short-range orientational order visible in the fluid, with pieces preferring to align parallel with each other. At the medium density, two kinds of local structure are observed. In the first, and most common, neighboring pieces are offset in the diagonal  $(\pm 1, \pm 1)$  directions, which gives a “herringbone”-like structure. In the second, pieces are offset in the Cartesian directions  $(0, \pm 1)$  or  $(\pm 1, 0)$ , depending on whether they are in the vertical or horizontal orientations, respectively. Interestingly, at higher densities, the Cartesian offset structure is largely suppressed in favor of the herringbone structure. As in the case of the rods, large domains of uniform alignment and greater positional regularity appear at high densities, but no sharp

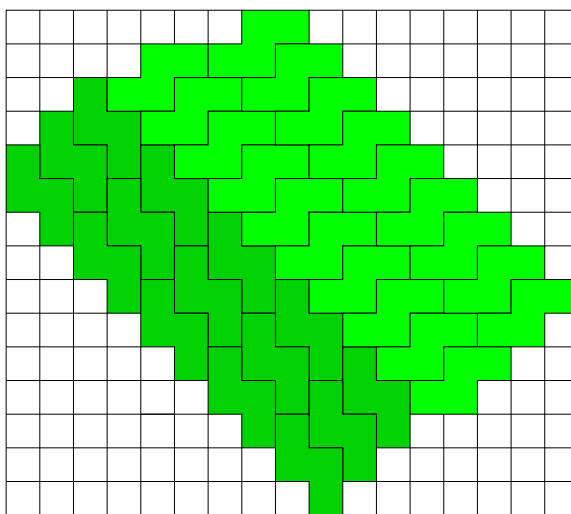


Figure 4.6: An example herringbone packing motif for an orientational interface of *S*-shapes, commonly observed in high density snapshots.

transition to a crystalline phase (ordered or not) is observed in the chemical potential range studied, and these domains remain much smaller than the system size.

The remaining shapes, the enantiomers *J* and *L* and the *T* shape, also display interesting orientational and positional ordering but of qualitatively different types, as shown in Figure 4.5. These shapes all have four distinguishable orientations, and unlike rod, *S* and *Z* shapes, preferentially associate with pieces of orientation different to their own. We first consider the *L* fluid. At low density, *L* pieces are frequently found in a “stacked” configuration, with neighbors of the same orientation displaced by a single diagonal step on the lattice, much as in the *S* and *Z* fluids. However, at higher densities, *L* pieces begin to orient antiparallel with each other to form compact  $2 \times 4$  site objects, which themselves pack efficiently along the Cartesian directions, much as in the fluids of squares and rods. The *T* fluid is also quite complex. At low densities, *T* shapes tend to be rotated  $90^\circ$  or  $180^\circ$  from their nearest neighbors. At higher densities, a prevalent packing motif appears to be a



stack of several like-oriented pieces offset by the lattice vectors  $(0, 2)$  or  $(2, 0)$ , with other pieces “fit” into the structure thus created in a less-regular way. Recall that the  $T$  fluid is the least dense of all the single-component fluids at a given chemical potential. This appears to be because the  $T$  shapes are the most compact of the pieces with four orientations. Void spaces in the  $T$  fluid allow for much more orientational freedom than in, say, the  $L$  fluid, and the associated entropy drives the  $T$  fluid towards lower density.

### 4.3.2 Two-Component Systems

We have also scanned the phase space of all 21 binary mixtures, simulating a total of 78141 state points. In all cases, the two shapes were fully miscible over the chemical potential range simulated, but substantial non-ideality was frequently observed, which we attribute to complex micro-scale fluid structure. Due to the large number of binary mixtures, only a selection of these systems will be discussed.

We first consider the two-dimensional equation of state  $\eta(\beta\mu_i, \beta\mu_j)$ , analogous to the isotherms of Figure 4.2 for one-component mixtures. Two of these are shown in Figure 4.7, as contour plots. In these plots, the low density state is found in the lower left corner, at low chemical potential of both species, and the highest density is found in the upper right corner, at high chemical potentials of both species. For species with similar properties, the plot should be approximately symmetric across the phase space diagonal  $\beta\mu_i = \beta\mu_j$ . In the square/rod mixture, substantial deviations from ideality are clearly evident. For example, the contour beginning at  $\beta\mu_O = +6.5$  and  $\beta\mu_I = -4.0$  gradually moves to higher  $\beta\mu_O$  and as  $\beta\mu_I$  is increased. Equivalently, increasing  $\beta\mu_O$  at constant  $\beta\mu_I$  decreases the total system density. That increasing the pressure in one of the two mass reservoirs to which

the system is connected would lead to a decrease in total system density was quite unexpected! This result is due to the rods disrupting the structure of the pure square fluid, and corresponds to a positive volume of mixing (technically, area of mixing, since the system is two-dimensional). Of course, at sufficiently high  $\beta\mu_I$  the total density again increases; this occurs here for  $\beta\mu_I > 4.0$ . A similar effect might be expected on the other side of plot, where squares are introduced into a dense fluid of rods, but following the contour beginning near  $\beta\mu_I = 6.0$  we see a much weaker effect. The difference between the effect of rods on the structure of the fluid of squares and the effect of squares on the structure of the fluid of rods can be seen in representative snapshots, shown in Figure 4.8. In the former case, at high rod density and low square density, the squares seem to fit well into the rod fluid, the structure of which is generally similar to that seen in Figure 4.4. In the latter case, at low rod density and high square density, this is not the case. The rods, which span two or more rows of squares, induce alignment between the one-dimensional rows of squares described earlier. This reduces the entropy of the system and hence destabilizes it; the equilibrium density is thus lowered in compensation. Additional vacancies created by lowering the density help the system regain some of the entropy lost via the induced alignment. Finally, the middle snapshot in Figure 4.4 in a mixture of squares and rods at the same chemical potentials (and nearly the same densities; the mole fraction of squares is 0.509 in the snapshot shown). Here the overall structure is dramatically perturbed, with both species still forming clusters, but of much smaller characteristic length scale.

The equation of state of the mixture of *S* and *Z* shapes (an enantiomeric pair), also shown in Figure 4.7, is necessarily symmetric about the  $\beta\mu_S = \beta\mu_Z$  axis. The contours at high  $\beta\mu_S$  and low  $\beta\mu_Z$  are very nearly vertical, indicating that *Z* shapes are almost perfectly solvated by the *S* fluid; they simply replace *S* pieces and the density does not change. A configuration from a near-equimolar mixture of *S* and *Z* shapes is shown in Figure 4.9, in

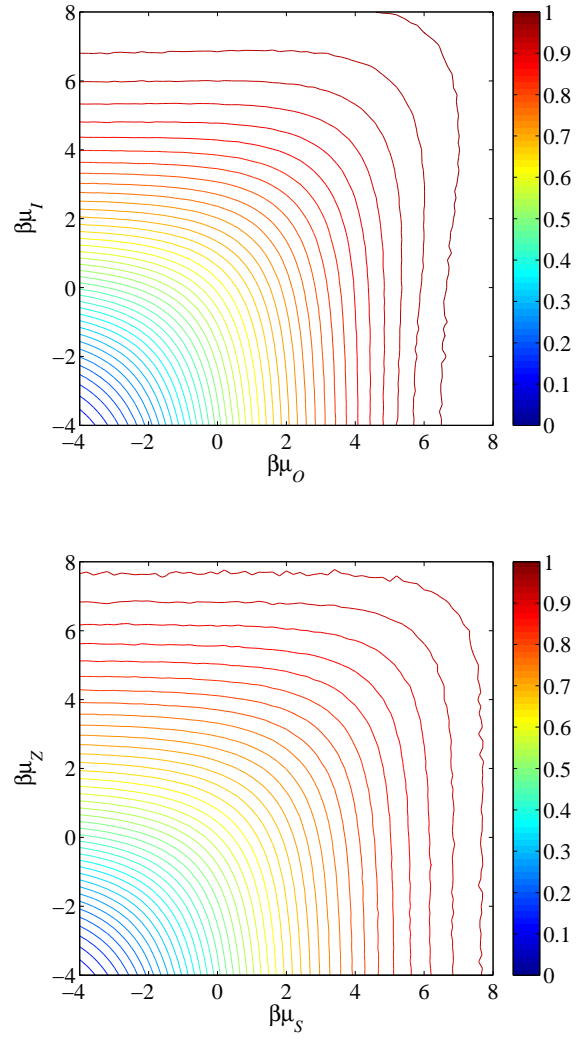


Figure 4.7: Contour plots of packing fraction versus chemical potentials for (top) mixtures of squares and rods, and (bottom) mixtures of  $S$  and  $Z$  shapes.

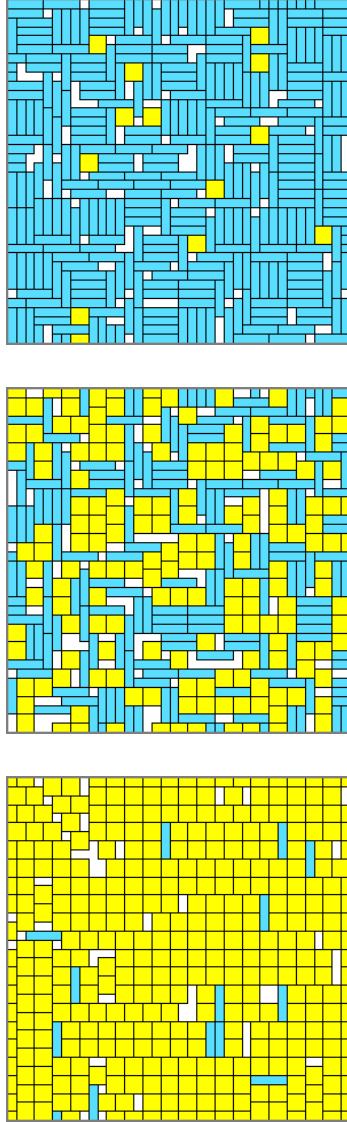


Figure 4.8: Snapshots taken from simulations of mixtures of squares and rods at (top)  $\beta\mu_O = 0.0$ ,  $\beta\mu_I = 6.0$ , (middle)  $\beta\mu_O = \beta\mu_I = 4.0$ , (bottom)  $\beta\mu_O = 6.0$ ,  $\beta\mu_I = 0.0$ . These are  $38 \times 38$  sections cut from  $64 \times 64$  simulation cells; as a result, pieces may extend over the boundary of the section shown. Rods are all shown in the same color regardless of orientation.

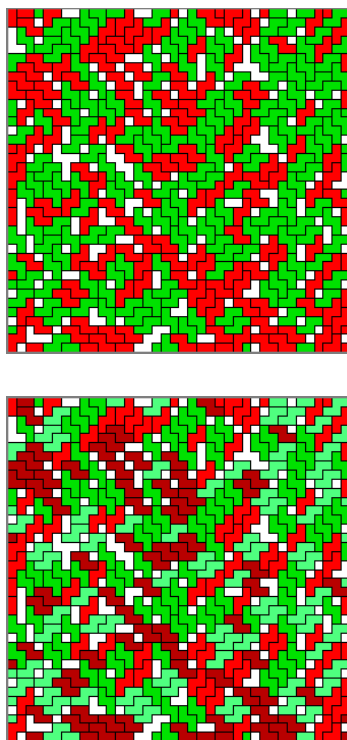


Figure 4.9: Snapshots taken from simulations of a mixture of  $S$  and  $Z$  shapes, at  $\beta\mu_S = \beta\mu_Z = 4.0$ , (top) without orientation-specific coloration, and (bottom) with orientation-specific coloration.

two different representations. As in the square/rod mixture, we see a dramatic tendency of the two species to segregate into “micro-clusters” (top image). This mixture displays herringbone-like structures as seen in the pure fluids, and the same sort of stacking motifs are also present. Interestingly, the bottom image in Figure 4.9 clearly indicates that the tendency of pieces of the same orientation to aggregate (as observed in Figure 4.5) is preserved in the mixture; individual  $S$  and  $Z$  pieces strongly prefer to associate with other pieces of both the same species and orientation. This behavior is further discussed in section 4.3.4. The virial analysis may be extended to five-site and larger polyominoes, as discussed in the next chapter.

Returning to the square/rod binary system, the structure of the fluid along the  $\beta\mu_0 = \beta\mu_1$  phase space diagonal (pictured in Figure 4.8) may be further analyzed in terms of average

cluster size, shown in Figure 4.10. For these purposes we take two pieces of like species to belong to the same cluster if they touch along any face; pieces with only “corner contacts” are not considered part of the same cluster. We see in this figure that the average sizes of clusters of both shapes remain small even up to very high densities, consistent with a picture of a globally well-mixed but locally clustered or phase-separated fluid. Interestingly, the rods form clusters that are over twice as large on average as those formed by squares. In the middle snapshot in Figure 4.8 we see, however, that the average size of the rod clusters is in fact misleading; the rods form a very large percolating cluster along with a number of very small isolated clusters. The clusters of squares, on the other hand, are distinct and well separated. The tendency of rod shapes to form large clusters was observed in all rod/shape binary pairs. However, a transferable hierarchy of cluster size is not otherwise present. For instance, while clusters of squares were largest in a square/ $S$  shape mixture, clusters of  $T$  shapes were largest in high density square/ $T$  mixtures. However, in the  $S/T$  mixture, clusters of  $S$  shapes were consistently larger than clusters of  $T$  shapes.

To more deeply probe the non-ideality of the binary mixtures, we have extracted the volume of mixing in each over the entire range of conditions simulated. These data, for selected binary systems, are shown in Figure 4.11. The conventional definition of the volume of mixing is:

$$\Delta V_{mix}(\mathbf{N}, \beta p) = V(\mathbf{N}, \beta p) - \sum_i \hat{V}_i(\beta p) N_i \quad (4.7)$$

where  $\mathbf{N}$  is the vector quantity of the  $N_i$ , the number of particles of each species, and  $\hat{V}_i(\beta p)$  is the molar volume of pure species  $i$  at pressure  $\beta p$ . The data in Figure 4.11 are normalized by system volume and given as percentages,  $(\Delta V_{mix}/V) \times 100\%$ , plotted against pressure and mole fraction. The complete procedure for calculating the pressures and volumes of mixing is given in the Appendix to this chapter. For an ideal solution, the volume of mixing is zero.

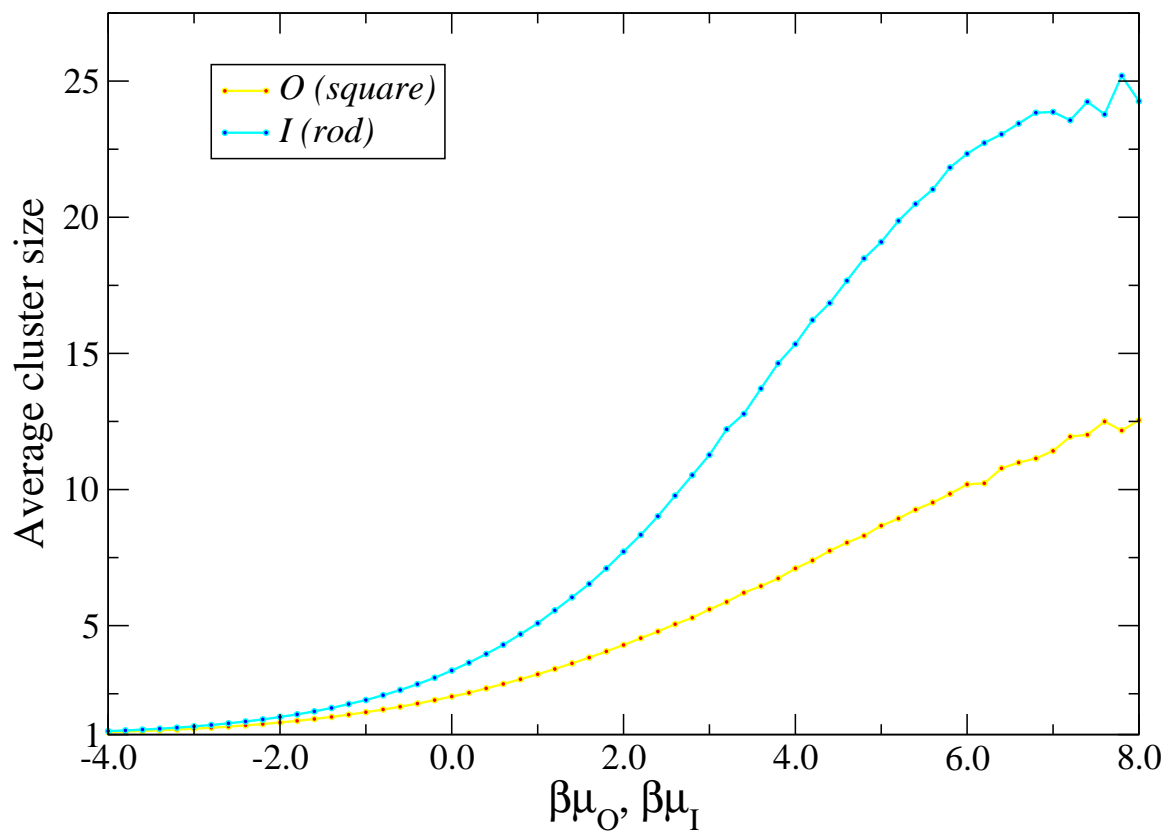


Figure 4.10: Average sizes of clusters of squares and rods in square/rod mixtures, along the  $\beta\mu_O = \beta\mu_I$  phase space diagonal.

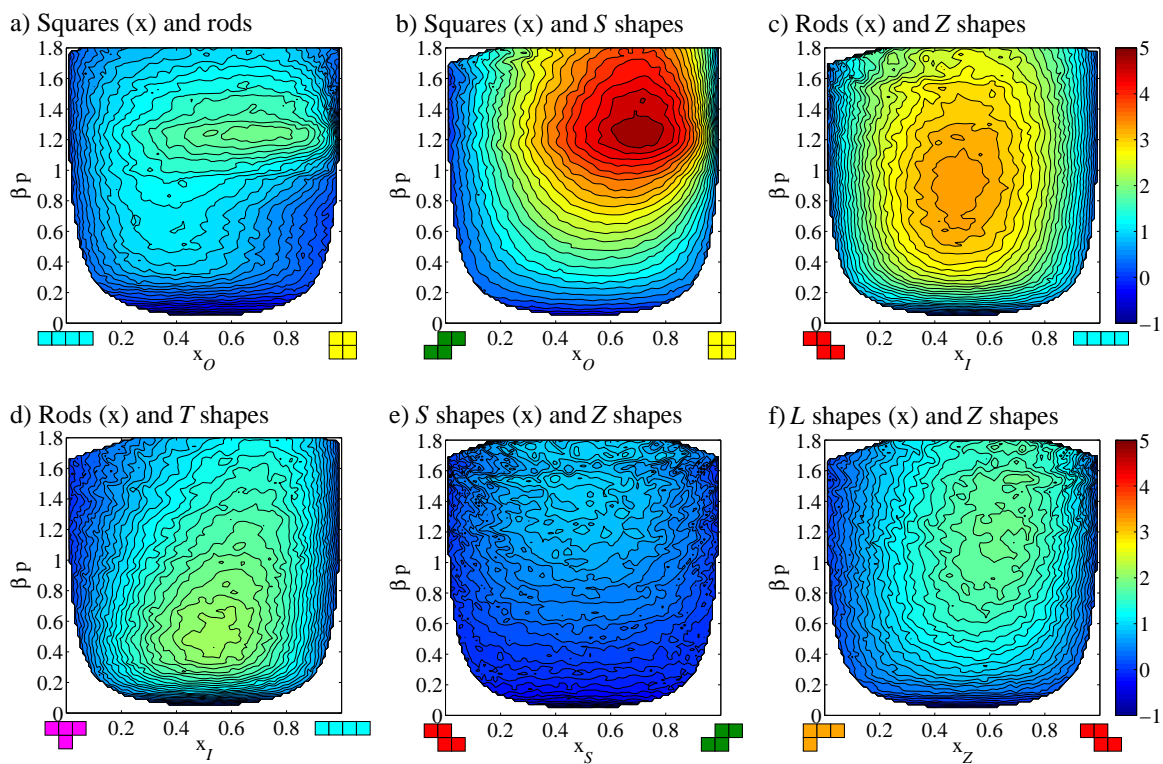


Figure 4.11: Contour plots of volume of mixing versus pressure  $\beta p$  and mole fraction  $x$  for various binary mixtures: (a) squares and rods, (b) squares and  $S$  shapes, (c) rods and  $Z$  shapes, (d) rods and  $T$  shapes, (e)  $S$  shapes and  $Z$  shapes, and (f)  $Z$  shapes and  $L$  shapes. In all cases the mole fraction shown is that of the first shape of the pair. All figures are plotted on the same vertical scale, in relative percentage units,  $(\Delta V_{mix}/V) \times 100\%$ .



All of the binary systems in this model are non-ideal, though to varying degrees. The mixture of squares and rods is strongly asymmetrical and peculiarly dependent on pressure, with a modest positive peak centered near  $x_O = 0.7$  and  $\beta p = 1.2$ . This corresponds to the substantial deviation from ideality already seen in Figure 4.7 and 4.8 — that introduction of rods into the square fluid at high density substantially perturbs the structure of that fluid, lowering the density (see Figure 4.7) until it is completely restructured near  $x_O = 0.5$ . At low pressure, however, the most positive volume of mixing occurs to the left of the  $x_O = 0.5$  line, on the plateau located at  $x_O = 0.4$  and  $\beta p = 0.6$ . The fluid density is much lower here, and this effect appears to be due to the presence of the squares interrupting the low-density orientational ordering behavior displayed in the pure rod fluid.

The square/ $S$  mixture is the most strongly non-ideal of all the binary systems, with a dramatic peak in the volume of mixing observed at  $x_O = 0.7$  and  $\beta p = 1.2$ . This peak is more than twice the height of that observed in the square/rod mixture. The reason for this is that the structures of the dense square fluid and the dense  $S$  fluid are fundamentally incompatible. The squares prefer to align along the Cartesian lattice directions with regular displacements of two lattice spacings, and clusters of squares have facets indexed along these lattice vectors. The  $S$  pieces prefer to align along the lattice diagonals, as discussed previously, and have facets indexed by the diagonal lattice vectors. In an aperiodic system, it is impossible to create a fully rectilinear cluster of  $S$  shapes without vacancies. In our simulations using a periodic boundary, a strip may be created which tiles a rectilinear domain. When not phase separated, the two structures are therefore incompatible: one cannot pack clusters of squares and clusters of  $S$  shapes together without either introducing vacancies at the interface or perturbing the structure of the clusters. This leads to a very significant positive volume of mixing of these fluids. Again, this effect is asymmetric

across the  $x_O = 0.5$  line, with squares clearly more compatible with (less perturbing to) the structure of the  $S$  fluid than vice versa, much as in the square/rod mixture.

Rods and  $Z$  shapes display the second largest positive volume of mixing of the systems shown, though at somewhat lower pressures and near to equimolarity. Rods are somewhat more compatible with the  $Z$  (or  $S$ ) fluid than are squares, because rod clusters are better able to distort and accommodate the characteristic diagonal facets of clusters of  $Z$  shapes. Nonetheless, this disrupts the rods' tendency to form small clusters aligned in both directions. This incurs a free energy cost, which the system alleviates by increasing the total volume, corresponding to  $\Delta V_{mix} > 0$ .

Of the remaining binary systems shown, rods and  $T$  shapes are most strongly non-ideal at pressures near 0.5, suggesting that the structures of these two fluids at even modest packing fractions (near 0.7) are particularly incompatible. At higher pressures, the peak in volume of mixing shifts to  $x_I > 0.5$ , suggesting that  $T$  shapes are less soluble in the rod fluid than are rods in the  $T$  fluid. The mixture of  $Z$  and  $L$  shapes is closer to ideal than any of those discussed so far, with a broad but low peak shifted slightly to the  $Z$ -rich side of the diagram. Finally, the mixture of  $S$  and  $Z$  shapes, already considered in Figures 4.7 and 4.9, is of course symmetric about  $x_S = 0.5$  and shows only very slightly positive volume of mixing at very high pressures, even while displaying significant microscopic segregation (Figure 4.9).

Mixtures containing rods exhibit  $\Delta V_{mix}$  maxima at generally lower pressures than other mixtures. In Figure 4.11 this is particularly evident for the rod/ $T$  mixture and the rod/ $Z$  mixture, but it is also true for rods and squares and the rod/ $L$  mixture not shown. This is another consequence of the pronounced local ordering that occurs in the rod fluid at lower densities (Figure 4.4). Finally, we note that at very low pressures and/or at mole fractions

very close to 1 or 0, many mixtures appear to display negative volumes of mixing. We are confident that this is a numerical artifact. Under these conditions the molar volume in one or both pure fluids becomes extremely large, and the correspondingly large statistical error in these quantities leads to large uncertainty in the (near-zero) volume of mixing. Note that it is possible for binary mixtures such as these to display a negative volume of mixing, as discussed below in section 4.3.4.

### 4.3.3 Many-Component Systems

We have simulated all multicomponent systems at many state points along the phase space diagonal, and find that the tendency of shapes to self-associate persists even when many components are present. To illustrate this behavior, snapshots from simulations of selected three-, four-, five-, six- and seven-component mixtures at high densities ( $\beta\mu = 7.0$ ) are shown in Figure 4.12. In all cases, clusters of each species are readily apparent, which is true in every multicomponent mixture that we have visualized. As in the binary mixtures, pieces are well-mixed at large length scales, and we have no evidence for any sort of first-order fluid-fluid transition in these systems. Furthermore, even when many different shapes are present, there is no tendency to form clusters or characteristic structures composed of more than one shape.

We have obtained the average sizes of the clusters of each shape in each of these simulations, shown in Table 4.1. As the number of components increases, the average size of clusters of a given species decreases. Most of this effect is simply due to dilution; the tendency to form clusters must be significantly reduced as the number of particles of a given shape decreases. For instance, in the *S/Z/T* ternary mixture, the average size of *S* (or *Z*) clusters at high pressure reaches as high as 3.364, while in the *O/I/S/Z/J/L* senary

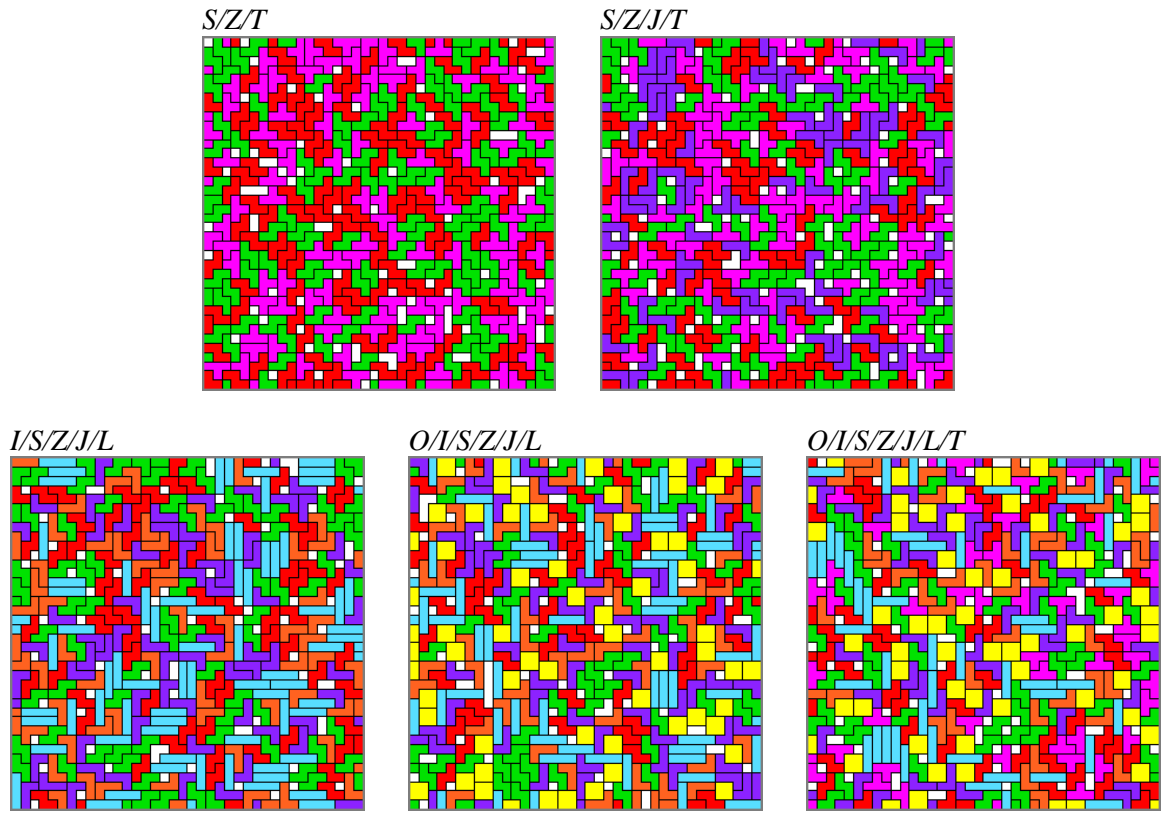


Figure 4.12: Representative snapshots of selected three-, four-, five-, six- and seven-component mixtures, with all species at  $\beta\mu = 7.0$ . These are  $38 \times 38$  sections cut from  $64 \times 64$  simulation cells; as a result, pieces may extend over the boundary of the section shown. All pieces of a given shape are shown in the same color, regardless of orientation.

Mixture	Average size of clusters of species:						
	<i>O</i>	<i>I</i>	<i>S</i>	<i>Z</i>	<i>J</i>	<i>L</i>	<i>T</i>
<i>O/I</i>	11.407	24.041					
<i>S/Z/T</i>			3.354	3.364			2.962
<i>S/Z/J/T</i>			2.284	2.248	2.415		2.181
<i>I/S/Z/J/L</i>		2.450	1.826	1.828	1.932	1.933	
<i>O/I/S/Z/J/L</i>	1.769	2.051	1.628	1.628	1.703	1.698	
<i>O/I/S/Z/J/L/T</i>	1.608	1.836	1.517	1.518	1.568	1.570	1.550

Table 4.1: Average size of clusters of each shape, from simulations at  $\beta\mu_i = 7.0$  for all  $i$ , for the mixtures shown in Figures 4.8 and 4.12. Statistical uncertainty in these data is  $\pm 0.005$  at 95% confidence.

mixture, it is reduced to very nearly half that value, 1.628. There is nonetheless significant information contained in the cluster size data. In the two systems containing rods, the clusters of rods are substantially larger than those of other shapes. One might suspect that this is simply due to the ability of rods to make contacts at larger separation than other pieces. However, upon inspection of the snapshots in Figure 4.12, we see that rod clusters tend to be closely packed rather than extended, which suggests that in fact the rods aggregate more strongly than the other pieces. In the *S/Z/J/T* quaternary mixture, the *S* and *Z* cluster sizes differ by a statistically significant 0.036, while in the *S/Z/T* ternary mixture they are the same to within the uncertainty of the measurement. This is a result of the two enantiomers interacting differently with the (also chiral) *J* shape in the quaternary mixture. In the senary and septenary mixtures shown, both members of each chiral pair are present, and there is no enantiomeric resolution. Finally, in the two systems containing squares, squares form larger clusters than any other shape besides rods, despite the compactness of the squares reducing their ability to make contacts at large distance. Squares also only have eight sites of contact, tied for the lowest among tetrominoes. Yet, the squares form large clusters.

An approximate combinatorial argument can provide further insight regarding the mean cluster sizes. In the dense fluids shown in Figure 4.12, nearly all pieces have 4, 5 or 6

neighbors. We can make an approximate prediction of the average cluster size in a “well-mixed” equimolar fluid by using combinatorics to predict the probability that a randomly chosen particle will have a certain number of neighbors of the same shape as itself, and then using these values as estimates of the probability distribution of different cluster sizes. For an exactly equimolar seven-component mixture, assuming that each piece has six neighbors, the probability that a chosen piece has zero “like” neighbors is approximately 0.396, the probability of one “like” neighbor is also 0.396, and the probability of two “like” neighbors is 0.165. Assuming that this is also the distribution of clusters of one, two and three pieces, respectively, we obtain an average cluster size of 1.50. If each piece has only five neighbors, then the average cluster size predicted in this way is 1.39; for pieces with four neighbors, 1.32. Such a simple argument will under-predict the average cluster size, but not by a large amount; a “well-mixed” fluid should therefore be expected to have average cluster sizes near to 1.4. Significantly, in the simulated seven-component mixture, all shapes have average cluster sizes larger than this, with squares and rods in particular forming much larger clusters than would be expected from random placement. In the seven-component mixture, then, all of these shapes prefer to self-associate.

#### 4.3.4 Analysis of Virial Coefficients

In order to better understand the interactions between different shapes, we have calculated all of the second virial coefficients  $B_{ij}$ , as defined by the expansion of the pressure of a binary  $i, j$  mixture in powers of the densities of both species:

$$\beta p = \rho_i + \rho_j + B_{ii}\rho_i^2 + 2B_{ij}\rho_i\rho_j + B_{jj}\rho_j^2 + \dots \quad (4.8)$$

$B_{ij}$	$O$	$I$	$S$	$Z$	$J$	$L$	$T$
$O$	4.50	5.00	5.00	5.00	5.00	5.00	5.00
$I$	5.00	5.75	5.75	5.75	5.75	5.75	5.75
$S$	5.00	5.75	5.25	5.25	5.50	5.50	5.25
$Z$	5.00	5.75	5.25	5.25	5.50	5.50	5.25
$J$	5.00	5.75	5.50	5.50	5.50	5.625	5.50
$L$	5.00	5.75	5.50	5.50	5.625	5.50	5.50
$T$	5.00	5.75	5.25	5.25	5.50	5.50	5.25

Table 4.2: Matrix of second virial coefficients  $B_{ij}$ . Note that these coefficients are exact.

These are obtained from the lattice analog of a cluster integral [133, 134]:

$$B_{ij} = -\frac{1}{2} \sum_k f_{ij}(k) \quad (4.9)$$

where  $f_{ij}(k) = 0$  if pieces of types  $i$  and  $j$  do not overlap if placed in a configuration indexed by  $k$ , and  $f_{ij}(k) = -1$  if they do overlap. In the summation  $k$  runs over all possible configurations (that is, orientations and relative displacements) of two pieces. Because the number of such configurations is enumerable this sum can be evaluated exactly; the resulting  $B_{ij}$  values are shown in Table 4.2. Likewise, an “orientation-specific virial coefficient”  $B'_{ij}$  is defined by taking the two pieces in specific orientations and only summing over relative displacements. These “orientation-specific coefficients” are shown in Table 4.3.

The  $B_{ij}$  are clearly measures of how “strongly” two pieces overlap. They are all necessarily positive, and contribute to increasing the pressure of a fluid over its ideal value. Low values may be interpreted as indicating a more “favorable” interaction than high values, though of course there is no direct attraction between any of the shapes. These values may also be compared to the virial equation of state for the hard disk model. For that model it is well known that the magnitude of the second virial coefficient is exactly twice the area of the disk ( $B_2 = \frac{\pi}{2}(2r)^2 = 2a_o$ ). If our virial coefficient results were divided by the area of a tetromino, the resulting scaled virial would provide an approximate comparison of the

$B'_{ij}$	$O1$	$I1$	$I2$	$S1$	$S2$	$Z1$	$Z2$	$J1$	$J2$	$J3$	$J4$	$L1$	$L2$	$L3$	$L4$	$T1$	$T2$	$T3$	$T4$
$O1$	4.5	5.0	5.0	5.0	5.0	5.0	5.0	5.0	5.0	5.0	5.0	5.0	5.0	5.0	5.0	5.0	5.0	5.0	5.0
$I1$	5.0	3.5	8.0	6.5	5.0	6.5	5.0	5.0	6.5	5.0	6.5	5.0	6.5	5.0	6.5	6.5	5.0	6.5	5.0
$I2$	5.0	8.0	3.5	5.0	6.5	5.0	6.5	6.5	5.0	6.5	5.0	6.5	5.0	6.5	5.0	5.0	6.5	5.0	6.5
$S1$	5.0	6.5	5.0	4.5	6.0	5.5	5.0	5.5	5.5	5.5	5.5	6.0	5.0	6.0	5.0	5.0	5.5	5.0	5.5
$S2$	5.0	5.0	6.5	6.0	4.5	5.0	5.5	5.5	5.5	5.5	5.5	5.0	6.0	5.0	6.0	5.5	5.0	5.5	5.0
$Z1$	5.0	6.5	5.0	5.5	5.0	4.5	6.0	6.0	5.0	6.0	5.0	5.5	5.5	5.5	5.5	5.0	5.5	5.0	5.5
$Z2$	5.0	5.0	6.5	5.0	5.5	6.0	4.5	5.0	6.0	5.0	6.0	5.5	5.5	5.5	5.5	5.5	5.0	5.5	5.0
$J1$	5.0	5.0	6.5	5.5	5.5	6.0	5.0	5.5	6.0	4.5	6.0	5.5	5.5	5.5	6.0	6.0	5.0	5.5	5.5
$J2$	5.0	6.5	5.0	5.5	5.5	5.0	6.0	6.0	5.5	6.0	4.5	6.0	5.5	5.5	5.5	5.5	6.0	5.0	5.5
$J3$	5.0	5.0	6.5	5.5	5.5	6.0	5.0	4.5	6.0	5.5	6.0	5.5	6.0	5.5	5.5	5.5	5.5	6.0	5.0
$J4$	5.0	6.5	5.0	5.5	5.5	5.0	6.0	6.0	4.5	6.0	5.5	5.5	5.5	6.0	5.5	5.0	5.5	5.5	6.0
$L1$	5.0	5.0	6.5	6.0	5.0	5.5	5.5	5.5	6.0	5.5	5.5	5.5	6.0	4.5	6.0	6.0	5.5	5.5	5.0
$L2$	5.0	6.5	5.0	5.0	6.0	5.5	5.5	5.5	5.5	6.0	5.5	6.0	5.5	6.0	4.5	5.0	6.0	5.5	5.5
$L3$	5.0	5.0	6.5	6.0	5.0	5.5	5.5	5.5	5.5	5.5	6.0	4.5	6.0	5.5	6.0	5.5	5.0	6.0	5.5
$L4$	5.0	6.5	5.0	5.0	6.0	5.5	5.5	6.0	5.5	5.5	5.5	6.0	4.5	6.0	5.5	5.5	5.5	5.0	6.0
$T1$	5.0	5.0	6.5	5.0	5.5	5.0	5.5	6.0	5.5	5.5	5.0	6.0	5.0	5.5	5.5	5.5	5.5	4.5	5.5
$T2$	5.0	6.5	5.0	5.5	5.0	5.5	5.0	5.0	6.0	5.5	5.5	5.5	6.0	5.0	5.5	5.5	5.5	5.5	4.5
$T3$	5.0	5.0	6.5	5.0	5.5	5.0	5.5	5.5	5.0	6.0	5.5	5.5	5.5	6.0	5.0	4.5	5.5	5.5	5.5
$T4$	5.0	6.5	5.0	5.5	5.0	5.5	5.0	5.5	5.5	5.0	6.0	5.0	5.5	5.5	6.0	5.5	4.5	5.5	5.5

Table 4.3: Matrix of “orientation-specific second virial coefficients”  $B'_{ij}$ . The orientations of each piece are numbered according to the scheme described in Figure 4.1. These coefficients are exact.



excluded volume between that shape (or specific orientation) and hard disks. In general, the scaled virials of tetrominoes would be smaller than the second virial coefficient of hard disks (indicating lower excluded volume). Scaling of virial coefficients thus makes comparison of different size objects possible. In the  $B_{ij}$  matrix of Table 4.2, a variety of interesting features are seen. Consider first the diagonal values, corresponding to the second virial coefficients of the seven pure fluids. These are all of the same magnitude, because the shapes all occupy the same number of sites and have similar lateral extent. Nonetheless, the variation is significant. The value for squares,  $B_{OO} = 4.5$  is the lowest, while the value for rods,  $B_{II} = 5.75$ , is the highest. Of the remaining, the  $S$ ,  $Z$  and  $T$  values of 5.25 are slightly lower than the  $J$  and  $L$  values of 5.5. One would expect based on these data that the squares would have the highest density at a given pressure, followed in turn by  $S$ ,  $Z$  and  $T$ ,  $J$  and  $L$ , and finally the rods. While the squares do in fact have the highest density at a given pressure, this argument fails to predict the high density of the rods, and does not distinguish between the  $S$  (or  $Z$ ) and  $T$  shapes at all. Another feature of these data is that the  $B_{OX}$  all have the same value for  $X \neq O$ , which is due to the squares having higher symmetry than any other shape. Interestingly, all the  $B_{IX}$  are the same for  $X \neq I$  and  $X \neq O$ , and rods have the second-highest symmetry.

Likewise, the  $B_{ij}$  clearly do not tell the whole story in regards the behavior of binary mixtures. For example, while the  $B_{IZ}$  value of 5.75 is certainly larger than  $B_{ZZ} = 5.25$ , it is the same as the coefficient for pure rods, and does not seem to correlate with the significant positive volume of mixing seen in Figure 4.11. The coefficient for squares and  $S$  shapes,  $B_{OS} = 5.0$ , is smaller even than  $B_{SS} = 5.25$ , which does not correlate at all with the extremely large positive volume of mixing in this system. To better understand these effects we turn to the “orientation-specific coefficients”  $B'_{ij}$  in Table 4.3.

Firstly, the two values for  $B'_{II}$  explain the discrepancy of the density of the rod fluid and the high value of  $B_{II}$ . Like-aligned rods have  $B' = 3.5$ , the lowest value on the table, while unlike-aligned rods have  $B' = 8.0$ , the highest. The average of these two gives the high  $B_{II} = 5.75$ , but since there is significant orientational clustering in the rod fluid, the “effective” value should be much lower (closer to 3.5), accounting for the very high density of this fluid. For the pure  $S$  (and  $Z$ ) fluids, we see that again the diagonal values of  $B' = 4.5$  are lower than the off-diagonal values of  $B' = 6.0$ , in accord with the earlier observation that these pieces tend to form clusters with all pieces in the same orientation. In the pure  $J$  and  $L$  fluids, different behavior is observed. Of the four orientations, each prefers to associate with (that is, has the lowest  $B'$  value for) the  $180^\circ$  rotation of itself. That is,  $J1$  and  $J3$  are a preferentially associating pair, with  $B' = 4.5$ , as are  $J2$  and  $J4$ . This again, is consistent with the behavior seen in the snapshots of Figure 4.5. The  $Ji-Ji$  association, corresponding to the diagonal-offset “stacking” seen at low densities, has  $B' = 5.5$ , the second lowest value. The  $90^\circ$  associations ( $J1-J2$ , etc.) are the least favorable, and are less common in the snapshots. Finally, somewhat similar behavior is observed in the pure  $T$  fluid, with a strong preference for the  $T1-T3$  and  $T2-T4$  associations, with  $B' = 4.5$ , over all others, with  $B' = 5.5$ .

Considering the  $B_{ij}$  and  $B'_{ij}$  values for  $i \neq j$ , we see that, while the  $B_{ij}$  suggest possibly favorable associations between pieces of different shape, taking orientation into account shows a substantially different picture. The lowest  $B'$  for any binary mixture is 5.0, while for every pure species there is at least one value of 4.5 or below. This suggests that every shape packs better with its own kind than with any other, provided they are allowed to adopt favorable orientations.

Although the strongest associations are between pieces of the same shape (though not necessarily in the same orientation), in binary mixtures there are still preferred orientations

for associations between pieces of different shape. For example, for neighboring  $S$  and  $Z$  pieces, the preferred orientations are between the pairs  $S0-Z1$  and  $S1-Z0$ , that is, with one piece turned  $90^\circ$  to the other. In fact, looking at the snapshot in Figure 4.9 this motif is often, though not always, adopted at the interface between clusters of  $S$  shapes and clusters of  $Z$  shapes. We also see a significant difference in the interactions of the members of the enantiomers; the  $S-J$  coefficients (equal to those of the  $Z-L$  pair, of course) are substantially different from the  $S-L$  ( $Z-J$ ) ones. The  $S-J$  coefficients are all the same,  $B' = 5.5$ , in fact, while in the  $S-L$  case there is orientational preference, with  $S1$  pieces preferring association with  $L2$  and  $L4$  ( $B' = 5.0$ ) over association with  $L1$  and  $L3$  ( $B' = 6.0$ .) This reflects the enantiomeric resolution discussed earlier.

Finally, we note that it is possible in this system to obtain a negative volume of mixing at pressures sufficiently low that the virial equation of state truncated at second order is accurate. We have verified numerically that this occurs in the rod/square mixture. The requirement of accuracy at second order means that the effect is seen only at extremely low pressures and densities and is therefore very small; nonetheless it is curious to see a negative volume of mixing between two dilute gases with purely repulsive interactions.

### 4.3.5 Solubility and solvation

To further probe the interaction between different shapes we turn to Henry's Law coefficients, which measure the solubility of one species in a fluid composed of others. The Henry's Law constant  $K_i$  for solute  $i$  in a given solvent is defined by  $f_i^\infty(T, p, x_i) = x_i K_i(T, p)$ , where  $x_i$  is the mole fraction of species  $i$  and  $f_i^\infty$  is the fugacity of species  $i$  at infinite dilution, which in a real liquid is similar to its partial pressure in the coexisting vapor. In our athermal model, this becomes  $\beta f_i^\infty(\beta p, x_i) = x_i \beta K_i(\beta p)$ .  $\beta K_i$  measures the

ratio of fugacity to mole fraction for the solute at infinite dilution; when its value is very small, species  $i$  is very soluble, and when its value is large, species  $i$  is very insoluble. The inverse quantity  $1/\beta K_i$ , therefore, is a measure of solubility: it reports the mole fraction of solute that would be attained at unit solute fugacity (partial pressure), if the Henry’s Law region extended to such high mole fraction<sup>1</sup>.

In fact, simulations indicate that these systems display Henry’s Law behavior only for mole fractions significantly below  $x = 0.001$ , indicating strong non-ideality. We have measured these constants for each shape dissolved in each pure fluid and in a large number of multicomponent solvents, all at several pressures. The details of this calculation are given in the Appendix. A selection of these data at  $\beta p = 0.5$  are shown in Table 4.4. This pressure corresponds to packing fractions near 0.65 for all the solvents considered. We first consider the various shapes dissolved in pure fluids. Overall, squares are always the most soluble, and rods are usually the least soluble. There is significant variation from solvent to solvent, however. Squares are themselves most soluble in the  $J$  and  $L$  fluids, and least soluble in the  $S$  and  $Z$  fluids. The latter is consistent with the large volume of mixing of squares and  $S$  shapes seen in Figure 4.11, which indicates poor compatibility between those two shapes. However, such behavior would not have been predicted from the virial coefficients; the cross-coefficients for squares and  $S$ ,  $Z$ ,  $J$  and  $L$  shapes are all the same. Rods, on the other hand, are most soluble in the fluid of squares, followed by the fluids of  $J$  and  $L$  shapes and  $T$  shapes, and are least soluble in the  $S$  and  $Z$  fluids. The  $S$ ,  $Z$  and  $T$  shapes are all mutually quite soluble, with  $S$  and  $Z$  being slightly more soluble in the  $T$  fluid than in each other, and  $T$  being more soluble in the  $S$  and  $Z$  fluids than in any other. This appears due to the strong similarity in shape of these three pieces, which share a “stepped” motif. We also see

---

<sup>1</sup>A common, though less rigorous, formulation of Henry’s Law is written  $c_i = k_H p_i$ , reflecting its original discovery [135]. Here large values of the constant  $k_H$  indicate high molar concentration  $c_i$  at given partial pressure  $p_i$ ;  $k_H$  is thus analogous to our  $1/\beta K_i$ .

Solvent	$\eta_s$	Solute Species						
		<i>O</i>	<i>I</i>	<i>S</i>	<i>Z</i>	<i>J</i>	<i>L</i>	<i>T</i>
<i>O</i>	0.696		0.218	0.168	0.168	0.196	0.196	0.167
<i>I</i>	0.694	0.232		0.146	0.146	0.159	0.159	0.149
<i>S</i>	0.660	0.227	0.147		0.210	0.168	0.174	0.205
<i>Z</i>	0.660	0.226	0.146	0.210		0.174	0.168	0.205
<i>J</i>	0.653	0.267	0.185	0.185	0.191		0.178	0.183
<i>L</i>	0.653	0.267	0.185	0.191	0.184	0.178		0.183
<i>T</i>	0.650	0.243	0.167	0.212	0.212	0.182	0.182	
<i>O/T</i>	0.664		0.193	0.202	0.202	0.195	0.195	
<i>S/J</i>	0.647	0.256	0.174		0.206		0.185	0.201
<i>L/T</i>	0.646	0.256	0.179	0.207	0.202	0.183		
Senary	0.649-56	0.253	0.176	0.192	0.192	0.185	0.184	0.191
Average		0.244	0.175	0.185	0.185	0.176	0.176	0.182

Table 4.4: Solubility ( $1/\beta K_i$ ) of each shape in various solvents at  $\beta p = 0.5$ . Values given are certain to within  $\pm 0.002$ . The first column contains the packing fraction of the solvent,  $\eta_s$ . The first seven rows of the table show the solubility of each shape in the pure fluids of each other shape. The diagonal values are missing because Henry’s law does not apply to components of the solvent. The next three rows show the solubility of various shapes in each of three binary mixtures, with both mixture components at the same chemical potential. The row labeled “Senary” shows the solubility of each shape in a 6-component mixture composed of all the other shapes, again all at the same chemical potential and  $\beta p = 0.5$ ; these solvents do not all have the same packing fraction, but they vary over only a small range, given in the  $\eta_s$  column. The final row gives the average of the solubility of each shape in the six other pure solvents; note that this quantity does not have a rigorous thermodynamic interpretation, and is only given for the sake of comparison.

evidence of chiral interactions in the solubilities of *J* and *L* in the *S* and *Z* fluids and vice versa. The solubility of *S* in *L* is the same as that of *Z* in *J*, and the *J*–*Z* (or *L*–*S*) pair is more mutually soluble than the *J*–*S* (or *L*–*Z*).

In the near-equimolar binary mixtures, the solubility of other shapes is generally intermediate between the solubilities in the corresponding pure fluids. For instance, squares are less soluble in the *S*/*J* mixture than in the pure *J* fluid, but more soluble than in the pure *S* fluid. This is consistent with the clustering behavior seen earlier, which suggests that, to a solute, the mixture looks like small regions of pure fluids. In a few cases, such as *J* dissolved in the

*O/T* mixture, shapes are as soluble in the mixture as in one of its components. In this case, the poor structural compatibility of the *O* and *T* fluids and their relatively large volume of mixing provides many voids into which the solute may fit. In one particularly interesting case, the *L* shape is noticeably more soluble in the *S/J* mixture than in either of the pure *S* or *J* fluids. There is a large positive volume of mixing in the *S/J* system, which is the likely cause.

In the “senary” row of Table 4.4 are shown the solubilities of each shape in the six-component mixture of the remaining shapes, again all at equal chemical potentials such that  $\beta p = 0.5$ . For comparison, the averages of the solubilities of each shape in the six other pure solvents are given in the last row. In all cases, the six-component mixture is a better solvent than one might expect from averaging over its components, though the difference is relatively small. Also, the trend established in the pure fluids remains, with squares being the most soluble of the shapes and rods being the least soluble.

Finally, we note that the ratio of the  $1/\beta K_i$  values for a species *i* in two different solvents is a partition coefficient which describes the distribution of a solute between them. At this pressure, the largest partition coefficient is for rods dissolved in square and *Z* (or *S*) solvents, with  $K_I(O/Z) = 1.49$ , a relatively modest preference for the fluid of squares. As the pressure is increased, the total solubilities decrease, but the partition coefficients can be greater; at  $\beta p = 1.00$ ,  $K_I(O/Z) = 2.14$ , but the solubilities are reduced to 0.015 in the fluid of squares and 0.007 in the *Z* fluid.

## 4.4 Discussion

The simulations described above provide a detailed picture of the structure and thermodynamics of both the single-component fluids and binary mixtures, as well as some insight into the behavior of many-component mixtures. The tetromino fluids do not display sharp (first-order) phase transitions in the density range studied, though there remains the possibility of continuous phase transitions without divergences in the compressibility or other signatures. However, they do display intriguing local structure, including clustering of like-oriented pieces in the pure fluids and localized strong species segregation in binary and multicomponent mixtures. That is, although only purely entropic forces are present in these systems, pieces appear to preferentially associate with other pieces of the same shape and complementary (though not necessarily identical) orientation. The qualitative picture of these interactions obtained through inspection of representative configurations is supported by analysis of several quantitative measures, including second virial coefficients, volumes of mixing, cluster size statistics, and solubilities in the form of Henry's Law constants. While related models have been used in a number of other simulation studies, the structure of the fluids and the associated thermodynamics have not been considered in any detail, and multicomponent mixtures have not been treated in any previous study of which we are aware.

While the structures adopted in the fluids of squares and rods is reasonably intuitive, the behavior of the remaining pieces is rather less so. All of the tetrominoes can be used to completely tile the lattice (100% packing) in a combinatorially large number of ways, including via well-ordered periodic structures. The structures of the  $J$ ,  $L$  and  $T$  fluids, while successfully rationalized in terms of piece-piece interactions, are not easily predicted, and one can easily imagine other structural motifs for packing these shapes at high densities. It

thus appears that using shape alone to direct self-assembly is perhaps more difficult than it might appear, since rather surprising behavior is observed even among such simple shapes.

The preference for association of pieces of like shape and complementary orientation, the solubilities of each species in the other fluids, and the volume of mixing data can all be interpreted via the usual chemical rule of thumb that “like dissolves like”, provided that one has an expansive interpretation of “like.” Consider, for instance, that squares and rods are the most and least compact of the shapes studied, yet are quite mutually soluble, while rods and *J* shapes are much less soluble in each other. Solubility is controlled by the compatibility of the solute with the characteristic structures formed in the solvent, rather than with the solvent pieces themselves. Squares are very soluble in the dense *J* fluid because the *J* pieces tend to pair, forming compact  $2 \times 4$  site structures, and a fluid of such structures is amenable to forming  $2 \times 2$  site vacancies, which exactly fit a square. Rods are much less soluble in the *J* fluid than are squares, despite “looking” more like *J* pieces than squares do, because the  $1 \times 4$  vacancy required to accommodate a rod requires a larger perturbation of the structure of the *J* fluid. Another type of compatibility occurs in fluid mixtures, between the characteristic structures formed by both shapes. Squares and rods have only modestly positive volume of mixing even at high densities, because both pieces form structures faceted along the Cartesian lattice vectors. *S* and *Z* shapes have nearly zero volume of mixing while displaying significant microscopic segregation, because they both form structures faceted along the lattice diagonals. Squares and *S* shapes, however, exhibit the most positive volume of mixing of any two species, due to the extreme incompatibility of their characteristic structures; rods and *S* shapes are nearly as incompatible.

It remains curious that in all the mixtures considered each shape prefers to associate with its own type rather than with any combination of others. The orientational virial coefficients provide some evidence that this should be the case: a shape’s lowest orientational virial is



always with itself. Another possible explanation for this behavior, or one possible reason for the virial results, is that the tetrominoes are quite thin (either one or two lattice spacings), and so their “face” on one side tends to be the same as that on the other; this is true for all the shapes except the *T*. This would lead to a natural tendency for shapes to pack efficiently in the same orientation, which is observed for the rods, *S* and *Z* shapes. *J* and *L* shapes also pack this way, but only at low densities; at high densities they rotate to make contact with the same face on another piece. *T* shapes form the most complex structures at high density, perhaps because they are unlike the other pieces in not having opposing faces of similar shape. Self-association is likely not a general feature of polyomino fluids; one can easily imagine larger shapes which exhibit “lock and key” shape complementarity, or frustrated structures that cannot pack efficiently with themselves<sup>2</sup>.

Much of this behavior can be predicted qualitatively by examination of second virial coefficients. The orientationally-averaged “thermodynamic” coefficients defined in eq 4.8 do not provide much insight into the fluid structure, but the orientationally-resolved coefficients correlate extremely well with behavior observed in the simulations. In nearly all cases, the relative orientation adopted by pieces in the dense fluids are those with the lowest orientationally-resolved coefficients. This suggests that these quantities may be useful in designing shapes that will exhibit a particular structure or packing motif; this should be equally true in systems which exhibit attractive interactions.

Increasing the number of components in a mixture decreases the tendency of each species to self-associate. This appears to be principally due to dilution, rather than any tendency for shapes to form characteristic multicomponent structures. Analysis of Henry’s Law data indicates that some many-component mixtures are generally better solvents (for shapes not present in the mixture) than were pure species or binary mixtures. Much of this behavior

---

<sup>2</sup>Many may consider the tetrominoes already sufficiently frustrating in this regard.

can be correlated with the volume of mixing in the solvent; when the solvent components do not mix well, the density of the fluid is lower (at a given pressure) than otherwise, and it becomes a better solvent for other species because it has more empty space available. Such a correlation is likely to be present for other polyominoes and perhaps real colloidal and nanoparticulate systems, and may suggest routes towards the systematic control of solvation behavior in such systems.

All of the fluids studied are fully miscible; no macroscopic phase separation was ever observed in these simulations. In off-lattice hard models, even in two dimensions, this is not always the case. For instance, demixing can be observed in mixtures of hard rectangles and disks or discorectangles [100]. Again, we expect that such phenomena may be observed in other (on-lattice) multicomponent polyomino fluids, especially when components are of substantially different size. Since an isotropic-to-nematic transition has already been identified for on-lattice rods of lengths greater than considered here [132], we believe that many single-component and multicomponent fluids of larger polyominoes are likely to exhibit true phase transitions. Extension of the model to three dimensions would increase the number of rotational states available and thus increase the likelihood of observing first-order transitions.

The off-lattice counterparts of some of the shapes considered here have been studied by other groups [98–101,132]. The behavior of the on- and off-lattice models is quite different, but this should not be surprising. In the off-lattice model, especially at high densities, the free energy of the fluid is principally determined by free volume considerations, and the structure adopted is one which maximizes the ability of individual objects to move about within the confinement of their neighbors. In the lattice model studied here, there is very little opportunity for such small-amplitude motions at high densities. Most importantly, the orientational degree of freedom in the lattice model is discrete, with very few states

available, so that the total entropy is dominated by translational terms; this is not the case in the off-lattice systems.

In conclusion, we have observed a number of interesting and previously unexplored phenomena in simulations of an idealized model with relevance to molecular adsorption and self-assembly in two dimensions. The extreme simplicity of the shapes studied and their interactions belies considerable complexity and non-ideality in the structure of the simulated fluids and mixtures. Quantities such as second virial coefficients, familiar from the analysis of simple liquids, and rigorous solution thermodynamics can nonetheless be used to correlate and understand most of this behavior. Larger polyominoes may exhibit true phase transitions, long-range ordering and even more complex behavior, and these results will be examined in the next chapter. We note in this regard that, even with an inexpensive model such as this and an efficient computer implementation, an exhaustive search of a seven-(or more)-dimensional phase space is likely beyond current computational capabilities. We believe statistical approaches for locating phase transitions in such a space based on ideas from quantitative stereology may prove useful [136]. Tetrominoes confined in small spaces may be induced to exhibit regular structure. If the confinement reinforces the characteristic structure of a fluid it will be enhanced, perhaps leading to pseudo-crystallization; on the other hand, an incompatible confinement geometry may be used to enhance fluid mixing. Confinement might also be used to effect a chromatographic separation based on liquid structure, rather than particle size; this will also be considered in future work. Finally, the results obtained to date may have some relevance to successful strategies for playing the Tetris computer game, but this has not been considered in detail.

## Appendices

### Calculation of pressure in multicomponent mixtures

In the athermal thermodynamics appropriate to this model, the Gibbs-Duhem equation is:

$$d\beta p = \sum_i \rho_i d\beta \mu_i \quad (4.10)$$

$$\beta p(\beta \mu) = \beta p(\beta \mu_0) + \sum_i \int_{\beta \mu_0}^{\beta \mu} \rho_i(\beta \mu') d\beta \mu'_i \quad (4.11)$$

(For a system with a real temperature, these expressions are still valid at constant  $\beta$ .) In principle, the integration in eq 4.11 is path independent (one can integrate through any set of  $\beta \mu_i$  state points). For a pure fluid the path selection is trivial and the quality of the result depends only on the spacing in  $\beta \mu$  between simulations. For each binary mixture of species A and B we have chosen to use rectilinear paths to reach each state point:

$$\begin{aligned} p(\beta \mu_A, \beta \mu_B) = p(\beta \mu_{A,0}, \beta \mu_{B,0}) &+ \int_{\beta \mu_{A,0}}^{\beta \mu_A} \rho_A(\beta \mu'_A, \beta \mu_{B,0}) d\beta \mu'_A \\ &+ \int_{\beta \mu_{B,0}}^{\beta \mu_B} \rho_B(\beta \mu_A, \beta \mu'_B) d\beta \mu'_B \end{aligned} \quad (4.12)$$

$\beta \mu_{A,0}$  and  $\beta \mu_{B,0}$  are chosen such that the density is very low, so that  $p(\beta \mu_{A,0}, \beta \mu_{B,0})$  can be accurately computed using the virial equation of state truncated at second order, Equation 4.8. The integration is a two step process:  $\beta \mu_{B,0}$  is held fixed while integrating up to the desired  $\beta \mu_A$ , after which  $\beta \mu_A$  is held fixed while  $\beta \mu_B$  is varied. Integrations were performed using Simpson's 1/3 integration. We examined different integration paths and found that the variation in  $\beta p$  due to choice of integration path was insignificant, confirming that the simulations are spaced closely enough in  $\beta \mu$  to provide reliable thermodynamics.

## Calculation of volume of mixing

The change in volume upon mixing is defined as:

$$\Delta V_{mix}(\mathbf{N}, \beta p) = V(\mathbf{N}, \beta p) - \sum_i \hat{V}_i(\beta p) N_i \quad (4.13)$$

where  $\hat{V}_i(\beta p)$  is the molar volume of pure species  $i$  at pressure  $\beta p$ . Our simulations of binary mixtures were performed in the grand ensemble, which necessitates several additional manipulations in order to obtain  $\Delta V_{mix}$  as it is conventionally used, as follows:

1. Obtain the equation of state,  $\beta p$  as a function of  $\beta \mu$  for each single-component (pure) fluid by thermodynamic integration, as described above.
2. For each species  $i$ , fit  $\hat{V}_i(\beta \mu_i)$  vs.  $\beta p(\beta \mu_i)$  via a cubic-spline function to provide  $\hat{V}_i(\beta p)$ .
3. Compute  $\beta p$  as a function of the chemical potentials  $\beta \mu$  for the desired mixture, again by thermodynamic integration. Combine this with the numbers of each shape  $\mathbf{N}(\beta \mu)$ , obtained in the simulation, to yield  $V(\mathbf{N}, \beta p)$ .
4. For each state point  $\beta \mu$ , compute  $\Delta V_{mix}$  via eq 4.13 .
5. Plot  $\Delta V_{mix}$  (or  $\Delta V_{mix}/V$ ) as a function of  $\beta p$  and mole fractions  $\mathbf{x}$ .

## Calculation of Henry's Law constants

In an athermal system, in the Henry's Law regime:

$$\beta f_i^\infty(\beta p, x_i) = x_i \beta K_i(\beta p) \quad (4.14)$$

that is, the fugacity of species  $i$  at infinite dilution in a particular solvent is equal to its mole fraction in the solution multiplied by a constant  $\beta K_i$ , which depends on both the solvent and solute and varies with pressure.  $\beta K_i$  is related to the excess chemical potential of the solute  $i$  at infinite dilution by [137, 138]:

$$\beta K_i(\beta p) = \rho_s \exp [\beta \mu_{i,ex}^\infty(\beta p)] \quad (4.15)$$

where  $\rho_s$  is the solvent density. We measure  $\beta \mu_{i,ex}^\infty$  via Widom test-particle insertion [139]. In the grand canonical ensemble

$$\beta \mu_{i,ex}^\infty = -\ln \langle \exp(-\beta \Delta U_i) \rangle_{\beta \mu, V} \quad (4.16)$$

where  $\Delta U_i$  is the energy associated with the insertion of a test particle of species  $i$  in the solvent, and the ensemble average is taken over both possible insertion positions (and orientations) and the positions and number of particles of other species present. Note that in the grand ensemble this expression applies only to the solute and not to the components of the solvent. In the hard model studied here, the term in  $\langle \dots \rangle$  brackets reduces to the ensemble average probability of successfully inserting a test particle of species  $i$  in the system when there are no other particles of species  $i$  present.

# Chapter 5

## Polyomino Fluids and Crystals

After our extensive study of the tetrominoes, the next logical step was examining the pentominoes, searching for more complicated behavior. In addition, a selection of larger polyominoes were studied. These included enlarged (size 16) versions of the tetrominoes, a series of high-symmetry shapes, and a family of shapes we refer to as “fish”. Tetrominoes displayed non-ideal mixing, “microscale phase separation”, and short-range geometric ordering. Pentominoes display much of the same microscale phase separation and clustering. The pentominoes also display fluid-to-solid phase transitions. Polymorphism (multiple solid phases) is observed in some pentominoes, and many larger polyominoes. In some larger polyominoes, we observe columnar behavior. Statistical mechanical models are used to assist in explaining the isotherms and stability of some polyomino solids.

### 5.1 Mathematical Research on Polyominoes

Most prior literature on polyominoes is found in mathematical journals, and mathematical challenges involving polyominoes were first popularized in the 1960s [9]. Mathematical researchers are generally concerned with different topics than we are in this dissertation,

but some of their work is useful when considering how to generate polyomino families or how to systematically categorize crystalline packings [10].

### 5.1.1 Enumeration

“Fixed” polyominoes cannot be rotated, and are the most commonly enumerated type of polyomino. “One-sided” and “free” polyominoes are subsets of the set of “fixed” polyominoes [140]. “One-sided” polyominoes considered equivalent if superimposable after rotation, while “free” polyominoes are allowed to both rotate and flip. There are 18 “one-sided” pentominoes. In Chapter 4 we considered the set of all possible “one-sided” tetrominoes, and continue to examine only “one-sided” polyominoes here. This is in keeping with an interest in molecular adsorption on surfaces, where molecules may preferentially adsorb in one configuration. Also, real molecules adsorbed on surfaces are generally able to change orientation, which is consistent with examining one-sided as opposed to “fixed” polyominoes.

Enumeration of polyominoes has been a longstanding research problem in their mathematical literature, as the size of the families (polyominoes of a given area  $N$ ; tetrominoes have  $N = 4$ ) grows exponentially, as quantified by Klarner’s constant [141]. A simple brute force approach is to enumerate a family of size  $N$  by generating them from the family of size  $N - 1$ . First, take a polyomino of size  $N - 1$ , add an additional lattice site at one edge site, and store the result. Repeat this process over all edge sites of every polyomino of size  $N - 1$ , and then eliminate duplicates to complete the set. The first efficient algorithm for enumeration of all possible fixed polyominoes is due to Redelmeier [140]. Redelmeier’s algorithm avoids generation of duplicates. Redelmeier was able to enumerate up to all



possible 24-site polyominoes using ten months of computer time, which was a more than tenfold increase in rate of enumeration over other algorithms available at that time.

More recent work by Conway has focused not on actual construction of every single polyomino of a given size, but instead on calculation of the properties (including number) of those families of polyominoes using transfer-matrix methods. This has resulted in calculation of polyomino properties such as perimeter, percolation thresholds, area, and number up to size 30 and beyond [118]. However, his algorithm is not useful if the properties of individual shapes are to be studied, since it does not actually generate the shapes. Conway's algorithm also applies only to fixed (not one-sided or free) polyominoes.

### 5.1.2 Tiling

Golomb was the original author of much of the mathematical literature on polyominoes, including an early study of different packings (“tiling”) of small polyominoes [10]. Golomb's book [11], *Polyominoes*, encapsulates much of the original discussion of polyominoes and challenging or classic problems regarding their tiling. For instance, how can one tile dominoes so that a “fault line” does not run through the structure? This has a direct application to masonry, as brick walls with continuous fault lines are weaker for bearing loads or shock resistance. We would also hope that a thorough understanding of polyominoes may eventually lead to a better understanding of assembly in modern chemical problems. For example, TEM micrographs of some binary nanoparticle superlattices [142] bear a strong resemblance to polyomino crystals.

Conway created a sufficient, but not necessary, set of requirements for a polyomino to be able to tile the plane. By this we mean a regular structure which covers every lattice site on an infinite plane. This rule is dubbed “Conway's criterion”, and no better rule has yet been

discovered [143]. The generalized version of the rule is for a “Conway Hexagon”, which is defined as follows:  $A, B, C, D, E, F$  are points in order on the boundary of some region. Let  $b(A, B)$  refer to the part of the boundary curve connecting points  $A$  and  $B$  without passing through any other point, and  $b(C, D)$  refer to the same curve for  $C$  and  $D$ , and similar for the rest of the adjacent points. If  $A = B$ ,  $b(A, B)$  is just a point: this may be useful for shapes without much curvature, or shapes such as pentominoes or tetrominoes. A shape satisfies “Conway’s criterion” if there is a translation that simultaneously takes  $A$  to  $E$  and  $B$  to  $D$ , and each of the four sides  $b(B, C)$ ,  $b(C, D)$ ,  $b(E, F)$ ,  $b(F, A)$  has 180 degree rotation symmetry. In practice, polygons that satisfy this criterion will have opposite sides that are congruent and parallel. This allows them to pack by stacking “top to bottom” along the congruent edges, and also “end to end” through 180 degree rotations.

## 5.2 Simulation details

### 5.2.1 Change from binary to integer representation

For this work our simulation code was modified such that occupation of the lattice was no longer stored bit-by-bit in a 512 byte integer vector (8 bytes per element). Instead, a two-dimensional integer array of two bytes per element was used to record the state of the lattice. Initially, possible reduced speed was a concern. On modern CPUs, the storage array appears to still fit within the L2 cache (up to roughly 6 megabytes in size) provided that the dimension of the array is kept to a reasonable size. Code and data stored within the L2 cache of a processor can be accessed much faster than data which has to be fetched from main memory. We typically use 256 as a maximum lattice dimension, which equates to only 128 kilobytes of cache ( $256^2$  array values at 16 bits per value), and most modern

CPUs have at least one megabyte of L2 cache. Allocatable arrays were also tested, but the resulting performance was slower by at least an order of magnitude when compiled with the GCC/gfortran, version 4.3.

### **5.2.2 Expanded lattice**

As some of the polyominoes to be studied are much larger than tetrominoes, the simulation cell size was increased. Larger lattices were needed to minimize any finite size effects. Preliminary runs included many different sizes, up to a  $512 \times 512$  lattice, but typically a  $120 \times 120$  or  $144 \times 144$  lattice is used for these simulations. An edge length of 120 has the advantage of being evenly divisible by 2,3,4,5,6 and 8, which is useful for simulations of shapes with many solid phases, or unknown crystal structure. If the simulation cell edge length is not a multiple of the unit cell edge length, grain boundaries or line defects may appear in the simulation.

### **5.2.3 Modified convergence heuristics and block averaging**

In general, simulations of larger polyominoes take much longer to equilibrate than those of smaller ones. This was expected for a few reasons. Our biased insertion method becomes less efficient as the polyominoes become larger. Translation moves, still limited to a displacement of one lattice site in any direction, are smaller relative to the size of the piece. Since the shapes are larger, there is a lower acceptance rate for all moves at high densities – with more lattice sites being affected by a move, there is simply a greater chance of a move resulting in overlap with another piece. The number of Monte Carlo moves between samples, and the number of samples per block, were therefore increased to 4000 and 16000

respectively, to reflect the increased lattice size. To equilibrate a system in the vicinity of a phase transition, several billion Monte Carlo moves, or more, were often needed. The nucleation and growth of a crystalline phase is a slow process. At a  $\beta\mu$  just barely above a transition and starting from an empty lattice or fluid, the simulation may proceed for billions of MC moves in the fluid phase before the solid phase fully occupies the cell. At  $\beta\mu$  below the transition point, the fluid phase does not need as many MC moves to equilibrate.

### 5.3 Vacancy Thermodynamics

For crystalline phases, we should be able to accurately and precisely model isotherms in the high density regime by determining the average number of vacancies present. One model used for this will be described in this section. Specific examples will be discussed in a later section.

In the grand canonical ensemble, for an athermal system:

$$\beta PV = \ln \Xi = \frac{S}{k} + \beta\mu \langle N \rangle \quad (5.1)$$

where  $\langle N \rangle$  is the average number of pieces in a system. During the course of a simulation  $\beta PV$  is maximized. Therefore, when examining crystalline solid phases or interfaces between different cluster domains, packings which have greater entropy at a given density are the more favorable.

The thermodynamic properties of crystalline phases of this model can be accurately modeled as follows. Crystalline phases are characterized by both high density and translational order. For a lattice of size  $L \times L$  and polyominoes of size  $M$ , we define  $N$  as the number

of polyominoes and  $V = L^2/M$  as the maximum number of polyominoes. The partition function can be presented as a sum over configurations, which may then be restated as a sum over occupancies by introduction of degeneracy coefficients  $W(N)$  (which are micro-canonical density-of-states):

$$\Xi = \sum_i^{states} e^{\beta\mu N_i} \quad (5.2)$$

$$= \sum_{N=0}^{\infty} W(N) e^{\beta\mu N} \quad (5.3)$$

Instead of summing over the number of pieces, we may sum over the number of voids ( $N_V = V - N$ ):

$$\Xi = e^{\beta\mu V} \sum_{N=0}^{\infty} W(N) e^{\beta\mu(N-V)} \quad (5.4)$$

$$= e^{\beta\mu V} \sum_{N_V}^{\infty} W(N_V) e^{-\beta\mu N_V} \quad (5.5)$$

The “complete occupancy” term  $e^{\beta\mu V}$  is factored off, which shows that  $-\beta\mu$  is the quantity conjugate to the number of vacancies. Then, for large  $\beta\mu$ , only the first few terms of the sum are important, and we write

$$\Xi/e^{\beta\mu V} = 1 + W(1)e^{\beta\mu} + W(2)e^{-2\beta\mu} + \dots \quad (5.6)$$

The specific degeneracy expressions are as follows, with  $W_1$  representing the “local” states at any  $V$  sites, and  $W_2$  being an interaction term which is defined in its expression, similar to the definition of a virial coefficient.

In this equation,  $W(N_V)$  is the total number of ways to arrange all the pieces in the system when  $N_V$  of them is missing. Because of the translational symmetry, we can factor off a volume term, giving

$$W(1) = V \cdot W_1 \quad (5.7)$$

where  $W_1$  is a “local” degeneracy – the number of states associated with a single vacancy at a specific position.  $W(2)$  is the total number of states for a system missing two shapes. These can be divided into two groups: those where the two missing pieces are far enough from each other that they can be considered independent, and those where they interact:

$$W(2) = \frac{V(V-1)}{2} \cdot W_1^2 + V \cdot W_2 \quad (5.8)$$

The first term covers the “non-interacting” situation, by treating the vacancies as a non-interacting “ideal gas”:  $V(V-1)/2$  is the number of ways of placing two vacancies on the lattice, and they each give rise to  $W_1$  local states. The other term covers the “interaction” of the two vacancies. This equation may be regarded as a *definition* of the  $W_2$  quantity, which should be thought of as a second virial coefficient of the vacancies.

For two different crystal structures,  $A$  and  $B$ , a larger  $W_1$  should lead to a larger  $\beta PV$  and therefore determine the thermodynamically stable phase. If  $W_1(A) = W_1(B)$ , a comparison would have to be made between  $W_2(A)$  and  $W_2(B)$ , and so on. This second order effect on

the partition function (and hence, packing fraction as commonly compared in isotherms) is small compared to first order effects. The average vacancy density for a given crystal can be determined by examining the derivative of the log of the partition function with respect to  $-\beta\mu$ :

$$\langle N_V \rangle = \frac{\partial \ln \Xi}{\partial(-\beta\mu)} = \frac{\partial}{\partial(-\beta\mu)} \ln[1 + V \cdot W_1 \exp^{\beta\mu} + \dots] \quad (5.9)$$

$$\approx \frac{\partial}{\partial(-\beta\mu)} V \cdot W_1 e^{\beta\mu} \quad (5.10)$$

$$\approx V \cdot W_1 e^{\beta\mu} \quad (5.11)$$

Finally, we note that this theory may also be applied to crystals with multiple “kinds” of sites, say  $X$  and  $Y$ . To first order,

$$W(1) = V_X \cdot W_{1X} + V_Y \cdot W_{1Y} \quad (5.12)$$

where  $V_X$  is the number of sites of type  $X$ ,  $W_{1X}$  is their associated local degeneracy, and similarly for site type  $Y$ .

## 5.4 Pentomino results

### 5.4.1 Overview

The phase behavior of each of the 18 one-sided pentominoes was studied in detail. The shapes themselves are shown in Figure 5.1. There are five pairs of enantiomers, and several of the shapes can be seen as larger versions of tetrominoes. While there is a rod in this set, there is not a square. The *X* shape has the same symmetry as the square, but its different shape may result in different packing. As each pentomino may be constructed by adding a single site to one or more tetrominoes, the other shapes also contain features of the tetrominoes, such as the pentomino *T* shape resembling both the tetromino *T* shape and *J/L* shapes. Like the tetrominoes, all of the pentominoes can tile the plane.

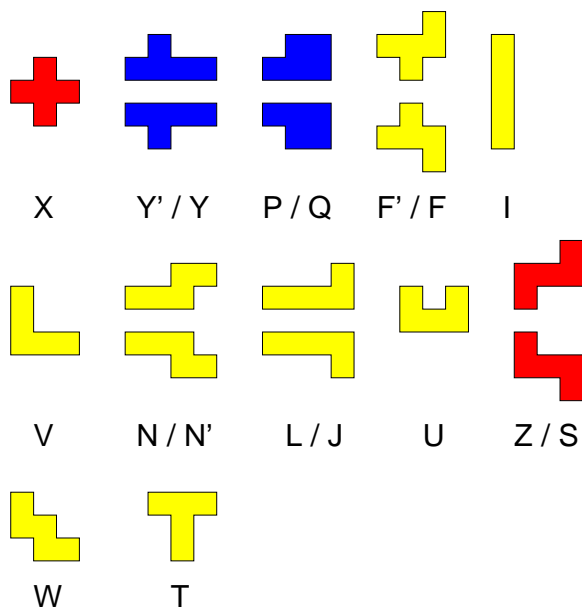


Figure 5.1: The 18 one-sided pentominoes. Some enantiomeric pairs are labeled with a single letter, “primed” and “unprimed”. Colors indicate the presence, absence, and type of phase transition. Yellow indicates no phase transition, blue indicates transition to a disordered phase, and red indicates transition to a crystalline phase or phases.



For each pentomino, five independent isotherm simulations were performed in the range  $\beta\mu = 1$  to  $\beta\mu = 11$ . A spacing of  $0.05 \beta\mu$  between state points was used. While the initial simulations began from an empty lattice, simulations at other state points were seeded from the prior state point. This “sequential” simulation protocol greatly accelerates equilibration at high densities. It also allows us to obtain forward and reverse branches of isotherms. The sequential simulation protocol restricts us from parallelizing a single isotherm calculation. To make full use of computing resources, we performed multiple isotherm calculations in parallel using different random number generator seeds, or on entirely different species.

### 5.4.2 Pentominoes without a phase transition

The rods,  $T$ ,  $N/N'$ ,  $W$ ,  $L/J$ ,  $V$ ,  $F/F'$  and  $U$  pentominoes did not undergo a phase transition in the  $\beta\mu$  range studied. The isotherms for these shapes are shown in Figure 5.2. As in the isotherms shown in the previous chapter, our unified temperature and chemical potential,  $\beta\mu$ , is on the horizontal axis. The packing fraction ( $\eta$ , as defined in the previous chapter), is on the vertical axis.

While not displaying phase transitions, these systems nonetheless have many interesting features. Snapshots of these fluids at high densities are shown in Figures 5.3 and 5.4. In the  $T$  fluid, the predominant structure involves two pieces placed “back to back”. An example of  $T$  shape packing is shown in Figure 5.3. The “back to back” dimer forms a vacancy-free interface (there are no unoccupied lattice sites) with itself when rotated 90 degrees. In the snapshot, we see that vacancies are often associated with pieces not being part of “back to back” dimers. The capability of differently oriented clusters to accommodate each other through vacancy-free interfaces is observed in many pentomino fluids, and especially those which do not undergo phase transitions. This ability to display orientational disorder

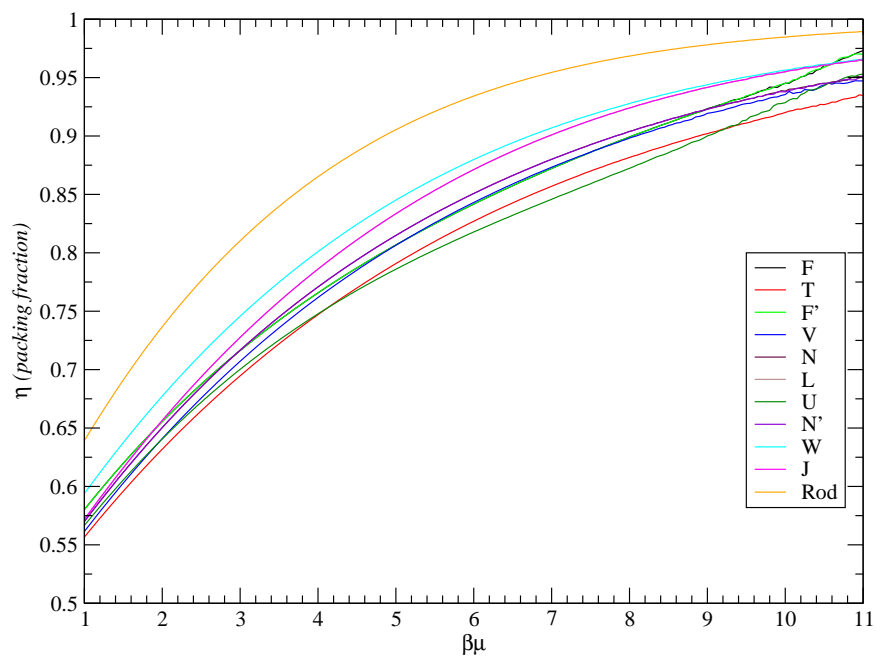


Figure 5.2: Isotherms of pentominoes without a phase transition. Data for each isotherm was gathered via “sequentially” seeded simulations. Each state point in an isotherm is separated by  $0.05 \beta\mu$ .

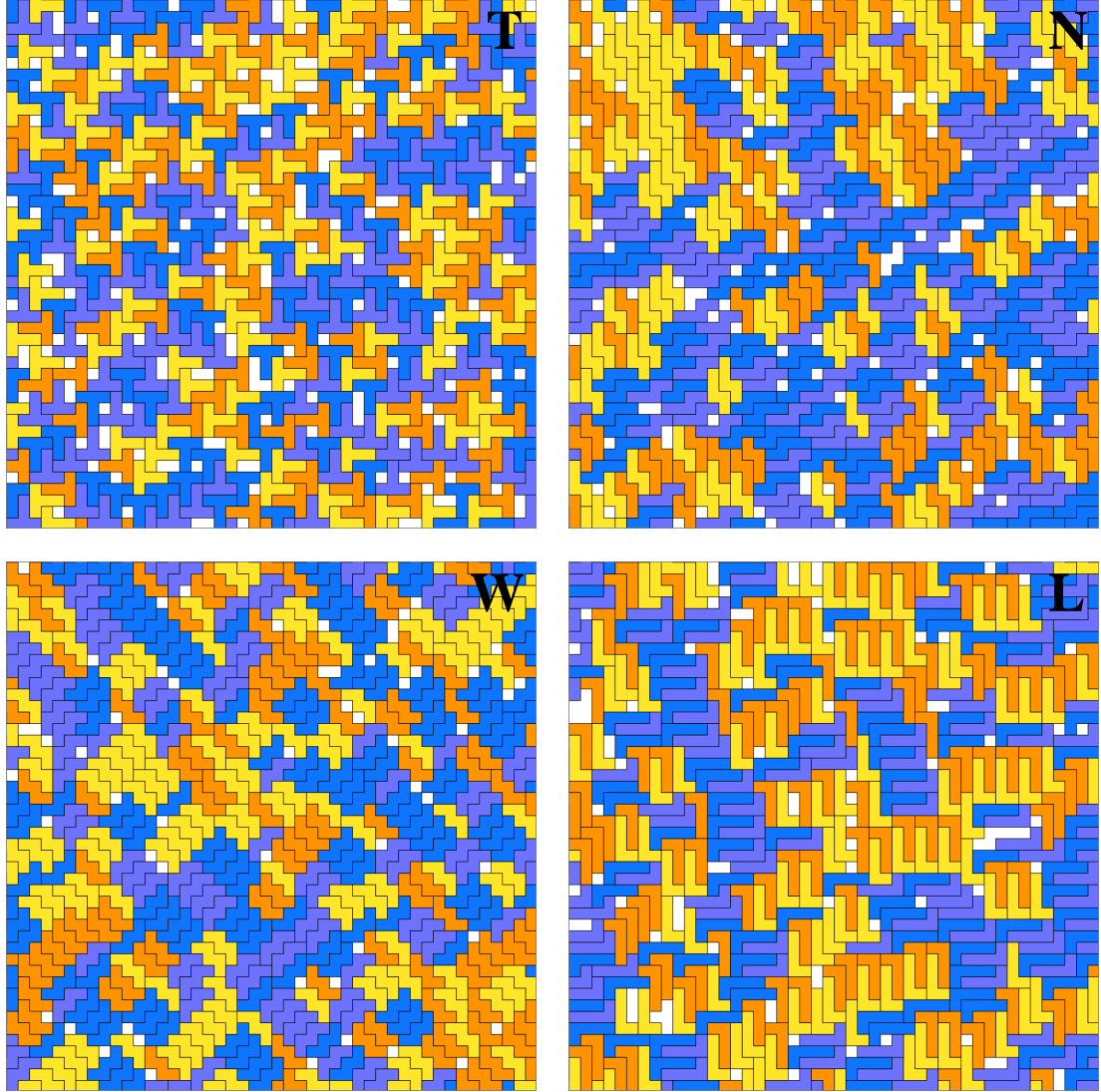


Figure 5.3: Pentominoes that do not display phase transitions, each at  $\beta\mu = 11$ . In this and other snapshots, pieces are shaded differently according to orientation. The blue and purple shades differ in rotation by 180 degrees, as do the yellow and orange shades. Each snapshot shows a section of the full simulation cell. From top left to bottom right (reading order):  $T$ ,  $N$ ,  $W$ ,  $L$ .

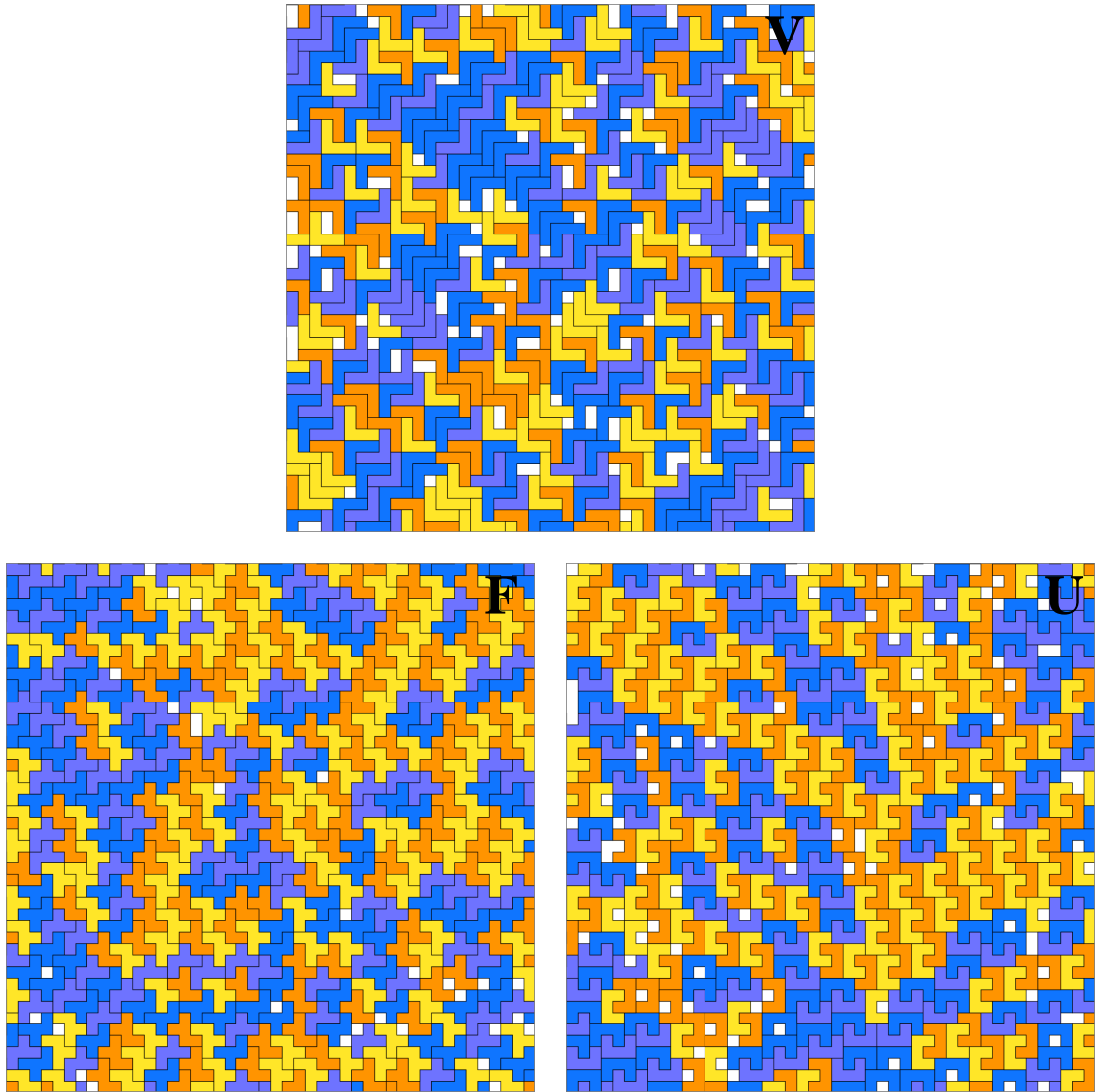


Figure 5.4: Additional pentominoes that do not display phase transitions, all at  $\beta\mu = 11$ . Each snapshot shows a section of the full simulation cell. From top left to bottom right (reading order):  $V$ ,  $F$ ,  $U$ .

without loss of packing fraction appears to inhibit crystallization. That is, the large number of non-crystalline high density states this orientational freedom provides make it less likely that a crystalline state will be the final result at any given  $\beta\mu$ .

Diagonal stacking, as seen in the *S* and *Z* tetrominoes in Figures 4.5, is also observed in many pentominoes. The *N* shape shown in Figure 5.3 is one example. This is not surprising as the *N* shape resembles the *S* shape tetromino. Similar to the *S/Z* tetrominoes, the *N* can form a herringbone interface between clusters of perpendicular orientation. We see large “stacked” domains, but no phase transition to an orientationally ordered crystal.

The *W* shape also displays strong orientational clustering, and features vacancy-free interfaces between clusters of different orientation. Due to the diagonal edges of the *W* shape, a perpendicular piece will always fit flush against a stack of *W* pieces. Interestingly, the packing and clustering observed in the *W* simulations is similar to that of the tetromino and pentomino rods, but rotated by 45 degrees. The *W* shape also has quite high density over most of the chemical potential range scanned, second only to that of the rod shape.

In the *L* fluid, pairs of pieces aggregate to form  $2 \times 5$  rectangular dimers, analogous to the dimers seen in the tetromino *L* fluid. When a *L* piece is not part of a dimer, quite often there are multiple vacancies next to it. As  $\beta\mu$  is increased and more dimers form, the density of *L* fluids approaches that of *W* fluids, which have nearly equal packing fraction at  $\beta\mu = 11$ .

The *V* fluid, shown in Figure 5.4, displays multiple types of clusters. Ultimately, they pack only poorly and at  $\beta\mu = 11$ , *V* fluids have an average density lower than any system but *T* fluids. The two main clusters observed are either “head-to-tail” dimers, or diagonal stacks of pieces of the same orientation. However, these two types of clusters cannot form defect-free interfaces. Four pieces, each with a different orientation, may form a cluster shaped

like a “cross” or “plus sign”, which will feature prominently in discussion of the  $Z$  shape. However, this cluster does not frequently occur in the  $V$  fluid.

The  $F$  shape displays orientational clustering at high  $\beta\mu$ . Two types of dimers are observed and large orientationally oriented domains are formed. At high  $\beta\mu$ , the density of this fluid increases faster than that of other pentominoes which do not undergo transitions, except for the  $U$  shape. The interlocking diagonal dimer tiling with a  $2 \times 1$  edge, easily visible in the upper right of the snapshot, is the dominant structure observed. Clusters of head-to-tail dimers are seen in the lower middle region.

This strong orientational clustering was also seen in shapes which had phase transitions to a disordered state (and will be discussed in those cases shortly). It is not entirely clear why the  $F$  shape has domains which look largely analogous to the  $Y$  shape, but has an anomalous isotherm instead of its own phase transition. No cell-sized grain boundaries were found and testing of various system sizes did not show significantly different packing. It is possible that a larger variety of domain interfaces simply leads to more possible defect states, and the rotational and translational entropy gained through these states is enough such that a transition never occurs.

The  $U$  shape can only form high-density configurations through “interlocked” dimers. These dimers may form diagonally stacked clusters with either  $2 \times 1$  or  $2 \times 2$  interfaces, either of which may form a vacancy-free interface with a perpendicularly oriented cluster. A snapshot is shown in Figure 5.4. Where there are vacancies in this snapshot, there is usually a  $U$  piece nearby that is not part of a dimer. The anomalous high density behavior for  $F$  and  $U$  shapes may be because they act as “larger” dimerized shapes more strongly than, for example, the  $J/L$  shapes.

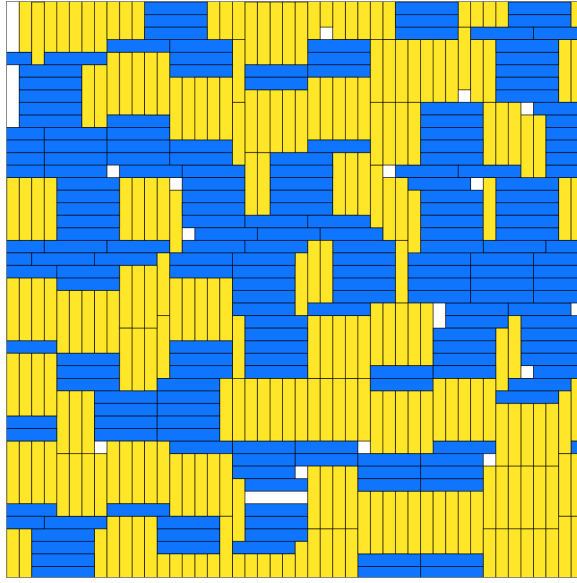


Figure 5.5: Pentomino rods at  $\beta\mu = 11$ . Orientation-specific clustering of groups of rods into larger rectangular (often square-like) shapes is the dominant form of packing.

Lastly, the previously studied system of rods on a square lattice with an aspect ratio of 5:1 [132] is reproduced here. The rods cluster strongly and have the highest density at any given  $\beta\mu$  of the species which do not have a phase transition. A snapshot of this system is shown in Figure 5.5, and is very similar to the tetromino rods in the previous chapter.

### 5.4.3 Isotherms of pentominoes with phase transitions

The  $X$ ,  $S/Z$ ,  $Y/Y'$ , and  $P/Q$  pentominoes undergo phase transitions, as indicated by sharp discontinuities in their isotherms, which are shown in Figure 5.6. As already mentioned, the data in this figure are averages of five independent runs, using different random seeds. In some cases, the transitions were not always observed at the same  $\beta\mu$  (that is, there was hysteresis). This results in jagged steps in the average isotherm; the individual isotherms

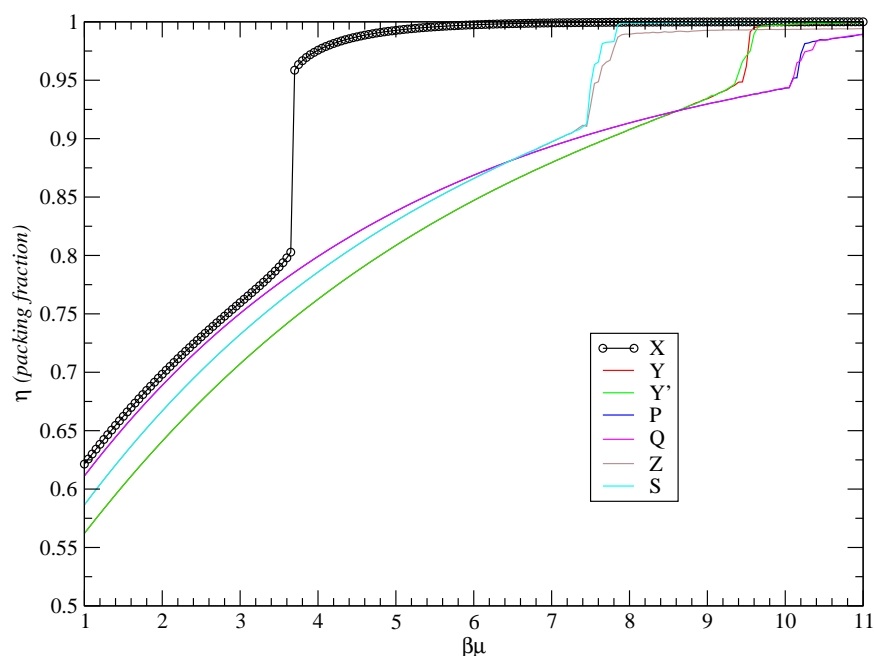


Figure 5.6: Isotherms of pentominoes that display phase transitions (data averaged over 5 runs). State points in each isotherm are separated by  $0.05 \beta\mu$ ; individual points are shown only for the  $X$  data. Differences between enantiomers appear due to small sample size.

each display a single steep step (not shown). The  $S$ ,  $Y'$ , and  $Q$  shapes are mirror images of the  $Z$ ,  $Y$ , and  $P$  pentominoes, so need not be discussed.

Briefly, the  $X$  shape freezes to a single crystal structure. The  $Z$  and  $Y$  shapes undergo transitions to disordered structures; in the case of the  $Y$  shape the density of this phase approaches nearly  $\eta = 1$ , while the dense  $P$  phase has rather more vacancies. The  $Z$  shape also crystallizes, but to many different polymorphs.

#### 5.4.4 $Y$ and $P$ shapes: transition to a disordered phase

Both just below and above the phase transition the  $Y$  fluid consists of “back to back” dimers. This is shown in Figure 5.7. The high density phase has a packing fraction very near to



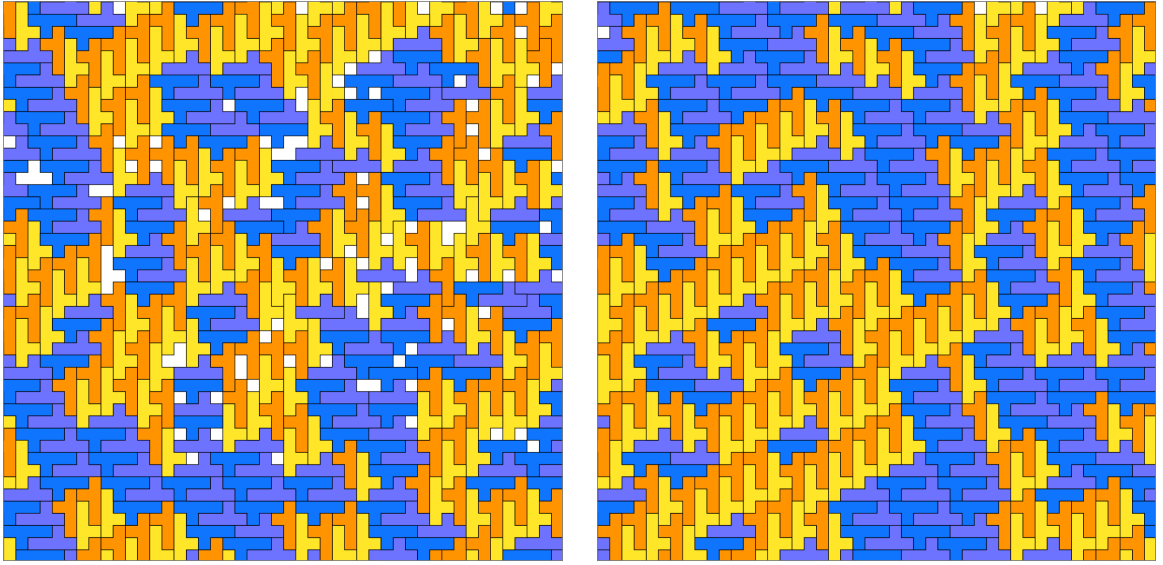


Figure 5.7:  $Y$  pentomino snapshots at  $\beta\mu = 9.50$  and  $\beta\mu = 11.00$  (pre- and post-transition).

1.00, comparable with that of a perfect crystalline structure. We speculate that orientational disorder as observed in Figure 5.7 is the source of some additional entropy which inhibits true crystallization.

The phase transitions observed for the  $P$  shape did not result in systems with unit density or ordered, crystalline domains. An example result is shown in Figure 5.8. Pre-transition,  $P$  pieces often dimerize “face to face” and form  $5 \times 2$  rectangles, but post-transition this dimer form is not observed. A diagonally “stacked” dimerization or clustering is seen both pre- and post-transition. To test whether this disordered, irregular packing was a function of periodic boundaries, lattice sizes of  $120^2$ ,  $180^2$  and  $210^2$  were tested, all of which produced similar results.

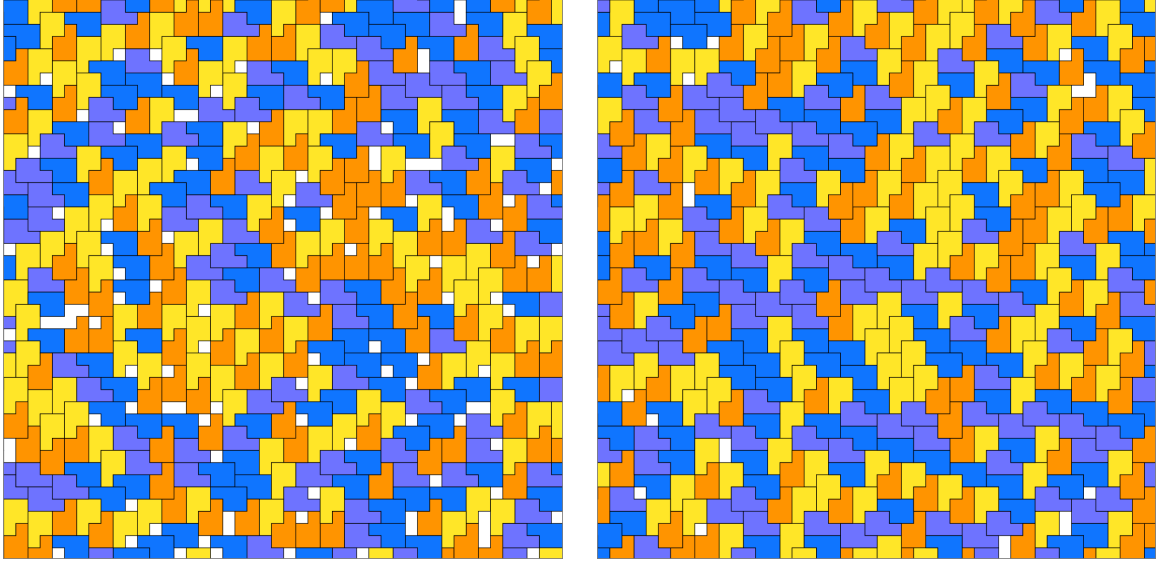


Figure 5.8:  $P$  fluid, at  $\beta\mu = 10.15$  and  $\beta\mu = 11.00$  (pre- and post-transition).

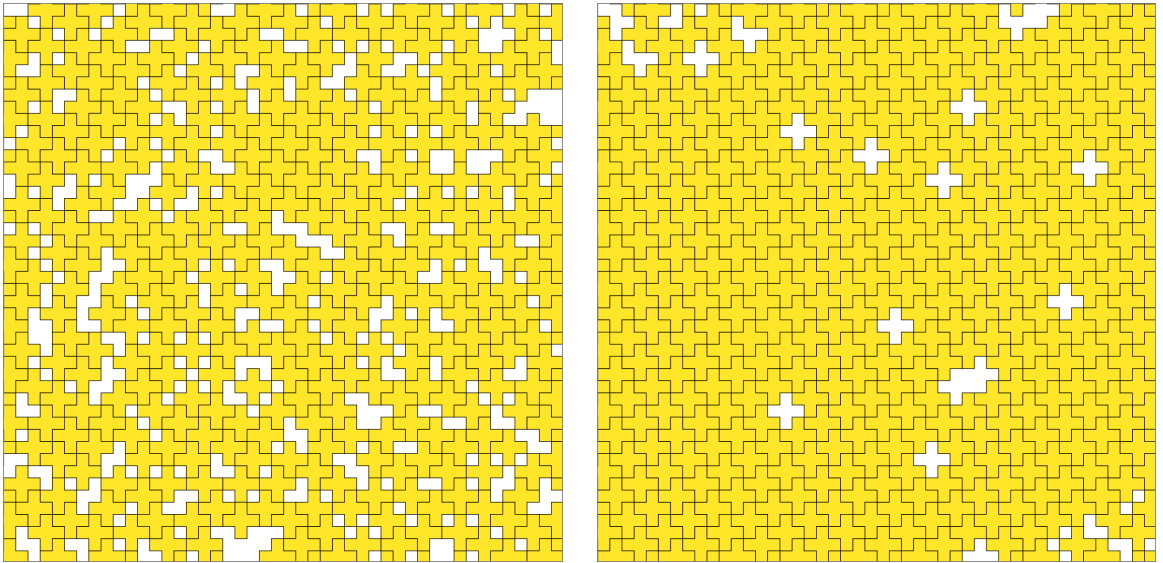


Figure 5.9:  $X$  pentomino snapshots: before transition at  $\beta\mu = 3.650$  and after transition at  $\beta\mu = 3.70$ .

### 5.4.5 *X* shape: transition to an ordered crystal

The *X* shape undergoes a first-order phase transition to a crystalline state, and was the first shape studied to do so. Inspection of snapshots from state points before and after this transition show that the system has gone from a disordered, liquid-like state to a highly ordered, largely crystalline state. In Figure 5.9 we see the the system before and after the transition. Notably, the crystal has two possible stereoisomers: a left-handed packing and a right-handed packing. At  $\beta\mu$  just above the transition point, the resulting solid has many vacancies and several defects. It is also a pure stereoisomer instead of some kind of racemic mixture with interfaces. If it were a mixture, that would indicate either problems with equilibration or periodic boundaries and the dimensions of the crystal unit cell.

Additional isotherms in both increasing and decreasing  $\beta\mu$  for the *X* shape are given in Figure 5.10. These display hysteresis. Hysteresis may occur when a system has two states of distinctly different structure and a barrier to interconversion. The phenomenon is commonly observed in experiment, for example, with melting or freezing. For these calculations we slightly altered the simulation methodology. Each branch (forward and reverse) was simulated using “sequential” seeding as described previously. We also re-ran the calculations in a smaller system with  $L = 60$ . Here, no hysteresis loop is observed, but the transition does occur at near the same chemical potential.

### 5.4.6 *Z* shape: phase transitions and polymorphism

There are six known periodic tilings of the *Z* shape [144], shown in Figure 5.11. In the type 1 and type 4 crystals, each piece has the same orientation. They differ by being stacked “body-to-body” versus “head-to-tail”. The type 2 and type 5 crystals also have common

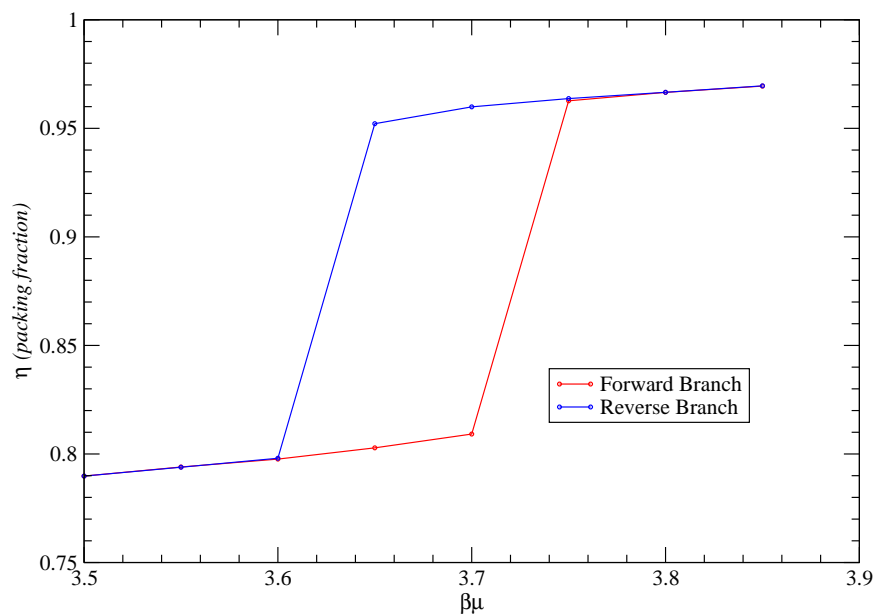


Figure 5.10:  $X$  pentomino isotherms, including both the forward and reverse branches. Significant hysteresis occurs in this system.

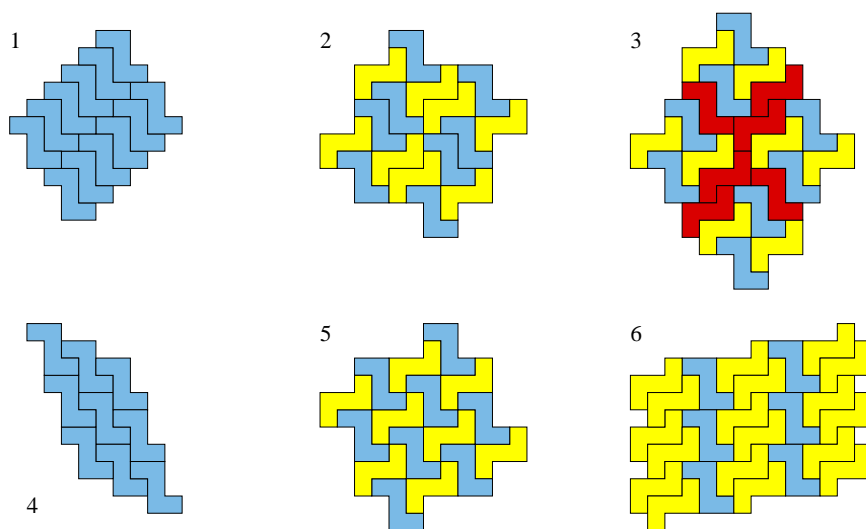


Figure 5.11: The six periodic tilings of the  $Z$  pentomino. These are found through backtracking (a form of exhaustive enumeration for tilings), not simulation. These unit cell size on the underlying square lattice widely varies for these tilings.

features. Each may be viewed as inter-meshed rows of pieces, or as an assembly of “cross” subunits composed of four pieces. When viewed as inter-meshed rows, the repeat units differ in being composed of rows single units (type 5) versus rows of dimers (type 2). When viewed as assemblies of “cross” subunits, they differ in handedness. In the type 6 tiling, vertical columns of pieces in one orientation are separated by a columns of dimers in the perpendicular orientation. Lastly, in the type 3 tiling, groups of four pieces form cross-shaped subunits which are separated by additional pieces of varying orientations, colored red. This is the most complex tiling.

When initial simulations were performed on the Z shape, we observed that post-transition configurations at high  $\beta\mu$  often had multiple domains, and that different simulation runs could also result in different crystal structures. A series of representative configurations are shown in Figures 5.13 through 5.16. Figure 5.13 shows a pre-transition configuration, displaying nuclei of type 1 and type 3, and a small number of type 2 nuclei. Its post-transition counterpart, Figure 5.14, is composed of two large domains, one of type 2 and one of type 3, with the type 2 domain occupying roughly 80% of the simulation cell. Figure 5.15 is an example of a cell with type 1 and type 2 domains, where the type 1 domain occupies about 40% of the box. The “band” feature is observed in many simulations, and apparently presents a difficult obstacle to equilibration. Lastly, Figure 5.16 displays a mixture of three similarly sized domains of type 1 and type 3 crystal, with two of the type 1 domains being of different orientation. There is also a small type 2 domain. The system in Figure 5.16 was grown from an empty lattice in a procedure described below; the systems in Figures 5.13 to 5.15 were selected from preliminary “sequentially seeded” isotherm calculations.

To better understand Z shape polymorphism, the following protocol was used: 160 independently seeded simulations were run at  $\beta\mu = 8.0$ , each starting from an empty lattice and a different random number generator seed, were run for over 1.1 trillion Monte Carlo

	Crystalline domain occurrence:					
	Type 1	Type 2	Type 3	Type 4	Type 5	Type 6
Pure crystal	4	67	3	0	0	0
Complete coverage, multiple domains	0	17	1	0	0	0
Majority component	13	48	8	0	0	0
Equal part in 2-component system	5	9	8	0	0	0
Minority in 2-component system	15	10	11	0	0	0
Equal part in 3-component system	11	15	15	0	0	0
Minority part in 3-component system	7	7	14	2	0	0

Table 5.1: Distribution of dense phase compositions for  $Z$  pentominoes at  $\beta\mu = 8.0$ , past the phase transition point. This data was gathered through simulations lasting over 1.1 trillion Monte Carlo moves for each system, beginning from an empty lattice in each case.

moves with occasional checkpointing to observe the state of the system. The final state in each run was characterized “by eye”, as either a single crystal, or a multi-domain structure, and the various phases present determined. These results are collected in Table 5.1. The majority of simulations resulted in a multi-domain configuration, indicating that even after one trillion MC moves the system is not fully equilibrated. The type 2 structure was the most commonly observed. It occurred as a pure crystal – a single domain filling the entire simulation cell – 67 times, and additional 17 times as the only type of crystal in the system (but in multiple domains). This means it is the only observed structure in over half the simulations, and in 48 of the remaining 76 simulations it is the majority component. The type 1 and type 3 crystals occur with similar frequency, but the type 3 is less likely to be the majority component. The type 4 crystal was rarely observed, and then typically only at the interface of two different crystal domains. Type 5 and type 6 structures of domains at least several repeat units in size were not observed, although clusters can sometimes be found at interfaces between domains of other types, and small nuclei are seen in configurations in lower  $\beta\mu$  simulations.

The frequency of occurrence of the different crystal structures does not correspond to the predicted order based upon single-defect vacancy models. Of the six tilings in Figure 5.11,

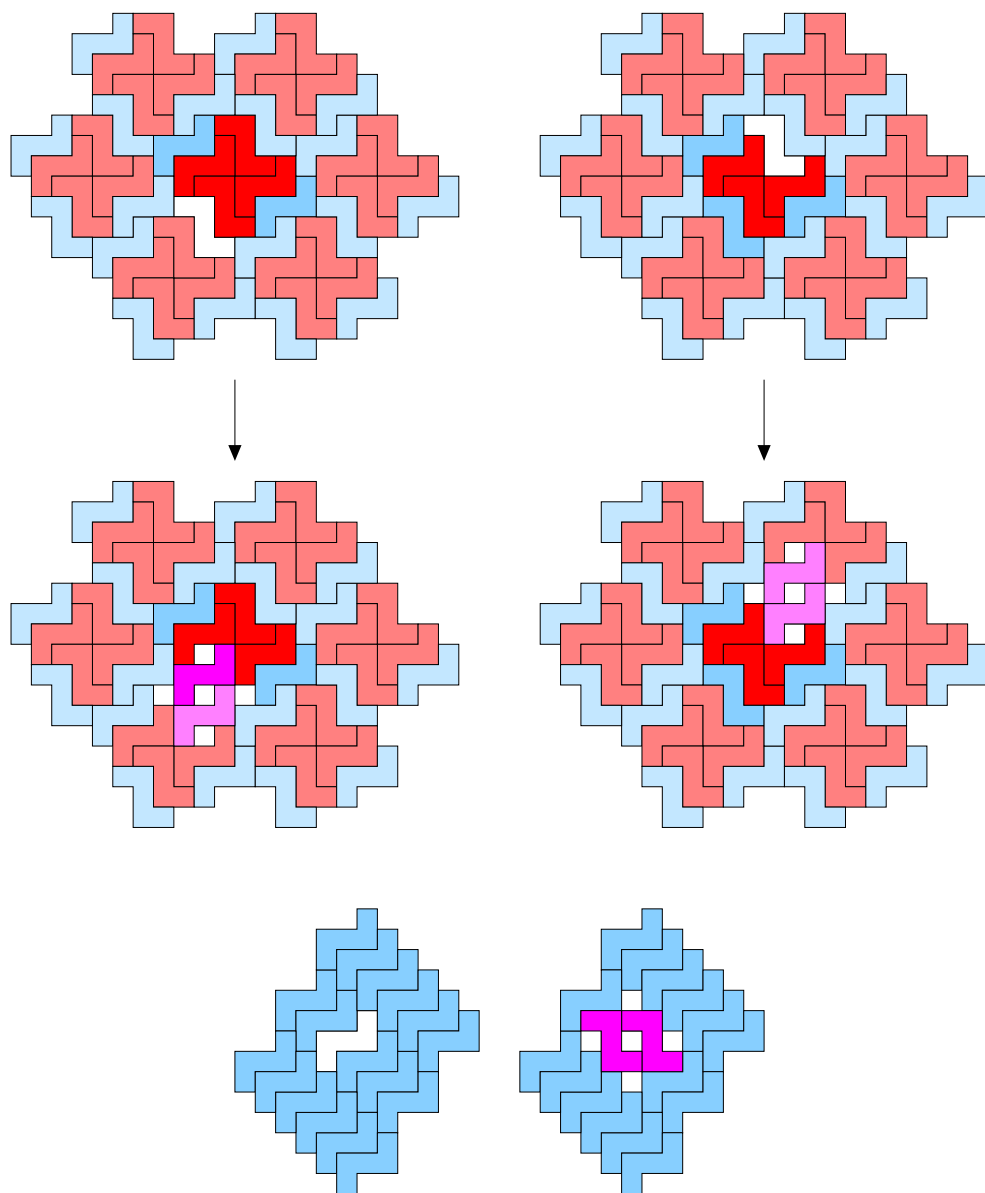


Figure 5.12: Doubly-degenerate vacancies in type 3 and type 1 Z polyomino crystals. These are the only Z polymorphs with multiply-degenerate states created upon formation of a single vacancy.

four have only singly-degenerate single-vacancy states; that is,  $W_1 = 1$  at all lattice sites (see Equation 5.7). In the types 1 and 3 crystals, there is a particular “double-rotation” possible which gives  $W_1 = 2$  at certain sites, raising the entropy of the crystals. If the polymorph appearance frequencies were controlled by thermodynamics, then the type 3 crystal would be most frequently observed. It has multiple doubly degenerate single vacancy states, shown in Figure 5.12. Instead, the type 2 crystal is clearly favored. In the type 2 crystal, single vacancies result in no additional states. Interestingly, of the two crystals which only contain pieces in a single orientation, just one is observed regularly. In that case, the polymorph with greater entropy does predominate. Overall, it appears that the frequency of appearance of the different polymorphs depends more on kinetic effects (nucleation and growth rates) than on thermodynamic stability.



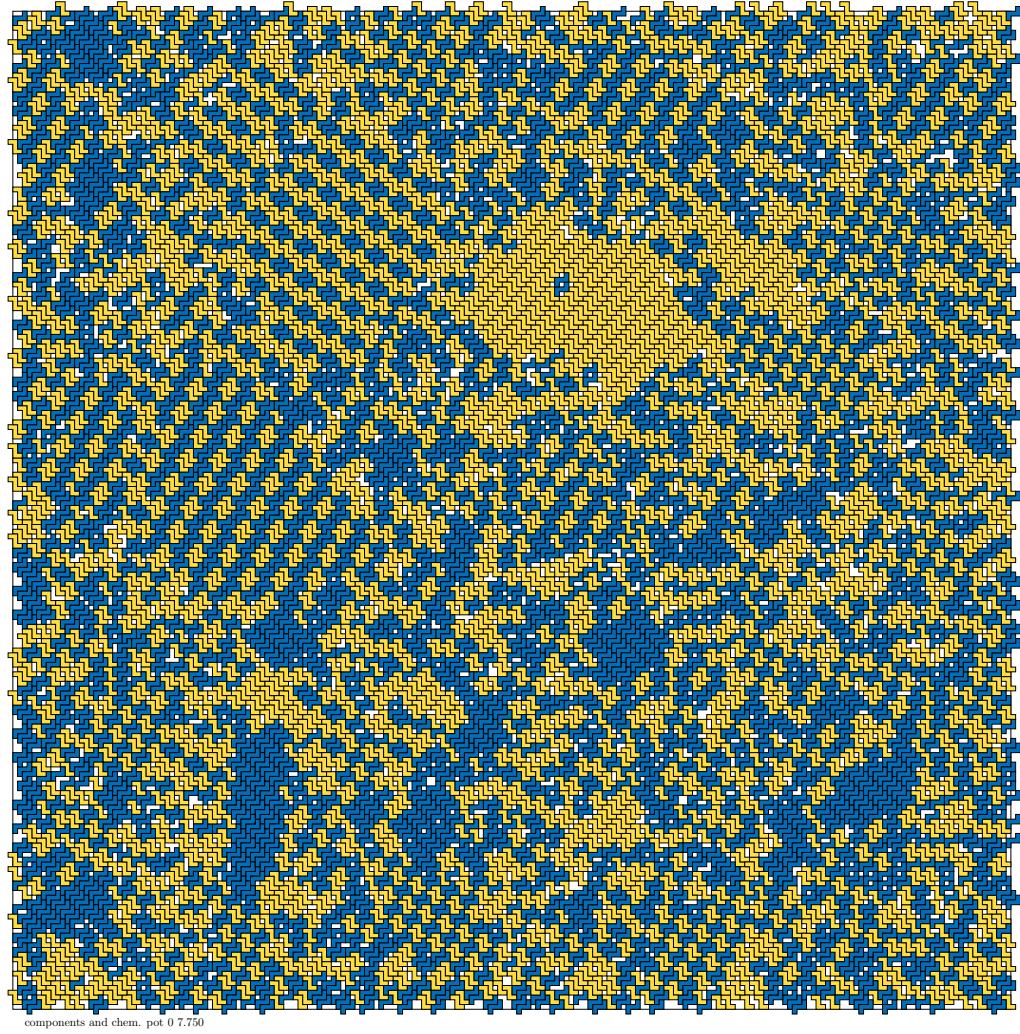


Figure 5.13: Pre-transition snapshot of  $Z$  fluid at  $\beta\mu = 7.75$ . Note the presence of many different crystalline nuclei of varying shape, structure and orientation.

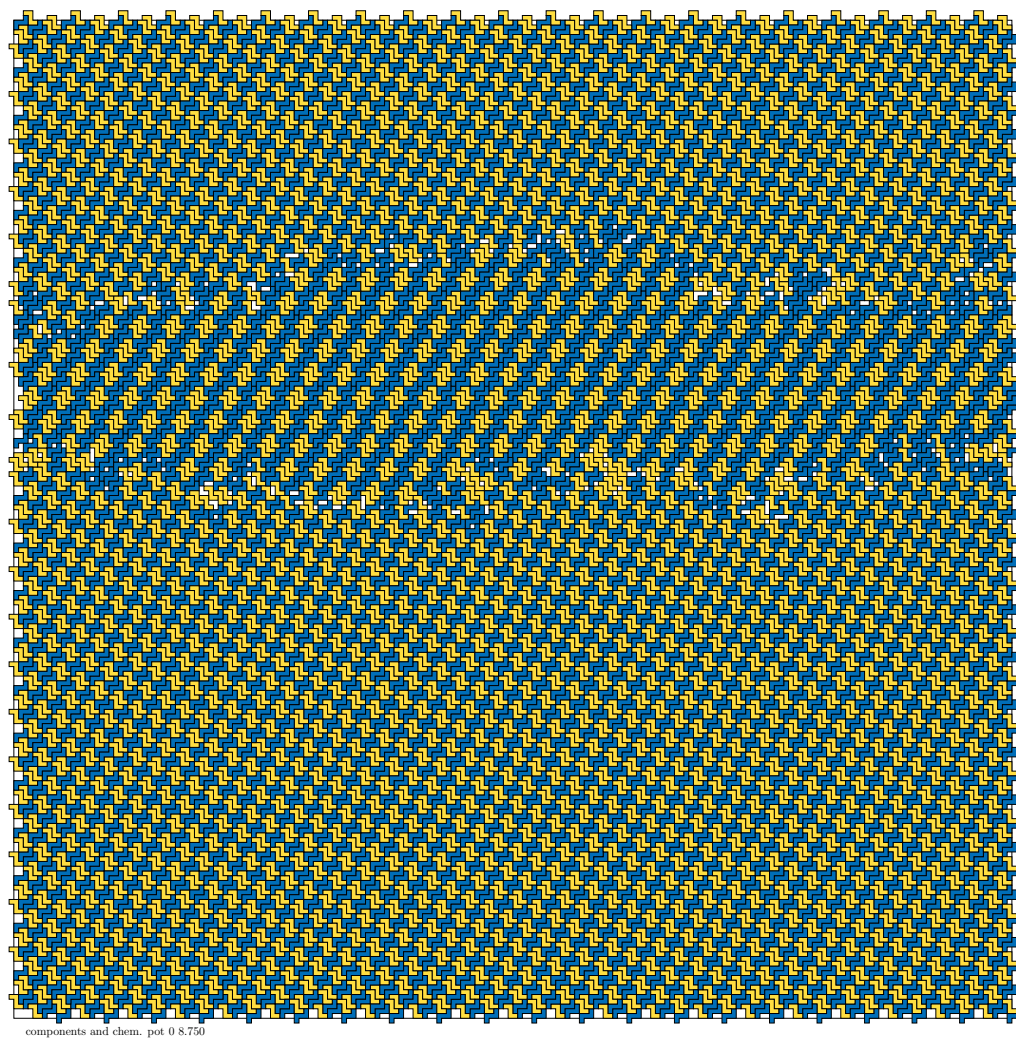


Figure 5.14: Post-transition snapshot of  $Z$  at  $\beta\mu = 8.75$ . This configuration is dominated by a large domain of type 2 crystal, and a smaller domain of type 3 crystal.

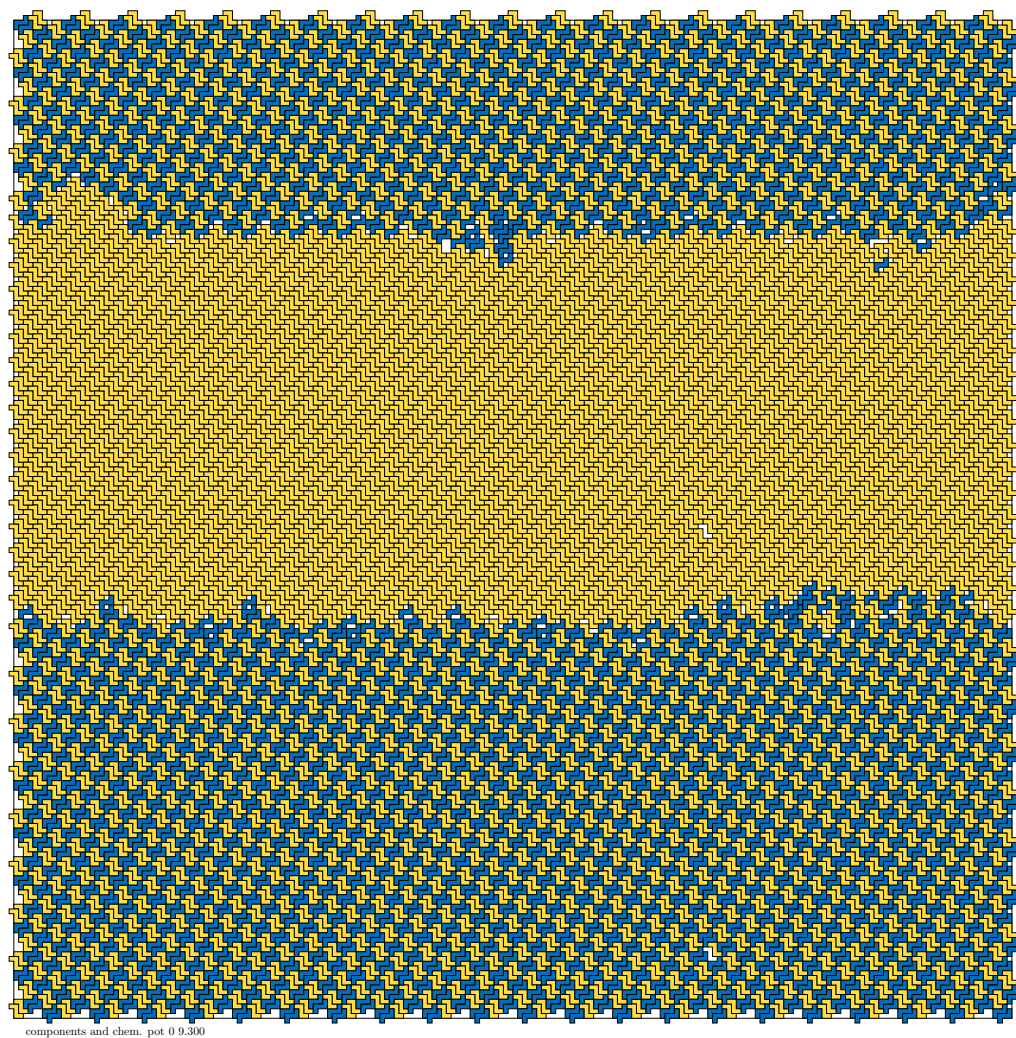


Figure 5.15: Post-transition snapshot of  $Z$  at  $\beta\mu = 9.30$  with domains of type 2 crystal and type 1 crystal.

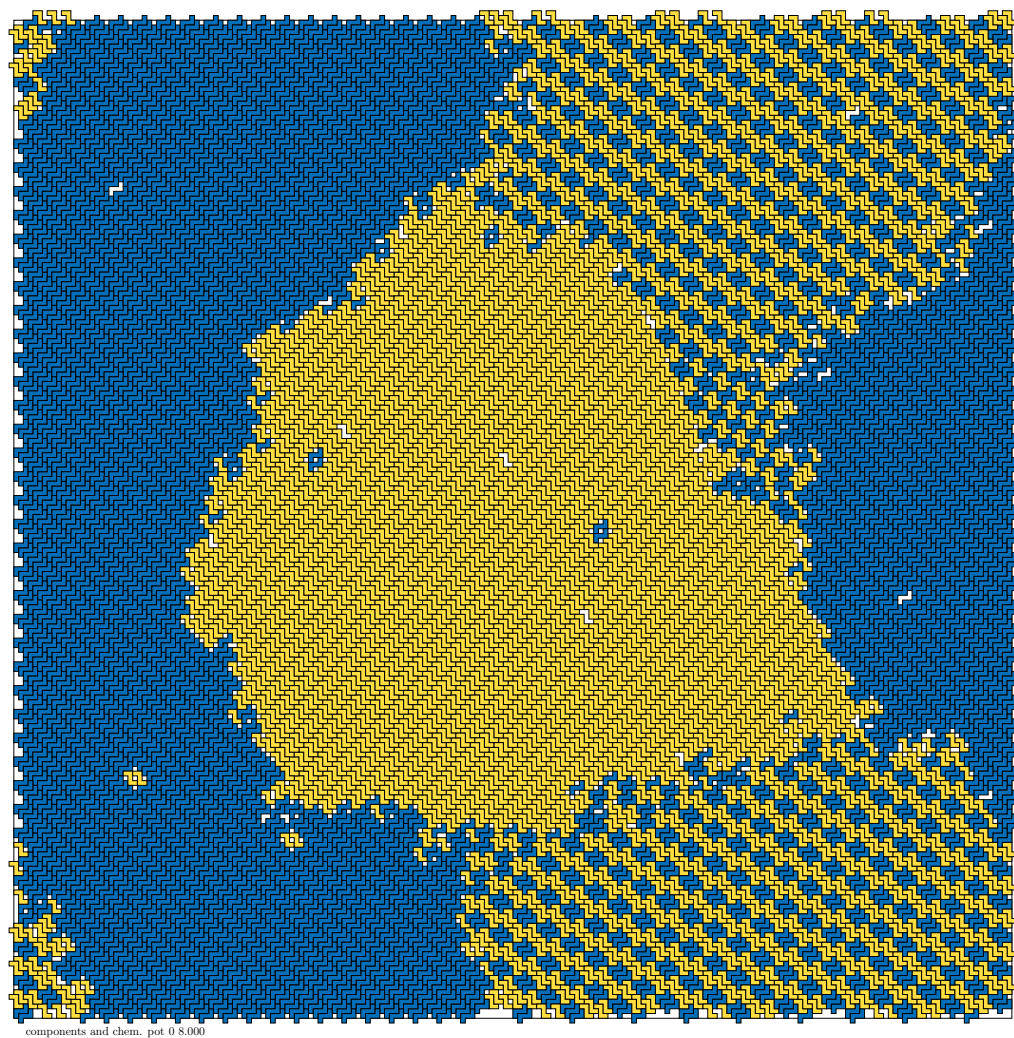


Figure 5.16: A system at  $\beta\mu = 8.0$  with two type 1 crystal domains of different orientation and a domain of type 3 crystal.

## 5.5 Columnar behavior

In the square tetromino fluid, configurations were often ordered into columns in which translations were only possible in one direction. In this section we describe further studies of this and larger shapes, in which this type of behavior is accentuated, giving rise to true phase transitions.

### 5.5.1 Theory

At very high densities the number of vacancies is very small, and a crystal can be modeled as an “ideal gas of vacancies.” The entropy, according to this approach, is:

$$-S/k_B L^2 = (1 - \eta) \ln(1 - \eta) + \eta \ln \eta$$

Note that this is the same form for the entropy as for generalized particles which follow Fermi-Dirac statistics.

A truly columnar phase should be exactly equivalent to a one-dimensional system, and therefore should be exactly solvable. For instance, for  $n$  blocks of length  $m$  placed on an  $L$ -site 1D lattice, Lee and Yang have shown the number of states to be [145]:

$$W(n) = \binom{L - mn + n}{n}$$

which leads to the entropy of the system (in the thermodynamic limit,  $L \rightarrow \infty$ ):

$$S/k_B = \ln W(n)$$

$$\begin{aligned}
-S/k_B L^2 &= (1 - \eta + \eta/m) \ln(1 - \eta + \eta/m) \\
&\quad - (1 - \eta) \ln(1 - \eta) + (\eta/m) \ln(\eta/m)
\end{aligned}$$

In the case of a system with periodic boundaries, additional states are available as pieces may occupy sites near the boundary which may be excluded for a system that has hard walls. This leads to:

$$W(n) = \frac{L}{n} \binom{L - mn + n - 1}{n - 1}$$

Work presented below involving squares will show that some polyomino systems display true columnar behavior, as they are accurately modeled by using the exact enumeration model with periodic boundary conditions.

### 5.5.2 Squares

In addition to the tetromino *O* ( $2 \times 2$  squares), we also obtained isotherms of the  $3 \times 3$  and  $4 \times 4$  square square polyominoes. Both shapes displayed columnar behavior at high density. In addition, the  $4 \times 4$  system displayed hysteresis.

The  $3 \times 3$  square does not exhibit a first-order phase transition. The corresponding isotherm is shown in Figure 5.17. In the range  $\beta\mu = 5.3$  to  $5.5$  a smooth transition from an isotropic liquid to a columnar state occurs. The columnar ordering is not perfect: at  $\beta\mu = 5.95$ , the system has multiple small defects in the columnar ordering. This is shown in Figure 5.18. However, the change from lower chemical potentials is marked enough to be given as the cause for the increase in packing fraction. Before this change in curvature of the isotherm, there was essentially no ordering in the system. The snapshot taken at  $\beta\mu = 5.95$  shows

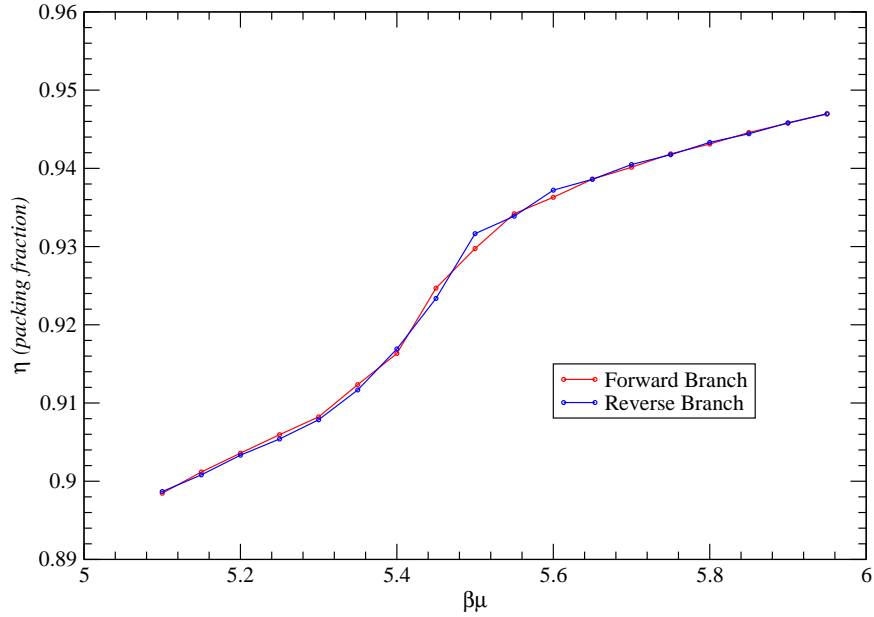


Figure 5.17: Isotherm of  $3 \times 3$  squares. This data was collected using the same protocol as the isotherm data for  $X$  shapes, with the reverse branch seeded from a perfect crystal.

columnar ordering with only occasional defects. The entropy versus packing fraction for this system is plotted in Figure 5.19. At low  $\beta\mu$ , there is large disagreement between varying theories and simulation. This is because the system is in a disordered, low density fluid phase. At higher  $\beta\mu$ , simulation and the exact enumeration match nearly exactly, supporting identification of this as a true columnar phase.

The isotherms for  $4 \times 4$  squares are shown in Figure 5.20. The discontinuous jump in packing fraction and presence of hysteresis (between  $\beta\mu = 6.4$  and  $6.5$ ) supports identification of the transition as first-order. A snapshot of this system above the transition is shown in Figure 5.21 – almost no out-of-column defects are observed. When a vacancy occurs in the  $4 \times 4$  system, more entropy is gained in comparison to a vacancy in a  $3 \times 3$  system. A single vacancy allows translational freedom for up to 4 additional pieces. This may explain why the  $4 \times 4$  system has a true first-order transition, but smaller square systems do not.



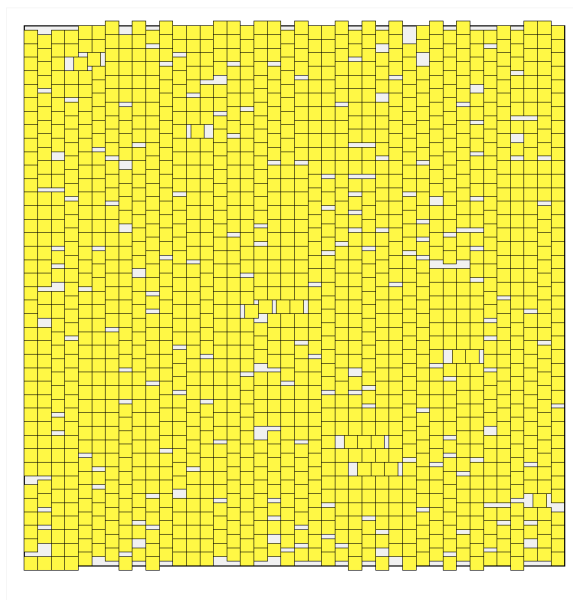


Figure 5.18: Snapshot of  $3 \times 3$  squares at  $\beta\mu = 5.950$ . Columnar behavior is evident.

## 5.6 Shapes that exhibit “diagonal” columns

After observing phase transitions and columnar ordering in square shapes, we decided to investigate shapes which might display columnar behavior along diagonal directions. One such polyomino was the size 6 “sort tail” fish shown in Figure 5.22, which can pack in a head-to-tail fashion. At first glance its shape resembles that of a goldfish cracker, hence the name.

The size 6 fish was essentially a negative result in that it remained disordered at high  $\beta\mu$ , with no phase transition observed. Its isotherm and a snapshot are shown in Figure 5.23. The availability of disordered very high density states seems to remove any driving force for formation of a diagonal columnar phase.

The size 11 “long tail” fish (isotherm shown in Figure 5.24) displays a sharp transition with hysteresis. This fish does not have a columnar phase, instead crystallizing into one of two



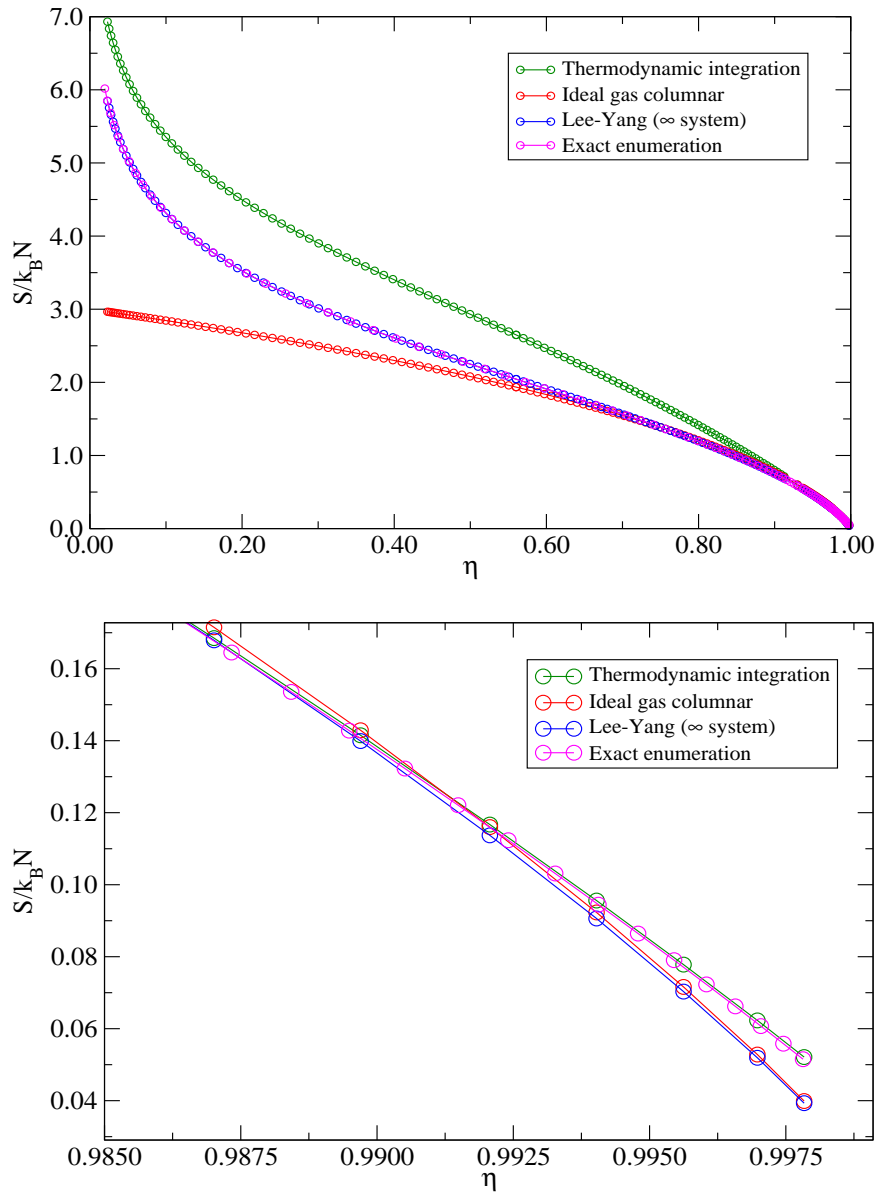


Figure 5.19: Entropy versus packing fraction for  $3 \times 3$  squares. This data was gathered through thermodynamic integration, using the virial equation of state for zero-density extrapolation and then continuing the integration from low-density states to near unit packing fraction states.

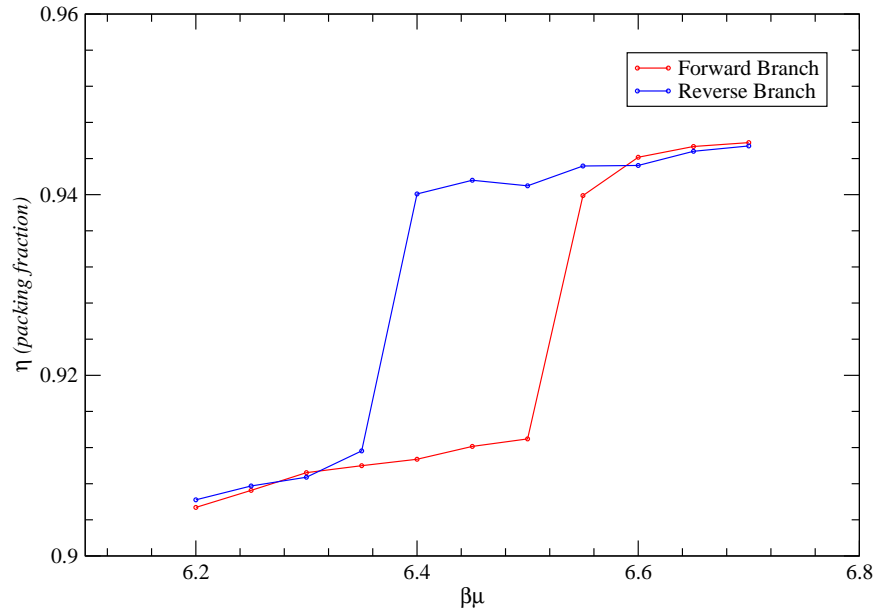


Figure 5.20: Isotherms of  $4 \times 4$  squares, with forward and reverse branches. This system displays a first-order phase transition.

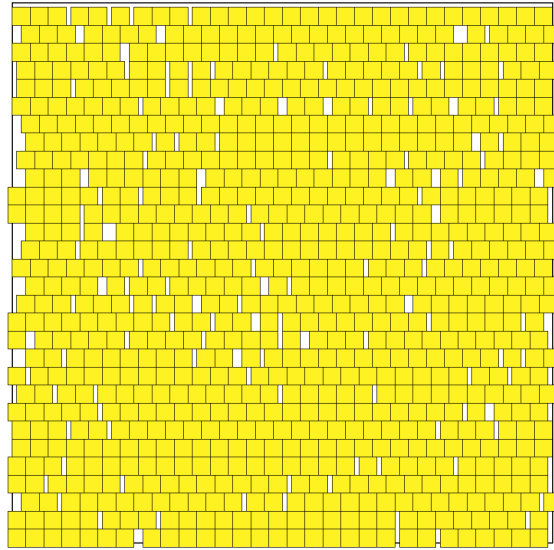


Figure 5.21: Snapshot of  $4 \times 4$  squares at  $\beta\mu = 6.950$ . Columnar order dominates in this system.

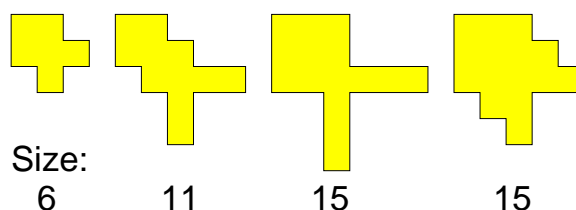


Figure 5.22: The four fish-like shapes examined in this study. From left to right: the “short tail” gold fish, “long tail” goldfish, “enlarged” fish, and “fat” fish.

crystal polymorphs (we observe both) in which there is no translational freedom. These are shown in Figure 5.25. Also interesting to note is that the dimer phase has a pair of enantiomeric tilings much like the pentomino *X* shape, except in this case dimers form the “base” of the tiling, rather than monomers.

The two structures have different entropies, which means that at large system sizes the polymorph with diagonal columns of varying orientation should be entropically favored. Each column of “head to tail” fish may also be oriented in two different directions, adding a factor of  $\ln 2$  to the entropy.

The “enlarged long tail”, a size 15 fish, was chosen because it cannot pack in a perpendicularly striped polymorph like the size 6 fish. Its isotherm and snapshot are shown in Figures 5.26 and 5.27, in which we observe a strong first-order transition and the resulting crystal phase. The crystal is composed of diagonal stripes of fish packed head-to-tail, with the stripes randomly oriented in one of two directions. A vacancy would not create translational entropy within a stripe, but the crystal as a whole gains entropy through the directional degree of freedom.

Lastly, the “fat fish”, another size 15 fish, does not have a protruding “tail”. The isotherm in Figure 5.28 shows a first-order transition with no hysteresis, and the corresponding snapshots in Figures 5.29 provide a picture of the fluid state and the mobility within the diagonal

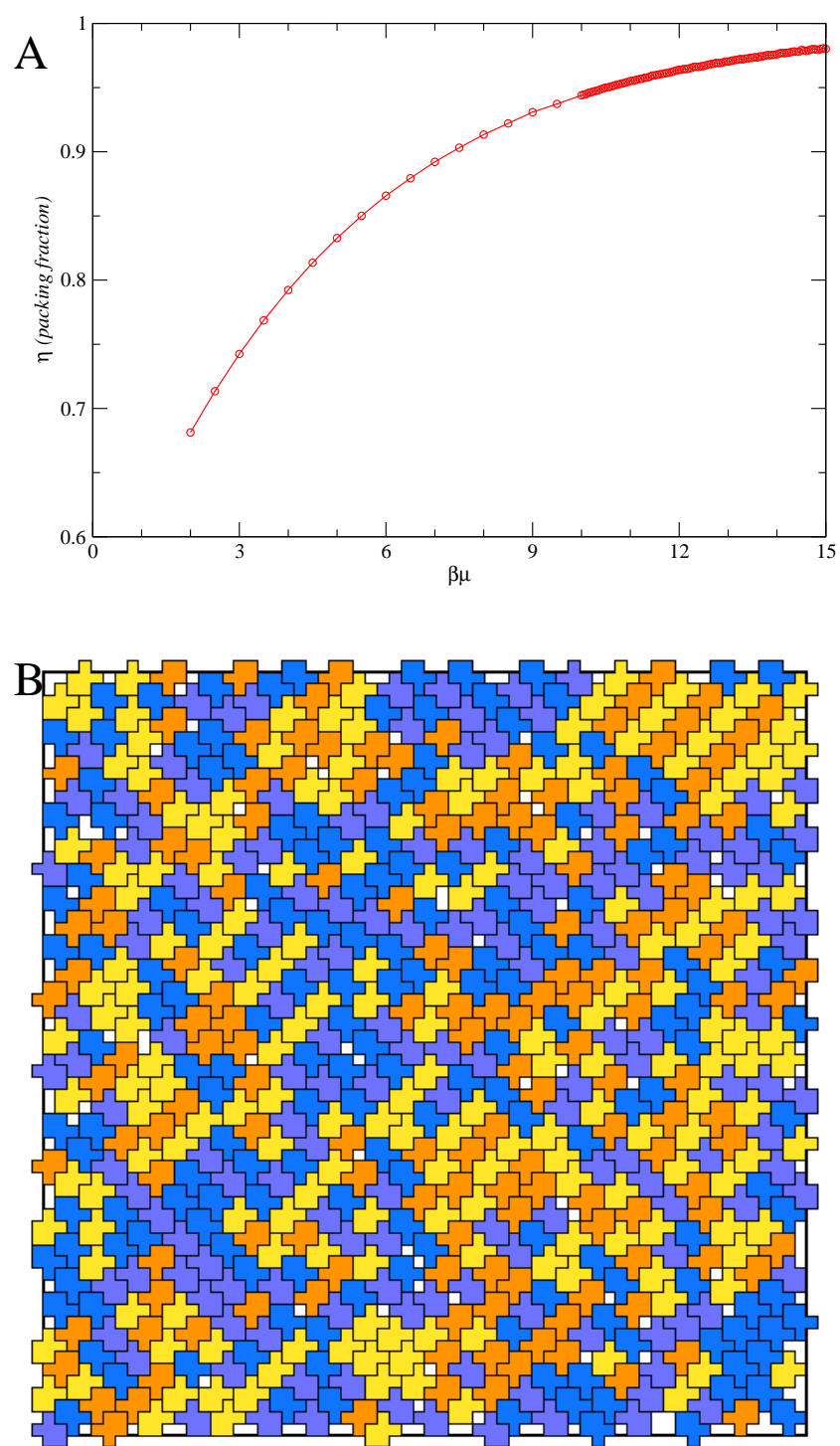


Figure 5.23: (A) Size 6 fish shape isotherm. No phase transition is observed. (B) Snapshot of this system at  $\beta\mu = 15$ .

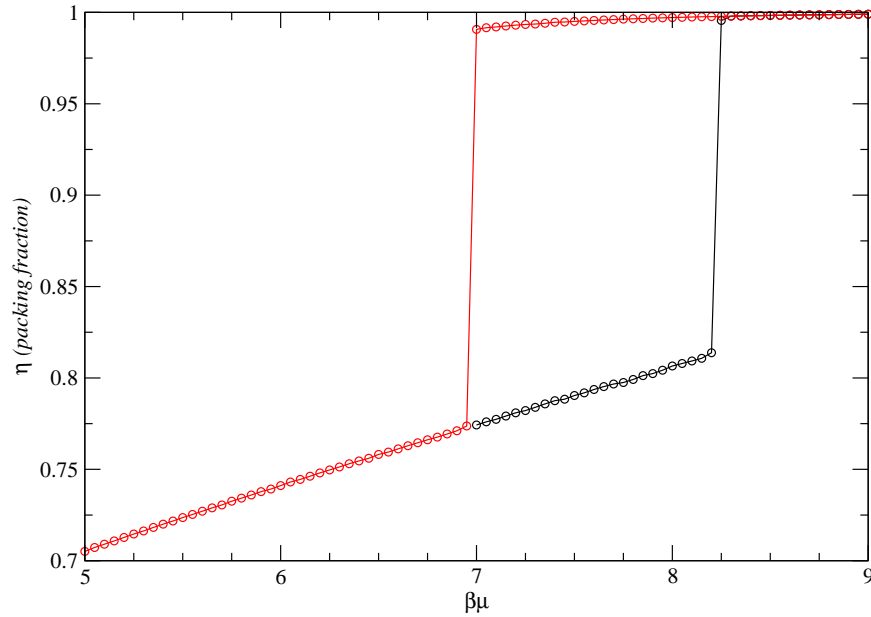


Figure 5.24: Isotherms for the size 11 “long tail” fish, which may undergo a phase transition to one of two crystal phases.

columnar phase. The transition occurs at a  $\beta\mu$  near 9, with a jump in packing fraction of from near 0.825 to above 0.925. The snapshots show that the system goes from a fluid with many small clusters to a system with stripes of two complementary directions. Voids which are the result of translation within a diagonal stripe containing a vacancy are also visible, as are occasional non-columnar out-of-column defects.

## 5.7 “Square-like” shapes

Motivated by the known phase transitions in off-lattice systems such as 2-D hard disks and the interesting columnar behavior of squares discussed previously, we decided to investigate a series of shapes of high symmetry. We refer to these as “square-like” shapes. They follow a logical progression from the *X* pentomino to selected larger shapes. In order, we

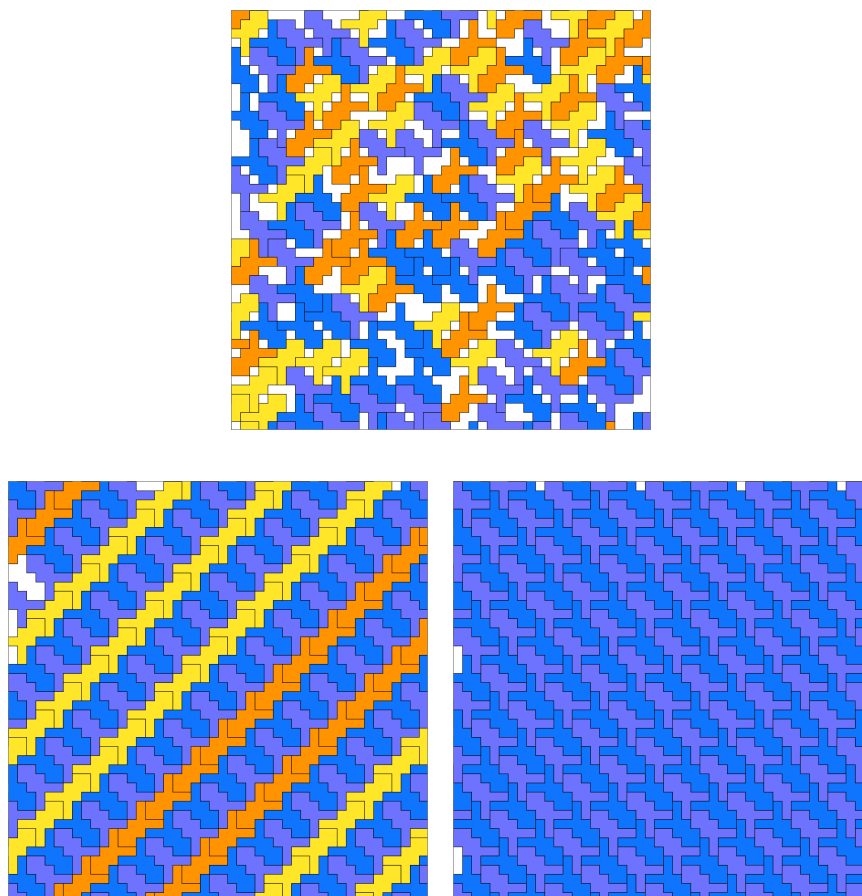


Figure 5.25: The liquid phase of size 11 fish at  $\beta\mu = 8.2$ , shortly below a phase transition, and in two crystal polymorphs post-transition.

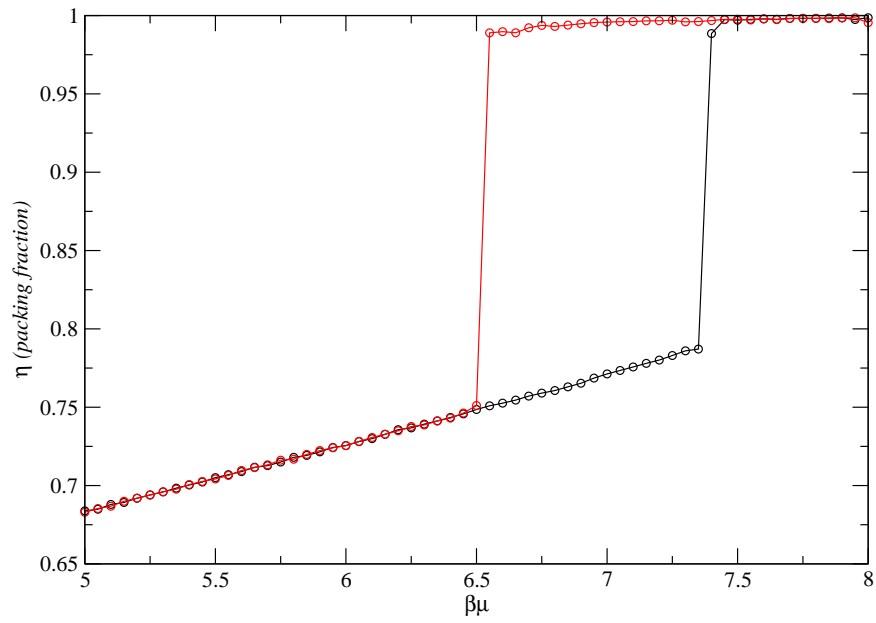


Figure 5.26: Isotherms for the “enlarged long tail” size 15 fish. This system undergoes a phase transition to a single crystal without translational freedom.

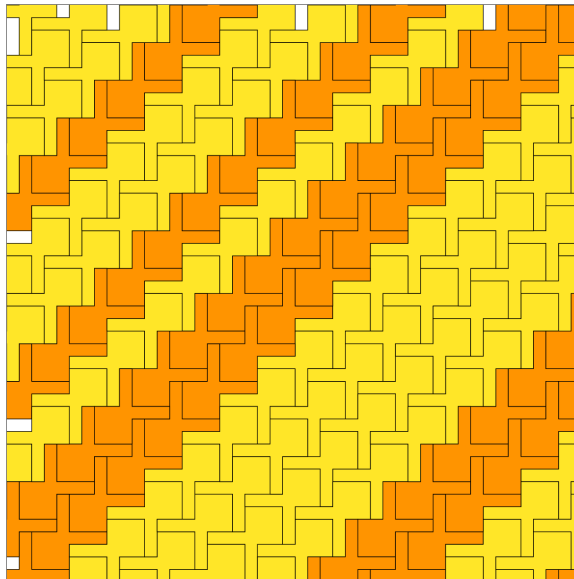


Figure 5.27: Solid phase of “enlarged long tail” size 15 fish, with stripes of opposite directions.

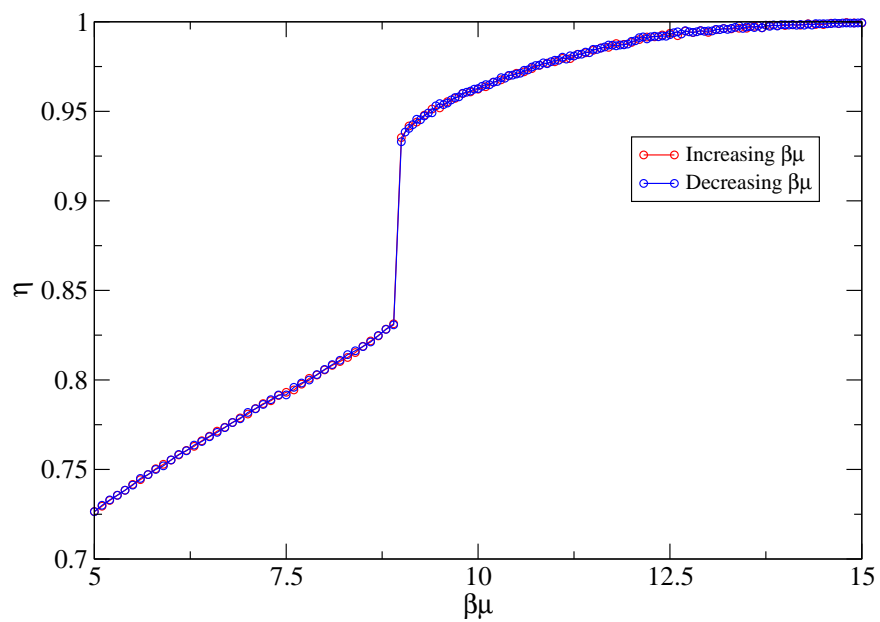


Figure 5.28: The “fat fish” isotherm, displaying a columnar transition. This diagonal columnar transition was “by design”.

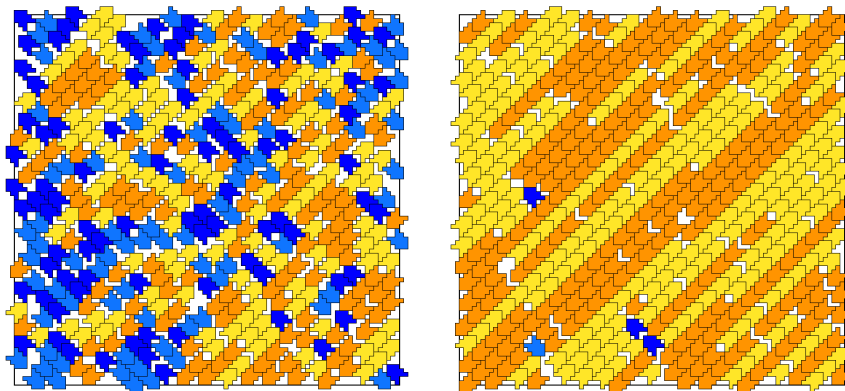


Figure 5.29: The “fat fish” just below (left) and above (right) the chemical potential for the phase transition.



studied 5-site, 9-site, 12-site, 13-site and 16-site shapes. The 5-site shape is the previously discussed  $X$  pentomino, while the 9-site and 16-site shapes are the  $3 \times 3$  and  $4 \times 4$  squares which were discussed in the section on columnar behavior. This leaves the size 12 “big cross” and size 13 “diamond” shapes to be discussed. These shapes are shown in Figure 5.30.

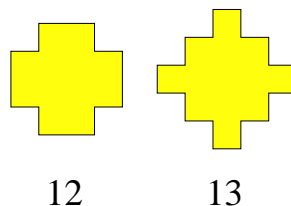


Figure 5.30: The size 12 “big cross” (or,  $X$ ) and size 13 “diamond” shapes.

The 12-site polyomino has a sharp first-order phase transition, shown in Figure 5.31 (A). The phase transition itself is abrupt, and a hysteresis loop is observed. Although this species has a shape manifestly similar to the  $X$  pentomino, it does not form a crystal with stereoisomers (snapshot in Figure 5.31) (B). There are orientations of the crystal which are degenerate via a 90 degree rotation. The density change through the transition is also significant, with  $\delta\eta > 0.1$ . After the transition, the system has a packing fraction of over 0.975 with only a few vacancy defects present. The hysteresis loop is roughly  $0.4 \beta\mu$  in width.

The isotherm of the 13-site “diamond” polyomino is shown in Figure 5.32, along with a snapshot of the crystal. It exhibits a strong first-order phase transition and hysteresis loop in the  $4.8$  to  $5.3 \beta\mu$  range. The crystalline phase has two enantiomers, similar to the  $X$  pentomino. As expected, after the phase transition, only one of the two is present in the simulation cell.

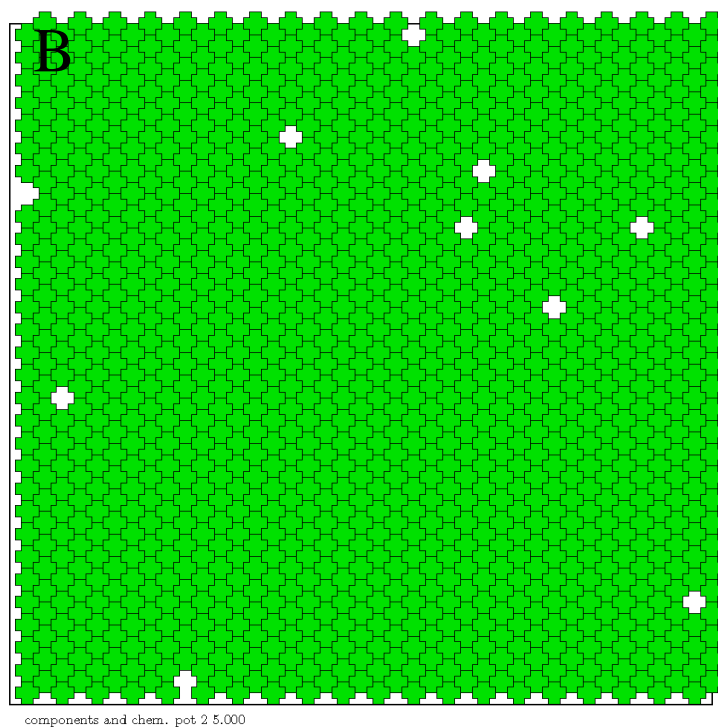
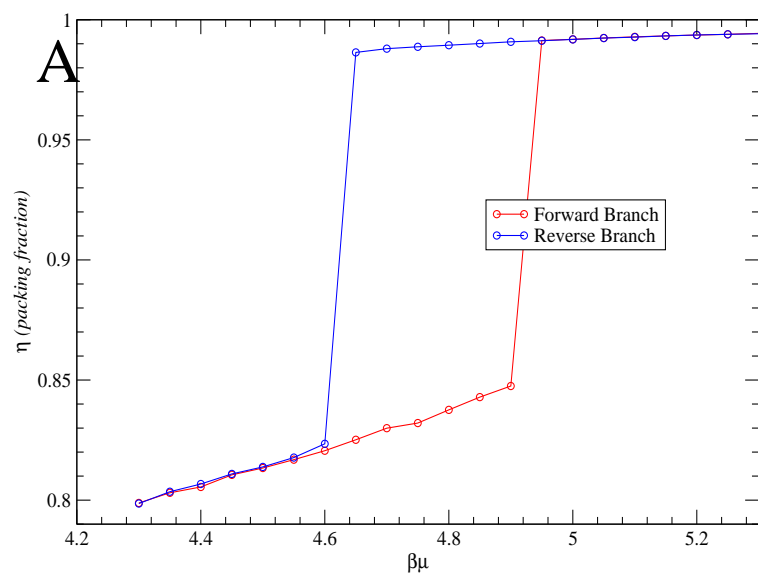


Figure 5.31: (A) Isotherms for a size 12 “X” polyomino. Hysteresis is observed with the phase transition. (B) Snapshot of the size 12 “X” polyomino crystal at  $\beta\mu = 5.0$ . The “interlocking” columns remove translational freedom for single vacancies.

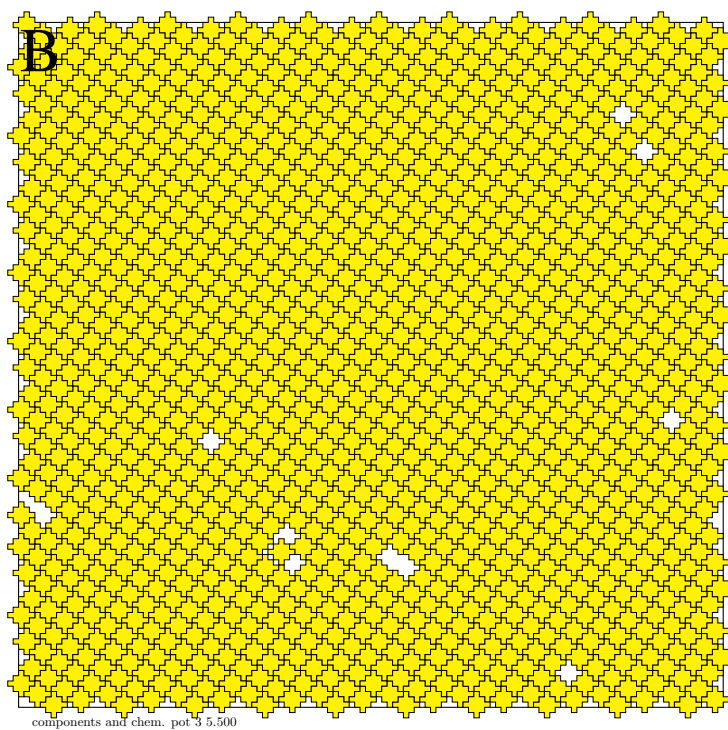
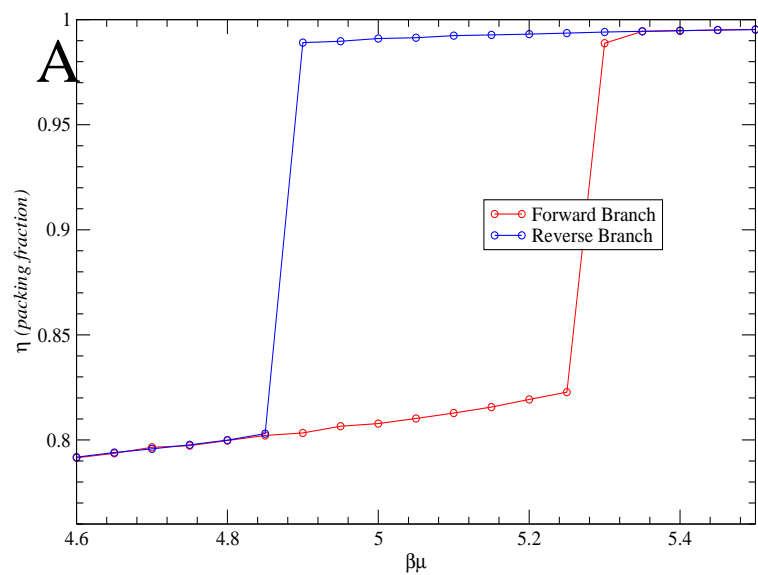


Figure 5.32: (A) Isotherms for the size 13 “diamond” polyomino. Hysteresis is observed in this system as well. (B) Snapshot of the size 13 “diamond” polyomino at  $\beta\mu = 5.5$ .

### 5.7.1 Two-component systems

We ran a single preliminary scan of a two-component system to observe phase transitions in a mixture. The components chosen were the 12-site “big cross” and 13-site “diamond” shapes discussed above. As these species are of similar size and each has a phase transition, we speculated that there would be phase separation or sharp phase transitions in the binary system. This is indeed the case. Figure 5.33 shows packing fraction (colored according to a temperature scale) versus chemical potentials of both species. The plot contains the results of a binary scan of 6400 individual state points. Species “i” is the 13-site polyomino, and species “j” is the 12-site polyomino. The lower left hand corner, colored dark blue, represents a total system packing fraction of 0.708. The dark red areas correspond to packing fractions near 0.98, which are nearly pure crystalline regions.

One feature that immediately stands out is the presence of two distinct ledges on either side of the phase space diagonal. These correspond to first-order phase transitions. One example of this is the transition from  $\beta\mu_j = 6.1$  to  $6.2$  at constant  $\beta\mu_i = 2$  (this is located along the central left edge of the plot). As that phase transition is followed in  $\beta\mu$  phase space to near  $(\beta\mu_i = 6, \beta\mu_j = 7)$ , it gradually becomes less distinct. Configurations near that point, but before the transition, resemble a well mixed, dense, two-phase system with occasional clusters of pure species. When the chemical potential of both species is high, the system may be difficult to equilibrate. As a result, it is difficult to mark the ends of these transition lines. Sharp “ends” may not even exist; the transition may change to second order or something else.

The asymmetry in the plot corresponds to what would be expected from the packing and phase transitions observed with the pure species in each polyomino. Species “i”, the 13-site polyomino, must overcome the disorder of the liquid phase to form a solid with two

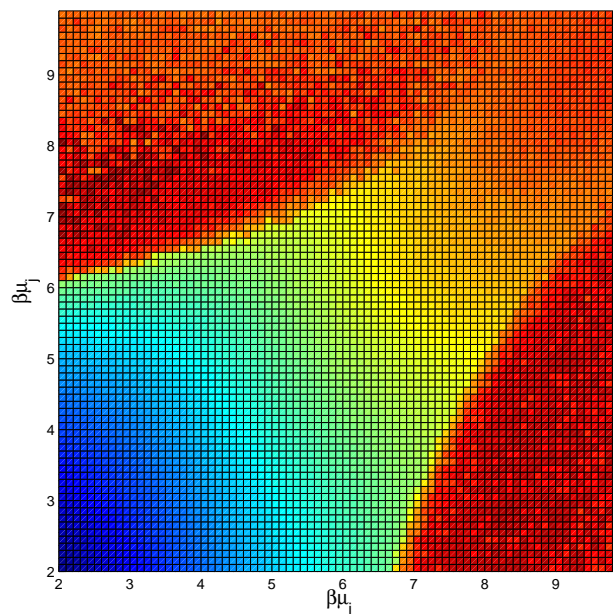


Figure 5.33: A 2D isotherm of the size 12 “big cross” (label j) and size 13 “diamond” (label i) shapes from  $\beta\mu = 2$  to 10 on each axis. The isotherm uses a “color temperature” scale to indicate density, with blue locations indicating low density and red locations indicating high density.

possible stereoisomers. It is also bigger than the 12-site polyomino. These factors explain why the phase transition for a binary system composed mostly of 13-site polyominoes occurs at a higher chemical potential than when the system is mostly 12-site polyominoes.

### 5.7.2 Future Work

The rich behavior displayed in the tetrominoes, pentominoes, and selected larger polyominoes suggests many avenues for continued work. We have developed the computational tools to simulate isotherms for subsequent polyomino families (such as hexominoes) in a nearly automated fashion. As the size of polyomino families grows exponentially, examining the hexominoes through octominoes could result in interesting discoveries. One such discovery could be that of a polyomino with over 10 polymorphs, the existence of which is still an open question [146]. While binary and multi-component mixtures of tetrominoes were studied in detail, only very limited work has been performed on mixtures of pentominoes or larger species. As larger polyominoes (some of which may have quite complicated shapes) are studied, their mixtures may display a strikingly wide range of behavior. For example, formation of co-crystals may occur.

To date, we have only studied phase transitions in pure component and binary systems. Phase transitions in mixtures containing many components may be discovered using a form of stereological analysis which is computationally inexpensive compared to exhaustive mapping. Or, rather than increasing the number of components, we could increase the number of dimensions and examine polycubes, of which only a small selection have been simulated [108]. Our simulations have also always used toroidal boundary conditions and cells of equal width and height. Pore-like conditions, previously studied for off-lattice rectangles [101], could be created by using “hard wall” boundaries for edges of the cell, and

pore size (and shape) could be tailored by varying the cell dimensions. Another alteration of the underlying lattice could be to use an equilateral triangular lattice in order to simulate polyiamonds, or a hexagonal lattice for polyhex species. Finally, our simulations have focused on an athermal model. Inclusion of attractive interactions between polyominoes – a drastic change to the model that would affect many parts of the simulation and analysis – would almost certainly provide many interesting results. Many opportunities for research await investigation.

# References

- [1] B. P. Feuston and S. H. Garofalini. Empirical three-body potential for vitreous silica. *J. Chem. Phys.*, 89(9):5818–5824, 1988.
- [2] N. Z. Rao and L. D. Gelb. Molecular dynamics simulations of the polymerization of aqueous silicic acid and analysis of the effects of concentration on silica polymorph distributions, growth mechanisms, and reaction kinetics. *J. Phys. Chem. B*, 108(33):12418–12428, 2004.
- [3] T. Bäck, F. Hoffmeister, and H.-P. Schwefel. A survey of evolutionary strategies. In R. K. Belew and L. B. Booker, editors, *Proceedings of the 4th International Conference on Genetic Algorithms*, pages 2–9, San Francisco, 1991. Morgan Kaufmann.
- [4] D. B. Fogel. An introduction to simulated evolutionary optimization. *IEEE Trans. Neural Networks*, 5(1):3–14, 1994.
- [5] K. A. De Jong. *Evolutionary Computation: A Unified Approach*. MIT Press, 2006.
- [6] S. Kirkpatrick, Jr. C. D. Gelatt, and M. P. Vecchi. Optimization by simulated annealing. *Science*, 220:671–680, 1983.
- [7] B. C. Barnes and L. D. Gelb. Meta-optimization of evolutionary strategies for empirical potential development: Application to aqueous silicate systems. *J. Chem. Theory Comput.*, 3:1749–1764, 2007.



- [8] A. Alavi, L. J. Alvarez, S. R. Elliot, and I. R. McDonald. Charge–transfer molecular dynamics. *Phil. Mag. B*, 65(3):489–500, 1992.
- [9] M. Gardner. Pentominoes and polyominoes: five games and a sampling of problems. *Sci. American*, 213(4), 1965.
- [10] S. W. Golomb. Tiling with polyominoes. *J. Comb. Theory*, (1):280–296, 1966.
- [11] *Polyominoes*. Princeton University Press, 1994.
- [12] B. C. Barnes, D. W. Siderius, and L. D. Gelb. Structure, thermodynamics, and solubility in tetromino fluids. *Langmuir*, 25:6702–6716, 2009.
- [13] C. G. Gray and K. E. Gubbins. *Theory of Molecular Fluids, Vol. 1*. Clarendon Press, Oxford, 1984.
- [14] M. P. Allen and D. J. Tildesley. *Computer Simulation of Liquids*. Clarendon Press, Oxford, 1987.
- [15] T. Schlick. *Molecular modeling and simulation: an interdisciplinary guide*. Springer-Verlag, New York, 2002.
- [16] F. Jensen. *Introduction to Computational Chemistry*. John Wiley & Sons, Ltd., Chichester, UK, 2nd edition, 2007.
- [17] A. D. MacKerell Jr., B. Brooks, C. L. Brooks III, L. Nilsson, B. Roux, Y. Won, and M. Karplus. CHARMM: The energy function and its parameterization with an overview of the program. In P. v. R. Schleyer, editor, *The Encyclopedia of Computational Chemistry*, volume 1, pages 271–277. Wiley, Chichester, 1998.
- [18] A. C. T. van Duin, S. Dasgupta, F. Lorant, and W. A. Goddard III. ReaxFF: A reactive force field for hydrocarbons. *J. Phys. Chem. A*, 105(41):9396–9409, 2001.

- [19] A. C. T. van Duin, A. Strachan, S. Stweman, Q. Zhang, X. Xu, and W. A. Goddard III. ReaxFF(SiO) reactive force field for silicon and silicon oxide systems. *J. Phys. Chem. A*, 107(19):3803–3811, 2003.
- [20] K. D. Nielson, A. C. T. van Duin, J. Oxgaard, W. Q. Deng, and W. A. Goddard III. Development of the ReaxFF reactive force field for describing transition metal catalyzed reactions, with application to the initial stages of the catalytic formation of carbon nanotubes. *J. Phys. Chem. A*, 109(3):493–499, 2005.
- [21] S. Cheung, W. Q. Deng, A. C. T. van Duin, and W. A. Goddard III. ReaxFF(MgH) reactive force field for magnesium hydride systems. *J. Phys. Chem. A*, 109(5):851–859, 2005.
- [22] S. S. Han, A. C. T. van Duin, W. A. Goddard III, and H. M. Lee. Optimization and application of lithium parameters for the reactive force field, ReaxFF. *J. Phys. Chem. A*, 109(20):4575–4582, 2005.
- [23] S. S. Han, J. K. Kang, H. M. Lee, A. C. T. van Duin, and W. A. Goddard III. The theoretical study on interaction of hydrogen with single-walled boron nitride nanotubes. I. The reactive force field ReaxFF(HBN) development. *J. Chem. Phys.*, 123(11):114703, 2005.
- [24] S. Izvekov, M. Parrinello, C. J. Burnham, and G. A. Voth. Effective force fields for condensed phase systems from ab initio molecular dynamics simulation: A new method for force-matching. *J. Chem. Phys.*, 120(23):10896–10913, 2004.
- [25] S. Izvekov and G. A. Voth. Effective force field for liquid hydrogen fluoride from ab initio molecular dynamics simulation using the force-matching method. *J. Phys. Chem. B*, 109(14):6573–6586, 2005.

- [26] R. Bukowski, K. Szalewicz, G. C. Groenenboom, and A. van der Avoird. Predictions of the properties of water from first principles. *Science*, 315:1249–1252, 2007.
- [27] A. Faure, P. Valiron, M. Wernli, L. Wiesenfeld, C. Rist, J. Noga, and J. Tennyson. A full nine-dimensional potential-energy surface for hydrogen molecule-water collisions. *J. Chem. Phys.*, 112:221102, 2005.
- [28] T. Strassner, M. Busold, and W. A. Herrmann. MM3 parameterization of four- and five-coordinated rhenium complexes by a genetic algorithm—which factors influence the optimization performance? *J. Comput. Chem.*, 23(2):282–290, 2002.
- [29] H. L. Lemberg and F. H. Stillinger. Central-force model for liquid water. *J. Chem. Phys.*, 62(5):1677–1690, 1975.
- [30] A. Rahman, F. H. Stillinger, and H. L. Lemberg. Study of a central force model for liquid water by molecular dynamics. *J. Chem. Phys.*, 63(12):5223–5230, 1975.
- [31] F. H. Stillinger and A. Rahman. Revised central force potentials for water. *J. Chem. Phys.*, 68(2):666–670, 1978.
- [32] W. H. Press, S. A. Teukolsky, W. T. Vetterling, and B. P. Flannery. *Numerical Recipes in Fortran 77*, pages 387–406. Cambridge University Press, 2 edition, 1992.
- [33] A. C. T. van Duin, J. M. A. Baas, and B. van de Graaf. Delft molecular mechanics - a new approach to hydrocarbon force-fields - inclusion of a geometry-dependent charge calculation. *J. Chem. Soc. Faraday Trans.*, 90(19):2881–2895, 1994.
- [34] M. A. Collins. Molecular potential-energy surfaces for chemical reaction dynamics. *Theor. Chem. Acc.*, 108:313–324, 2002.
- [35] G. E. Moyano and M. A. Collins. Molecular potential energy surfaces by interpolation: Strategies for faster convergence. *J. Chem. Phys.*, 121(20):9769–9775, 2004.

- [36] H. M. Netzloff. Growing multiconfigurational potential energy surfaces with applications to  $X+H_2$  ( $X=C,N,O$ ) reactions. *J. Chem. Phys.*, 124:154104, 2006.
- [37] Y. Guo, L. B. Harding, A. F. Wagner, M. Minkoff, and D. L. Thompson. Interpolating moving least-squares methods for fitting potential energy surfaces: An application to the  $H_2CN$  unimolecular reaction. *J. Chem. Phys.*, 126:104105, 2007.
- [38] H.-G. Beyer and H.-P. Schwefel. Evolution strategies. *Natural Computing*, 1:3–52, 2002.
- [39] I. Rechenberg. Cybernetic solution path of an experimental problem. Technical report, Royal Aircraft Establishment, Farnborough, Library Translation 1122, 1965.
- [40] H.-P. Schwefel. Kybernetische evolution als strategie der experimentellen forschung in der strömungstechnik. Master’s thesis, Technical University of Berlin, 1965.
- [41] I. Rechenberg. *Evolutionsstrategie: Optimierung technischer Systeme nach Prinzipien der biologischen Evolution*. PhD thesis, Technical University of Berlin, Department of Process Engineering, 1971.
- [42] I. Rechenberg. *Evolutionsstrategie: Optimierung technischer Systeme nach Prinzipien der biologischen Evolution*. Frommann-Holzboog Verlag, Stuttgart, 1973.
- [43] H.-P. Schwefel. *Evolutionsstrategie und numerische Optimierung*. PhD thesis, Technical University of Berlin, 1975.
- [44] L. Fogel, A. Owens, and M. Walsh. *Artificial Intelligence through Simulated Evolution*. John Wiley and Sons, 1966.
- [45] J. Holland. *Adaptation in Natural and Artificial Systems*. University of Michigan Press, 1975.

- [46] *Evolutionary Computation: A Unified Approach*, pages 49–69. MIT Press, 2006.
- [47] *Evolutionary Computation: A Unified Approach*, pages 72–73. MIT Press, 2006.
- [48] T. R. Cundari, J. Deng, and W. Fu. PM3(tm) parameterization using genetic algorithms. *Int. J. Quantum Chem.*, 77(1):421–432, 2000.
- [49] I. Rossi and D. G. Truhlar. Parameterization of nddo wavefunctions using genetic algorithms. an evolutionary approach to parameterizing potential energy surfaces and direct dynamics calculations for organic reactions. *Chem. Phys. Lett*, 233:231–236, 1995.
- [50] M. Mohr, J. P. McNamara, H. Wang, S. A. Rajeev, J. Ge, C. A. Morgado, and I. H. Hiller. The use of methods involving semi-empirical molecular orbital theory to study the structure and reactivity of transition metal complexes. *Faraday Discuss.*, 124:413–428, 2003.
- [51] E. N. Brothers and Jr. K. M. Merz. Sodium parameters for AM1 and PM3 optimized using a modified genetic algorithm. *J. Phys. Chem. B*, 106(10):2779–2785, 2002.
- [52] Y. Ge and J. D. Head. Global optimization of Si(x)H(y) at the ab initio level via an iteratively parameterized semiempirical method. *Int. J. Quant. Chem*, 95(4/5):617–626, 2003.
- [53] D. E. Clark and D. R. Westhead. Evolutionary algorithms in computer-aided molecular design. *J. Comput. Aid. Mol. Design*, 10:337–358, 1996.
- [54] E. W. Laméijer, T. Bäck, J. N. Kok, and A. P. Ijzerman. *Natural Computing*, 4:177–243, 2005.
- [55] R. Thomsen. *BioSystems*, 72:57–73, 2003.

- [56] T. Strassner, M. Busold, and H. Radrich. FFGeneAtoR 2.0 – an automated tool for the generation of MM3 force field parameters. *J. Mol. Model.*, 7:374–377, 2001.
- [57] P. Wolohan, J. Yoo, M. J. Welch, and D. E. Reichert. QSAR studies of copper azamacrocycles and thiosemicarbazones: MM3 parameter development and prediction of biological properties. *J. Med. Chem.*, 48(17):5561–5569, 2005.
- [58] J. Wang and P. A. Kollman. Automatic parameterization of force field by systematic search and genetic algorithms. *J. Comput. Chem.*, 22(12):1219–1228, 2001.
- [59] A. Mallik, K. Runge, H.-P. Cheng, and J. Dufty. Constructing a small strain potential for multi-scale modeling. *Mol. Sim.*, 31(10):695–703, 2005.
- [60] A. Globus, M. Menon, and D. Srivastava. Javagenes: Evolving molecular force field parameters with genetic algorithms. *Comput. Model. Eng. Sci.*, 3(5):557–574, 2002.
- [61] B. P. Feuston and S. H. Garofalini. Oligomerization in silica sols. *J. Phys. Chem.*, 94(13):5351–5356, 1990.
- [62] *Evolutionary Computation: A Unified Approach*, page 27. MIT Press, 2006.
- [63] *Evolutionary Computation: A Unified Approach*, pages 128–130. MIT Press, 2006.
- [64] M. Born and J. E. Mayer. *Zeits. f. Physik*, 75:1, 1932.
- [65] M. L. Huggins and J. E. Mayer. Interatomic distances in crystals of the alkali halides. *J. Chem. Phys.*, 1(9):643–646, 1933.
- [66] F. H. Stillinger and T. A. Weber. Computer simulation of local order in condensed phases of silicon. *Phys. Rev. B*, 31(8):5262–5271, 1985.
- [67] R. Car and M. Parrinello. Unified approach for molecular dynamics and density-functional theory. *Phys. Rev. Lett.*, 55(22):2471–2474, 1985.

- [68] J. P. Perdew, K. Burke, and M. Ernzerhof. Generalized gradient approximation made simple. *Phys. Rev. Lett.*, 77(18):3865–3868, 1996.
- [69] D. Vanderbilt. Soft self-consistent pseudopotentials in a generalized eigenvalue formalism. *Phys. Rev. B*, 41(11):7892–7895, 1990.
- [70] M. J. Frisch, G. W. Trucks, H. B. Schlegel, G. E. Scuseria, M. A. Robb, J. R. Cheeseman, J. A. Montgomery Jr. and T. Vreven, K. N. Kudin, J. C. Burant, J. M. Millam, S. S. Iyengar, J. Tomasi, V. Barone, B. Mennucci, M. Cossi, G. Scalmani, N. Rega, G. A. Petersson, H. Nakatsuji, M. Hada, M. Ehara, K. Toyota, R. Fukuda, J. Hasegawa, M. Ishida, T. Nakajima, Y. Honda, O. Kitao, H. Nakai, M. Klene, X. Li, J. E. Knox, H. P. Hratchian, J. B. Cross, C. Adamo, J. Jaramillo, R. Gomperts, R. E. Stratmann, O. Yazyev, A. J. Austin, R. Cammi, C. Pomelli, J. W. Ochterski, P. Y. Ayala, K. Morokuma, G. A. Voth, P. Salvador, J. J. Dannenberg, V. G. Zakrzewski, S. Dapprich, A. D. Daniels, M. C. Strain, O. Farkas, D. K. Malick, A. D. Rabuck, K. Raghavachari, J. B. Foresman, J. V. Ortiz, Q. Cui, A. G. Baboul, S. Clifford, J. Cioslowski, B. B. Stefanov, G. Liu, A. Liashenko, P. Piskorz, I. Komaromi, R. L. Martin, D. J. Fox, T. Keith, M. A. Al-Laham, C. Y. Peng, A. Nanayakkara, M. Challacombe, P. M. W. Gill, B. Johnson, W. Chen, M. W. Wong, C. Gonzalez, and J. A. Pople. Gaussian, 2003. Gaussian, Inc., Pittsburgh PA.
- [71] W. G. Hoover. Canonical dynamics: Equilibrium phase-space distributions. *Phys. Rev. A*, 31(3):1695–1697, 1985.
- [72] Cpmd, copyright ibm corp 1990-2001, copyright mpi für festkörperforschung stuttgart 1997-2005.
- [73] W. H. Press, S. A. Teukolsky, W. T. Vetterling, and B. P. Flannery. *Numerical Recipes in Fortran 77*, pages 436–448. Cambridge University Press, 2 edition, 1992.

- [74] *Evolutionary Computation: A Unified Approach*, pages 77–78. MIT Press, 2006.
- [75] P. Moscato and M. G. Norman. *Parallel Computing and Transputer Applications*, chapter A "Memetic" Approach for the Traveling Salesman Problem Implementation of a Computational Ecology for Combinatorial Optimization on Message-Passing Systems, pages 177–186. IOS Press/CIMNE, 1992.
- [76] R. Salazar and L. D. Gelb. An investigation of the effects of the structure of gel materials on their adsorptive properties using a simple lattice-gas model. *Mol. Phys.*, 102(9-10):1015–1030, 2004.
- [77] R. Salazar and L. D. Gelb. Application of the Bethe-Peierls approximation to a lattice-gas model of adsorption on mesoporous materials. *Phys. Rev. E*, 71:041502, 2005.
- [78] R. Salazar and L. D. Gelb. A computational study of the reconstruction of amorphous mesoporous materials from gas adsorption isotherms and structure factors via evolutionary optimization. *Langmuir*, 23:530–541, 2007.
- [79] L. D. Gelb. Simulating silica aerogels with a coarse-grained flexible model and langevin dynamics. *J. Phys. Chem. C*, 111:15792–15802, 2007.
- [80] L. Huang and J. Kieffer. Molecular dynamics study of cristobalite silica using a charge transfer three-body potential: phase transformation and structural disorder. *J. Chem. Phys.*, 118(3):1487–1498, 2003.
- [81] S. Bhattacharya and J. Kieffer. Fractal dimensions of silica gels generated using reactive molecular dynamics simulations. *J. Chem. Phys.*, 122:094715, 2005.



- [82] B. W. H. van Beest, G. J. Kramer, and R. A. Santen. Force fields for silicas and aluminophosphates based on ab initio calculations. *Phys. Rev. Lett.*, 64(16):1955–1958, 1990.
- [83] N. Troullier and J. L. Martins. Efficient pseudopotentials for plane-wave calculations. *Phys. Rev. B*, 43(3):1993–2006, 1991.
- [84] Z. Z. Bandić, D. Litvinov, and M. Rooks. Nanostructured materials in information storage. *MRS Bulletin*, 33(9):831–837, 2008.
- [85] F. Gu, L. Zhang, B. A. Teply, N. Mann, A. Wang, A. F. Radovic-Moreno, R. Langer, and O. C. Farokhzad. Precise engineering of targeted nanoparticles by using self-assembled biointegrated block copolymers. *Proc. Nat. Acad. Sci. USA*, 105(7):2586–2591, 2008.
- [86] L. Schmidt-Mende, A. Fechtenkötter, K. Müllen, E. Moons, R. H. Friend, and J. D. MacKenzie. Self-organized discotic liquid crystals for high-efficiency organic photovoltaics. *Science*, 293(5532):1119–1122, 2001.
- [87] A. Ulman. Formation and structure of self-assembled monolayers. *Chem. Rev.*, 96:1533–1554, 1996.
- [88] J. C. Love, L. A. Estroff, J. K. Kriebel, R. G. Nuzzo, and G. M. Whitesides. Self-assembled monolayers of thiolates on metals as a form of nanotechnology. *Chem. Rev.*, 105(4):1103–1170, 2005.
- [89] S. C. Glotzer, M. A. Horsch, C. R. Iacovella, Z. L. Zhang, E. R. Chan, and X. Zhang. Self-assembly of anisotropic tethered nanoparticle shape amphiphiles. *Curr. Op. Colloid Int. Sci.*, 10(5-6):287–295, 2005.

- [90] S. C. Glotzer and M. J. Solomon. Anisotropy of building blocks and their assembly into complex structures. *Nature Mat.*, 6:557–562, 2007.
- [91] N. Metropolis, A. W. Rosenbluth, M. N. Rosenbluth, A. H. Teller, and E. Teller. Equation of state calculations by fast computing machines. *J. Chem. Phys.*, 21:1087–1092, 1953.
- [92] B. J. Alder and T. E. Wainwright. Phase transition for a hard sphere system. *J. Chem. Phys.*, 27:1208–1209, 1957.
- [93] B. J. Alder. Studies in molecular dynamics. III. A mixture of hard spheres. *J. Chem. Phys.*, 40(9):2724–2730, 1964.
- [94] D. W. Siderius and D. S. Corti. Extension of scaled particle theory to inhomogeneous hard particle fluids. III. Entropic force exerted on a cavity that intersects a hard wall. *Phys. Rev. E*, 75:011108, 2007.
- [95] K. W. Wojciechowski, D. Frenkel, and A. C. Brańka. Nonperiodic solid phase in a two-dimensional hard-dimer system. *Phys. Rev. Letts.*, 66(24):3168–3171, 1991.
- [96] M. P. Allen and A. A. Imbierski. A molecular dynamics study of the hard dumb-bell system. *Mol. Phys.*, 60(2):453–473, 1987.
- [97] K. W. Wojciechowski and D. Frenkel. Tetratic phase in the planar hard square system? *Computat. Methods Sci. Tech.*, 10(2):235–255, 2004.
- [98] M. Porto and H. E. Roman. Critical packing fraction of rectangular particles on the square lattice. *Phys. Rev. E*, 62(1):100–102, 2000.
- [99] A. Donev, J. Burton, F. H. Stillinger, and S. Torquato. Tetratic order in the phase behavior of a hard-rectangle system. *Phys. Rev. B*, 73(5):054109(11), 2006.

- [100] D. de las Heras, Y. Martínez-Ratón, and E. Velasco. Demixing and orientational ordering in mixtures of rectangular particles. *Phys. Rev. E*, 76:031704, 2007.
- [101] D. A. Triplet and K. A. Fichthorn. Monte Carlo simulation of two-dimensional hard rectangles: confinement effects. *Phys. Rev. E*, 77(1):011707(10), 2008.
- [102] T. Schilling, S. Pronk, B. Mulder, and D. Frenkel. Monte Carlo study of hard pentagons. *Phys. Rev. E*, 71:036138, 2005.
- [103] E. DeMiguel, L. F. Rull, M. K. Chalam, and K. E. Gubbins. Liquid crystal phase diagram of the Gay-Berne fluid. *Mol. Phys.*, 74(2):405–424, 1991.
- [104] P. Bolhuis and D. Frenkel. Tracing the phase boundaries of hard spherocylinders. *J. Chem. Phys.*, 106(2):666–687, 1997.
- [105] S. C. McGrother, D. C. Williamson, and G. Jackson. A re-examination of the phase diagram of hard spherocylinders. *J. Chem. Phys.*, 104(17):6755–6771, 1996.
- [106] M. Dijkstra, D. Frenkel, and J.-P. Hansen. Phase separation in binary hard-core mixtures. *J. Chem. Phys.*, 101(4):3179–3189, 1994.
- [107] D. S. Gaunt and M. E. Fisher. Hard-sphere lattice gases. I. Plane-square lattice. *J. Chem. Phys.*, 43(8):2840–2863, 1965.
- [108] A. Z. Panagiotopoulos. Thermodynamic properties of lattice hard-sphere models. *J. Chem. Phys.*, 123:104504, 2005.
- [109] R. J. Baxter. *Exactly Solved Models in Statistical Mechanics*. Academic Press, London, 1982.
- [110] W. Li, K. F. Freed, and A. M. Nemirovsky. Packing entropy of extended, hard, rigid objects on a lattice. *J. Chem. Phys.*, 98(11):8469–8483, 1993.

- [111] D. Buta and K. F. Freed. Lattice polymers with structured monomers: a Monte Carlo study of thermodynamic properties of melts and solutions. *J. Chem. Phys.*, 116(24):10959–1096, 2002.
- [112] D. Buta and K. F. Freed. Mixtures of lattice polymers with structured monomers. *J. Chem. Phys.*, 120(13):6288–6298, 2004.
- [113] J. R. Davis, M. V. Piccarreta, R. B. Rauch, T. K. Vanderlick, and A. Z. Panagiotopoulos. Phase behavior of rigid objects on a cubic lattice. *Ind. Eng. Chem. Res.*, 45(16):5421–5425, 2006.
- [114] A. E. Krukowski, H. S. Chan, and K. A. Dill. An exact lattice model of complex solutions: Chemical potentials depend on solute and solvent shape. *J. Chem. Phys.*, 103(24):10675–10688, 1995.
- [115] R. Brem, H. S. Chan, and K. A. Dill. Extracting microscopic energies from oil-phase solvation experiments. *J. Phys. Chem. B*, 104:7471–7482, 2000.
- [116] P. W. Kasteleyn. The statistics of dimers on a lattice: I. The number of dimer arrangements on a quadratic lattice. *Physica*, 27(12):1209–1225, 1961.
- [117] H. Cohn, R. Kenyon, and J. Propp. A variational principle for domino tilings. *J. Amer. Math. Soc.*, 15:297–346, 2001.
- [118] A. R. Conway and A. J. Guttmann. On two-dimensional percolation. *J. Phys. A*, 28:891–904, 1995.
- [119] A. Pajintov. Tetris. Video game, 1985. Trademarked by The Tetris Company, LLC.
- [120] E. Caglioti, V. Loreto, H. J. Herrmann, and M. Nicodemi. A ‘Tetris-like’ model for the compaction of dry granular media. *Phys. Rev. Letts.*, 79(8):1575–1578, 1997.

- [121] S. Krishnamurthy, V. Loreto, H. J. Herrmann, S. S. Manna, and S. Roux. Self-structuring of granular media under internal avalanching. *Phys. Rev. Letts.*, 83(2):304–307, 1999.
- [122] E. G. Coffman, Jr., P. J. Downey, and P. Winkler. Packing rectangles in a strip. *Acta Informatica*, 38:673–693, 2002.
- [123] D. A. Matoz-Fernandez, D. H. Linares, and A. J. Ramirez-Pastor. Critical behavior of long straight rigid rods on two-dimensional lattices: theory and Monte Carlo simulations. *J. Chem. Phys.*, 128:214902, 2008.
- [124] F. Cicoira and F. Rosei. Playing Tetris at the nanoscale. *Surf. Sci.*, 600:1–5, 2006.
- [125] A. Troisi, V. Wong, and M. A. Ratner. An agent-based approach for modeling molecular self-organization. *Proc. Nat. Acad. Sci.*, 102(2):255–260, 2005.
- [126] N. Liu, S. Haq, G. R. Darling, and R. Raval. Direct visualization of enantiospecific substitution of chiral guest molecules into heterochiral molecular assemblies at surfaces. *Angew. Chem. Int. Ed.*, 46:7613–7616, 2007.
- [127] L. Mao, H. H. Harris, and K. J. Stine. Simple lattice simulation of chiral discrimination in monolayers. *J. Chem. Inf. Comput. Sci.*, 42:1179–1184, 2002.
- [128] M. Mezei. A cavity-biased  $(T, V, \mu)$  Monte Carlo method for the computer simulation of fluids. *Mol. Phys.*, 40(4):901–906, 1980.
- [129] H. Flyvbjerg and H. G. Petersen. Error estimates on averages of correlated data. *J. Chem. Phys.*, 91(1):461–466, 1989.
- [130] S. Mignani and R. Rosa. Markov Chain Monte Carlo in statistical mechanics: the problem of accuracy. *Technometrics*, 43(3):347–355, 2001.

- [131] K. Zhao, C. Harrison, D. Huse, W. B. Russel, and P. M. Chaikin. Nematic and almost-tetratic phases of colloidal rectangles. *Phys. Rev. E*, 76:040401R, 2007.
- [132] A. Ghosh and D. Dhar. On the orientational ordering of long rods on a lattice. *Euro. Phys. Letts.*, 78:20003, 2007.
- [133] T. L. Hill. *An Introduction to Statistical Thermodynamics*. Addison-Wesley, Reading, MA, 1960.
- [134] S. Moghaddam, Y. C. Kim, and M. E. Fisher. Convergence of fine-lattice discretization for near-critical fluids. *J. Phys. Chem. B*, 109(14):6824–6837, 2005.
- [135] W. Henry. Experiments on the Quantity of Gases absorbed by Water, at different Temperatures, and under different Pressures. *Phil. Trans. Roy. Soc. (London)*, 93:29–43, 1803.
- [136] E. E. Underwood. *Quantitative Stereology*. Addison-Wesley, Reading, MA, 1970.
- [137] K. S. Shing, K. E. Gubbins, and K. Lucas. Henry constants in non-ideal fluid mixtures: Computer simulation and theory. *Mol. Phys.*, 65(5):1235–1252, 1988.
- [138] J. W. Tester and M. Modell. *Thermodynamics and its Applications*. Prentice Hall, Upper Saddle River, NJ, 3rd edition, 1996.
- [139] B. Widom. Some topics in the theory of fluids. *J. Chem. Phys.*, 39:2802–2812, 1963.
- [140] D. .H. Redelmeier. Counting polyominoes: Yet another attack. *Disc. Math.*, 36:191–203, 1981.
- [141] *Mathematical Recreations: A Collection in Honor of Martin Gardner*. Dover, 1988.

- [142] E. V. Shevchenko, D. V. Talapin, C. B. Murray, and S. O'Brien. Structural characterization of self-assembled multifunctional binary nanoparticle superlattices. *J. Am. Chem. Soc.*, 128:3620–3637, 2006.
- [143] *Polyominoes: A Guide to Puzzles and Problems in Tiling*, pages 145–152. Math. Assoc. Amer., 1996.
- [144] *Polyominoes: A Guide to Puzzles and Problems in Tiling*, pages 83–95. Math. Assoc. Amer., 1996.
- [145] T. D. Lee and C. N. Yang. Statistical theory of equations of state and phase transitions. II. lattice gas and ising model. *Phys. Rev.*, 87(3):410–419, 1952.
- [146] A. Fontaine and G. E. Martin. Polymorphic polyominoes. *Math. Mag.*, 57(5):275–283, 1984.